Implementation and Refinement of a Comprehensive Model for Dense Granular Flows

Final Technical Report

Project Period: 1 October 2011 – 30 September 2015

Principal Investigator: Prof. Sankaran Sundaresan

Submitted: December 2015

Award Number: DE-FE0006932

Recipient: The Trustees of Princeton University
Office of Research & Project Administration
4 New South Building
P. O. Box 36
Princeton, NJ 08544

Abstract

Dense granular flows are ubiquitous in both natural and industrial processes. They manifest three different flow regimes, each exhibiting its own dependence on solids volume fraction, shear rate, and particle-level properties. This research project sought to develop continuum rheological models for dense granular flows that bridges multiple regimes of flow, implement them in open-source platforms for gas-particle flows and perform test simulations.

The first phase of the research covered in this project involved implementation of a steady-shear rheological model that bridges quasi-static, intermediate and inertial regimes of flow into MFIX (Multiphase Flow with Interphase eXchanges - a general purpose computer code developed at the National Energy Technology Laboratory). MFIX simulations of dense granular flows in hourglass-shaped hopper were then performed as test examples. The second phase focused on formulation of a modified kinetic theory for frictional particles that can be used over a wider range of particle volume fractions and also apply for dynamic, multi-dimensional flow conditions. To guide this work, simulations of simple shear flows of identical mono-disperse spheres were also performed using the discrete element method. The third phase of this project sought to develop and implement a more rigorous treatment of boundary effects. Towards this end, simulations of simple shear flows of identical mono-disperse spheres confined between parallel plates were performed and analyzed to formulate compact wall boundary conditions that can be used for dense frictional flows at flat frictional boundaries. The fourth phase explored the role of modest levels of cohesive interactions between particles on the dense phase rheology. The final phase of this project focused on implementation and testing of the modified kinetic theory in MFIX and running bin-discharge simulations as test examples.

Contents

1 EXECUTIVE SUMMARY

Dense granular flows, which occur in both natural and industrial processes, manifest several different flow regimes. Depending on the local solids volume fraction ϕ and shear rate $\dot{\gamma}$, one can observe any of three distinct flow regimes when non-cohesive particles are subjected to steady simple shear: (1) a quasi-static regime for ϕ exceeding the critical volume fraction ϕ_c in which pressure p and shear stress τ are independent of shear rate; (2) an inertial regime below ϕ_c in which $p, \tau \sim \dot{\gamma}^2$; and (3) an intermediate regime occurring in a narrow window of volume fractions about ϕ_c in which $p, \tau \sim \dot{\gamma}^n$ with $0.5 \leq n \leq 1$. This report summarizes the outcome of research aimed at developing continuum rheological models for dense granular flows that *bridges multiple regimes of flow*, implementing them in open-source platforms for gas-particle flows and performing test simulations.

The first phase of the research covered in this report involved implementation of a steady-shear rheological model that bridges quasi-static, intermediate and inertial regimes of granular flow, developed in the PIs research group, into MFIX (Multiphase Flow with Interphase eXchanges - a general purpose computer code developed at the National Energy Technology Laboratory). MFIX simulations of dense granular flows in hourglass-shaped hopper were then performed as test examples. It was found that the new rheological model implemented predicted rat-holing in the upper chamber of the hourglass as well as the formation of a sand-pile on the hour glass flow, both of which are consistent with experimental observations. In contrast, the standard kinetic theory predicted an unphysical bubble formation above the orifice, which is unexpected for such a dense flow; it also failed to predict pile formation.

The second phase of the research covered in this report dealt with formulation of a modified kinetic theory for frictional particles that can be used over a wider range of particle volume fractions and also apply for dynamic, multi-dimensional flow conditions. To guide this work, simulations of simple shear flow of identical mono-disperse spheres were performed using the discrete element method. Based on the simulation results, the modified kinetic theory was formulated by systematically modifying a widely used standard kinetic theory model for granular flows. Specifically, the modified kinetic theory recognizes that the particle volume fraction at jamming conditions depend on particle-particle friction coefficient, and incorporates a modified expression for the radial distribution function at contact that is consistent with the dense phase flow simulations. In addition, it introduces the notion of an effective restitution coefficient, which is a function of the usual normal restitution coefficient and the interparticle friction coefficient. It also ensures that in the dense limit, the ratio between shear stress and pressure reduces to an inertial-number model as has been recognized in the literature.

The third phase of the research covered in this report probed the interaction of frictional granular material and a flat frictional wall through simulations of simple shear flows of identical mono-disperse spheres confined between parallel plates. The simulation results were used to deduce compact wall boundary conditions. Specifically, a novel scaling based on granular viscosity was used to collapse data of the surface slip velocity, which includes rotational and translational velocity contributions; such a boundary condition would apply to contin-

uum simulations of granular flows where one models local-average translational and angular velocities of the particles. It was then followed by a separate relation for the rotational velocity of particles at the boundary, so that one can deduce a boundary condition just for the translational slip velocity at the boundary by combining the expressions for the surface slip and rotational velocity; such a boundary condition would apply to continuum simulations of granular flows where one evolves just the local-average translational velocity of the particles. In both these instances, the continuum model seeks to resolve the steep velocity variation in the boundary layer near the wall. In many practical applications, it is not appealing to have to resolve the boundary layer. With this in mind, a coarse-grained boundary condition that subsumes the boundary layer contribution into the boundary condition was formulated; this boundary condition applies for coarsely resolved flow simulation considering only translational motion, which is typical of the vast majority of applications.

The fourth phase of the research covered in this report explored the role of modest levels of cohesive interactions between particles on dense phase rheology through discrete element method simulations in periodic domains. It was found that when cohesive forces are included, all the three non-cohesive regimes, namely quasistatic, inertial, and intermediate regimes, persist. However, the inertial regime is bifurcated into two regimes: (a) a new rate-independent regime at lower scaled shear rates and (b) an inertial regime at higher scaled shear rates. New rheological models are then proposed to account for these changes due to cohesion.

The final phase of the research covered in this report focused on implementation and testing of the modified kinetic theory in MFIX as well as the open-source software OpenFOAM. Gravity discharge of particles from a bin was used as a test problem to assess the performance of the model and the codes. It was found that the modified kinetic theory predicted a discharge rate very close to the experimental value, while the standard kinetic theory predicted a much larger discharge rate. Thus, it was demonstrated that the dense granular rheology modifications introduced by the modified kinetic theory contribute to substantially lowering the discharge rate and bringing it in line with experimental data.

2 CONTEXT OF THE RESEARCH PROJECT

Dense granular flows are ubiquitous in both natural and industrial processes. They manifest three different flow regimes – commonly referred to as the quasi-static, inertial, and intermediate regimes – each of which exhibits its own dependences on solids volume fraction, shear rate, and particle-level properties. The differences in these regimes can be attributed to microscale phenomena, with quasi-static flows being dominated by enduring, frictional contacts between grains, inertial flows by grain collisions, and intermediate flows by a combination of the two. Existing constitutive models for the stress tend to focus on one or two regimes at a time. The PI's research group recently presented a rheological model for dense granular flows which captures stresses in all three regimes under *steady shear* conditions and the transitions between them. This proposal is aimed at: (1) implementation of this steady shear rheological model in MFIX (**M**ultiphase **F**low with **I**nterphase e**X**changes – a general purpose computer code developed at the National Energy Technology Laboratory) followed by validation against experimental and Discrete Element Method (DEM) simulation data for flows in hoppers, bins, chutes and dense fluidized beds, and (2) further development of the rheological model to allow for *dynamic* evolution of the stresses.

3 PROJECT OVERVIEW

The overall aim of the proposed project is to implement and validate a new granular stress model in MFIX while continuing to improve the model to capture more complex flow behavior. The proposed work consists of the following major goals.

Goal #1: Refine the steady-shear continuum rheological model for dense granular flows developed recently by the PI's group, and implement it into MFIX. Perform MFIX simulations of dense granular flows in hoppers and chutes, using this rheological model and no-slip and partial slip boundary conditions already available in MFIX. Examine the role of modest levels of cohesion on the steady-shear rheology.

Goal #2: Formulate a modified kinetic theory for frictional particles that can be used over a wider range of particle volume fractions and also apply for dynamic, multi-dimensional flow conditions. Implement this model in MFIX and assess the consequence of model refinement on flow characteristics in the test problems mentioned in Goal #1.

Goal #3: Develop improved wall boundary conditions for the particle phase that can be used for dense frictional flows at flat frictional boundaries and implement them in MFIX. Examine the effect of refined boundary conditions on flow characteristics in the test problems mentioned in Goal #1.

To achieve these goals, a combination of discrete particle simulations for model refinement and continuum simulations for testing proper implementation of the model in MFIX will be performed. The project is broken into five phases, as listed below:

The first phase calls for refinement of a steady-shear continuum rheological model for

dense granular flows developed recently by the research group, and its implementation into MFIX. MFIX simulations of dense granular flows in hourglass-shaped hoppers and chutes will then be performed as tests. These first-phase simulations would employ options for wall boundary conditions that already exist in MFIX.

The second phase would focus on formulation of a modified kinetic theory for frictional particles that can be used over a wider range of particle volume fractions and also apply for dynamic, multi-dimensional flow conditions. Towards this end, simulations of simple shear flows of identical mono-disperse spheres confined in periodically repeating domains would be performed using the discrete element method (DEM) implemented in the Large-scale Atomic/Molecular Massively Parallel Simulator (LAMMPS) developed by Sandia National Laboratories. Appropriate modifications to the standard kinetic theory of granular materials that would capture the simulations results over the entire range of particle volume fractions and friction coefficients would be identified.

The third phase of this project aims to develop and implement a more rigorous treatment of boundary effects. Towards this end, simulations of simple shear flows of identical mono-disperse spheres confined between parallel plates would be performed and analyzed to formulate compact wall boundary conditions that can be used for dense frictional flows at flat frictional boundaries.

The fourth phase would explore the role of modest levels of cohesive interactions between particles on the dense phase rheology. This was motivated by the fact that many particles used in energy-related industries do manifest varying levels of cohesive interactions. Based on results of DEM simulations including such interaction that would be conducted in this phase, the steady-shear continuum rheological model for dense granular flows developed in the first phase of this study would be generalized to account for cohesion.

The final phase of this project calls for implementation and testing of the modified kinetic theory and the newly developed wall boundary conditions in MFIX.

The overall project has been broken down into the set of tasks summarized below.

Task 1. Project Management and Planning

- **1.1.** Develop and maintain a comprehensive Project Management Plan that clearly identifies the organizational structure, roles and responsibilities of the project team members, technical scope, budget, schedule baselines, key milestones and decision points, cost and schedule control, and project risk management.
- **1.2.** Monitor progress on the Project Management Plan with respect to technical progress on each task, achievement of milestones and deliverables, Gantt chart schedule progress and financial comparisons to the budget.
- **1.3.** Provide reports according to the "Federal Assistance Reporting Checklist".

Task 2. Refinement of steady-shear rheological model for dense granular flows and its implementation in MFIX

- **2.1.** Perform DEM simulations of simple shear flows in periodic domains to gather

data at additional shear rates, volume fractions and friction coefficients to refine the steady-shear rheological model.

2.2. Implement this steady-shear rheological stress model in MFIX.

2.3. Test the implementation through MFIX simulations of hopper and chute flows.

Task 3. Development of modified kinetic theory model that is applicable over a wider range of particle volume fractions and its implementation in MFIX

3.1. Perform DEM simulations in periodic domains to gather data on stress over a wide range of volume fractions, friction coefficients and shear rates.

3.2. Formulate a modified kinetic theory to capture the rheological results obtained from the DEM simulations.

3.3. Implement this modified kinetic theory in MFIX.

3.4. Check the MFIX implementation through test simulations mentioned in subtask 2.3.

Task 4. Development of new wall boundary conditions for dense granular flows

4.1. Perform DEM simulations of bounded simple shear flows for an array of volume fractions, shear rates, and friction coefficients. Collect data on pressure, shear stress, actual and apparent slip velocities at the walls, particle volume fraction in the core region and the shear rate in the core region.

4.2. Develop expressions for boundary conditions in terms of volume fraction, shear rate, and particle properties.

4.3. Implement the new boundary conditions into MFIX.

4.4. Check the MFIX implementation through test simulations mentioned in subtask 2.3.

Task 5. Refinement of steady-shear rheological model for dense granular flows to include cohesion

5.1. Perform DEM simulations of simple shear flows of slightly cohesive particles in periodic domains to gather data at additional shear rates, volume fractions and friction coefficients and use the results to develop the steady-shear rheological model.

5.2. Implement this steady-shear rheological stress model in MFIX.

4 PROJECT MILESTONES AND STATUS

The eleven milestones for the proposed project are listed in the Table below.

Milestone #	Description	Completion Date	Revised Date
1	Submission of the updated Project Management Plan ***Status: Milestone achieved in a timely manner***	10/31/11	
2	Complete implementation of the *steady shear* rheological model in MFIX; carry out at least 2 MFIX simulations of hopper flows; complete at least 2 simulations of chute flows. ***Status: Milestone achieved in a timely manner***	6/30/12	
3	Complete at least 50 DEM simulations of shear flows of frictional particles in periodic domains to help develop a multi-dimensional modified kinetic theory of granular materials that is applicable over a wider range of conditions. ***Status: Milestone achieved in a timely manner***	12/31/12	
4	Propose a modified kinetic theory that applies for frictional particles undergoing time-dependent, multi-dimensional flows. ***Status: Milestone achieved in a timely manner***	3/31/13	
5	Complete at least 50 DEM simulations of wall-bounded shear flows of dense assemblies spanning the quasi-static and intermediate regimes. ***Status: Milestone achieved in a timely manner***	6/30/13	
6	Propose new boundary conditions at flat frictional boundaries to be employed in continuum model simulations. ***Status: Milestone achieved in a timely manner***	9/30/13	
7	Complete at least 50 DEM simulations of shear flows of cohesive, frictional particles in periodic domains and refine the steady-shear rheological model. ***Status: Milestone achieved in a timely manner***	12/31/13	
8	Complete MFIX implementation of modified kinetic theory mentioned in Milestone #4 and run at least 2 MFIX simulations of hopper or bin flows. ***Status: Milestone achieved in a timely manner***	3/31/14	11/30/14
9	Complete MFIX implementation of the improved boundary conditions mentioned in Milestone #6 and run at least 2 MFIX simulations of hopper or bin flows in conjunction with the simpler steady shear rheological model of Milestone #2. ***Status: Milestone not achieved***	6/30/14	4/30/15
10	Using the final model developed in this study – modified kinetic theory of Milestone #4 and wall boundary condition of Milestone #6, complete at least 2 MFIX simulations of hopper or bin flows, and at least 2 simulations of chute flows. ***Status: Milestone not achieved***	8/31/14	7/31/15
11	Complete Final Report ***Status: Milestone achieved in a timely manner***	9/30/14	9/30/15

5 TECHNICAL ACCOMPLISHMENTS

5.1 Accomplishment in Task 2

The first goal of this project was to conduct a series of steady state dense granular shear flow simulations in periodic domains and identify the dependence of pressure, stress ratio (defined as the ratio between the shear stress and pressure) in various regimes of flow. We then set out to formulate models to capture these rheological parameters in various regimes for various particle-particle friction coefficients, and bridge them into a model that can be used to bridge across all the regimes. The details of this work can be referred to the publication in Physics Review E [1], which is attached at Appendix A here.

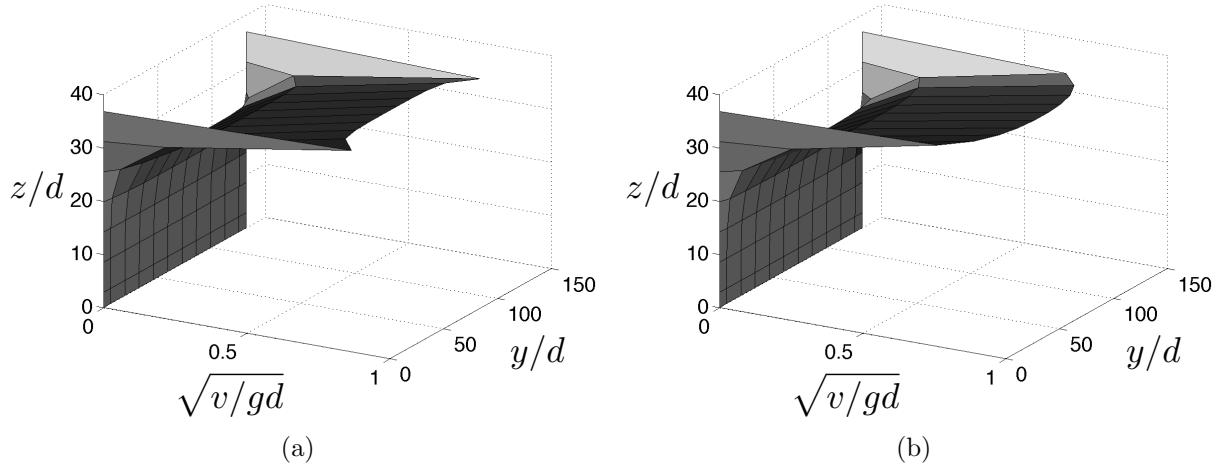

Figure 1: Velocity profiles for MFIX chute flow simulations using the steady-state rheological model with (a) no-slip and (b) partial-slip boundary conditions.

This steady-state model was implemented in MFIX and simulations of flow down an inclined plane with sidewalls were carried out. Figure 1(a) shows the velocity profile from a test simulation using the new rheological model paired with no-slip boundary conditions. The model predicts two salient features:

a) A stagnant layer is observed near the chute's bottom wall, which is consistent with experimental results of Jop et al. [2, 3].

b) The simulation also predicted and a concave velocity profile with spikes near the two sidewalls, which is not observed in experiments of Jop et al. [2, 3]. The occurrence of these velocity spikes is easily explained. No-slip boundary conditions result in large shear rates near the wall, which dilate the granular material and reduce the viscosity in this region, allowing for increased velocities.

However, when a partial-slip condition is used at the wall, the velocity spikes disappear as a result of decreased wall shear, and the convex profile observed in experiments is restored,

as illustrated in Figure 1(b). This behavior underscores the importance of investigating boundary conditions.

We also tested our steady shear rheological model [1] on the problem of flow in an hourglass, a commonly modeled type of hopper, using MFIX. In Figure 2, we present a comparison of predictions from the new model and MFIX's default model, a blending of the kinetic theory of Lun et al. [4] and an ad-hoc dense-regime stress. In both cases, the gas phase was considered, and no-slip boundary conditions were used for the solids. Beginning from an initial plug state with solids volume fraction of 0.586 (just below the critical volume fraction at which jamming occurs, which is 0.587 for an inter-particle friction coefficient of 0.5 [1]), the flow is observed to evolve differently using the two models. Notably, the new rheological model predicts rat-holing (i.e. persistent core flow) in the upper chamber of the hourglass as well as the formation of a sand-pile on the hourglass floor, both of which are consistent with experimental observations [5]. In contrast, the kinetic theory model predicts an unusual bubble formation above the orifice that one would not expect for such a dense flow and also fails to predict pile formation.

Simulations of the above kind using the steady state model based on steady shear rheology applicable only for dense regime were not pursued further as this model becomes less and less accurate as the volume fraction decreases. Instead, the focus shifted to research generalizing this model in the form of modified kinetic theory, which is task 3 in the project.

Milestone #2: Complete implementation of the steady shear rheological model in MFIX; carry out at least 2 MFIX simulations of hopper flows; complete at least 2 simulations of chute flows.

This milestone is associated with the task specified in this subsection. This milestone was completed, as illustrated above.

5.2 Accomplishment in Task 3

A large number of steady shear simulations of particles in periodic domains were carried out over a wide range of particle volume fractions covering both the dilute and dense flow regimes. Such simulations were carried out for several different values of particle-particle friction coefficient (μ) and coefficient of restitution (e). For each case, the system was sheared at various shear rates, and the corresponding average granular temperature, pressure, and shear stress ratio (ratio between shear stress and pressure) were extracted. Lee-Edwards boundary condition [6] was employed to achieve a linear velocity profile. Sample simulation results on steady-state granular temperature, pressure, and shear stress ratio are shown in Figure 3. The particle-particle friction coefficient of 0.5 is used in the simulations shown in this figure. The lines represent the model predictions from the modified kinetic theory developed in this project (MKT) [7]. Simulation results on other μ values can be referred to the attached paper in Appendix B.

MKT was developed based on the simulation results mentioned above. A complete description of MKT can be found in Table 1 of the attached paper in Appendix B. Briefly, the begins

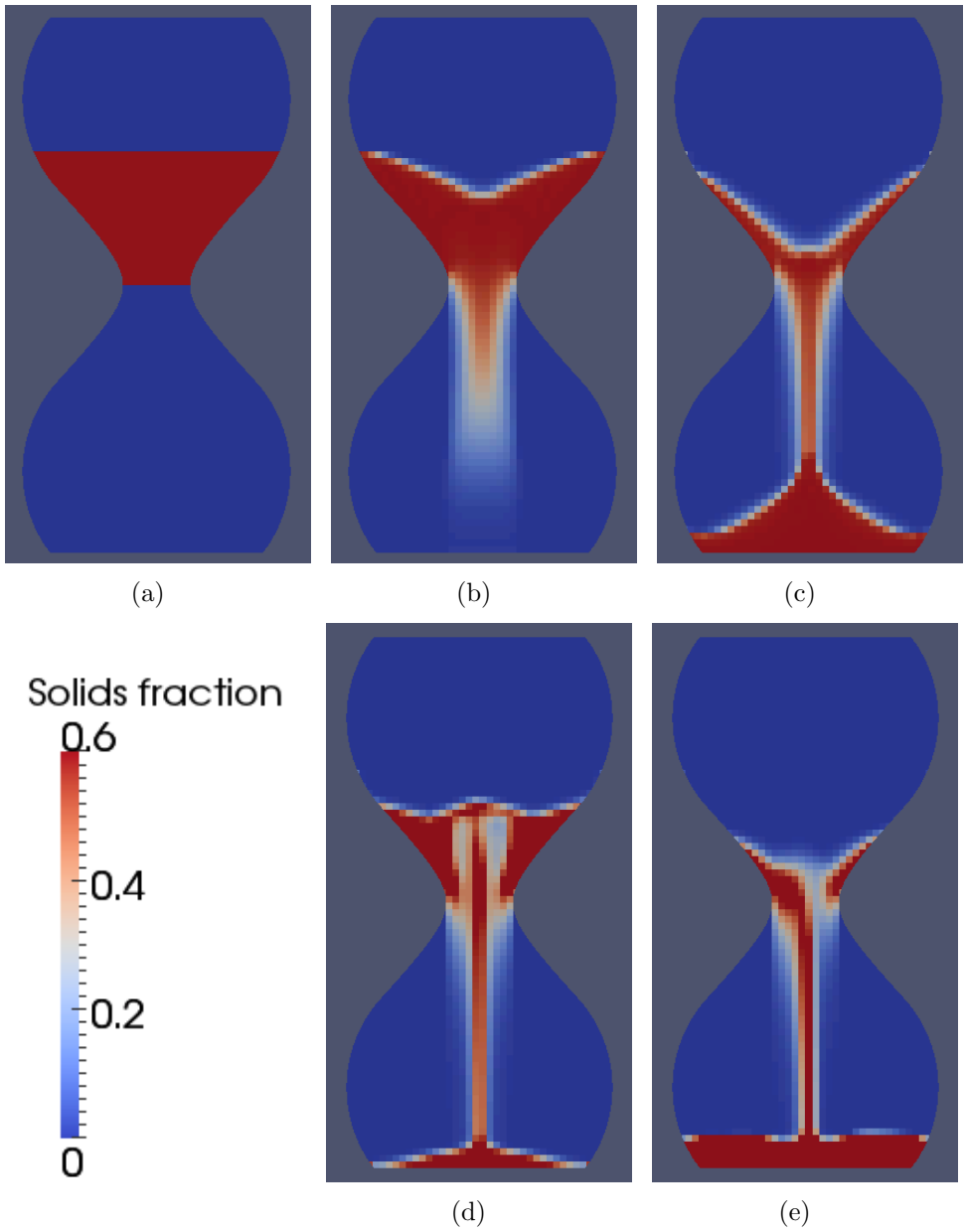

Figure 2: Snapshots of solids fraction from granular flow in an hourglass. Beginning from an initial state (a), a comparison is made between the predictions of the steady-state rheological model (b-c) and MFIX's default model (d-e). The new model predicts ratholing (core flow) in the upper chamber and pile formation on the hourglass floor, both in agreement with experimental observation. The default model produces anomalous bubbles above the orifice and an even layer on the floor.

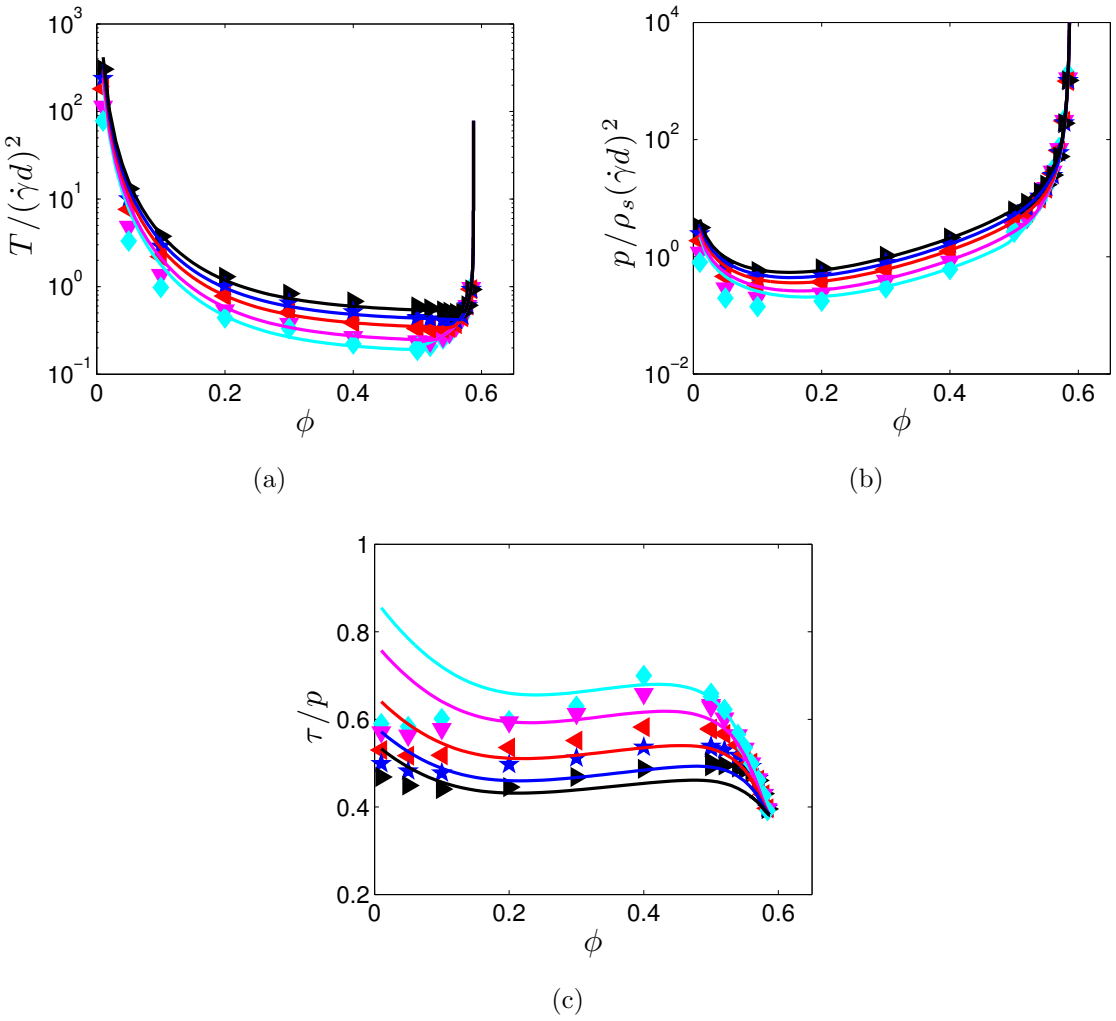

Figure 3: Comparison of the simulation results on (a) granular temperature (b) pressure (3) shear stress ratio with the proposed modified kinetic theory model. Particle-particle friction coefficient $\mu = 0.5$ is used.

with an existing kinetic-theory model for frictionless particles in dilute systems in order to extend it to handle frictional particles in both dilute and dense regimes. The approach to modifying the kinetic theory equations drew from the following strategies and is summarized as follows:

1. The temperature was captured by introducing a multiplicative correction factor δ_Γ to the energy dissipation term. This factor contains a dependence on an effective restitution coefficient $e_{\text{eff}} = e_{\text{eff}}(e, \mu)$ and would also diverge at jamming conditions, which depend on the magnitude of the friction coefficient.

2. The pressure was captured using a new expression for the radial distribution function at contact g_0 that would diverge at jamming conditions.

3. The shear stress was scaled by pressure and written as shear stress ratio $\eta \equiv \tau/p$. The

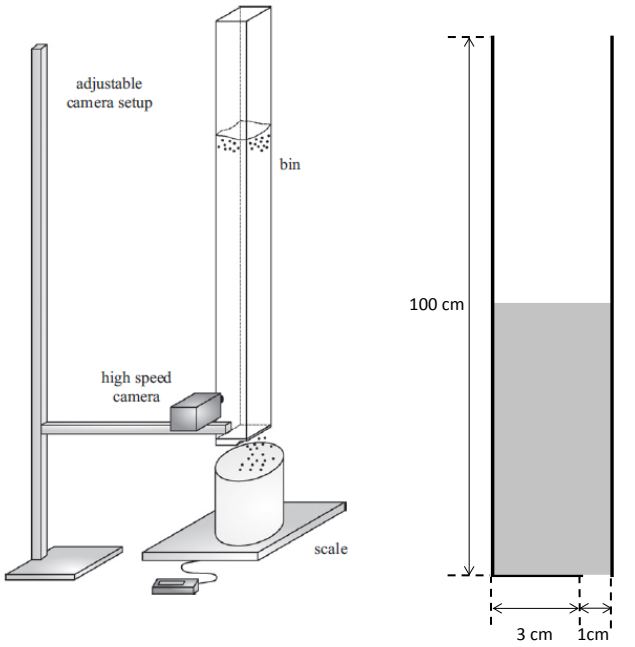

Figure 4: (a) Experimental setup of the system [10]. (b) The front view of the system. The width (not shown) of the system is 4 *cm*.

behavior of η was then captured with a second multiplicative factor δ_τ to the shear stress expression. This factor would force η to obey an inertial-number model [1, 8, 9, 2] in the dense regime, in particular requiring it to approach a yield stress ratio η_s at jamming conditions.

The MKT represents a simple and fruitful model to account for dynamic flow behavior. It falls in the category of an algebraic granular energy equation, as a dynamic evolution equation for the granular temperature is not solved.

The MKT has been successfully implemented both in OpenFOAM and in MFIX. It can be used to perform Euler-Euler simulations of gas-solid flows. Gravity discharge of particles from a bin, which has been experimentally investigated in the literature [10], is used as the test problem to assess the performance of the model and the codes. The experimental setup is described in Figure 4(a). Figure 4(b) is the diagram of the front view, which illustrates the dimensions. Particles are allowed to discharge from a 4 $cm \times 4$ $cm \times 100$ cm bin, through a 4 $cm \times 1$ cm orifice located at the bottom on one side of the bin. No-slip boundary condition is applied at the sidewalls for solid phase. No-slip boundary condition is also applied for gas phase. Table 1 lists the values of the model parameters used the example discussed below. Initially, particles are filled to a height of 50 cm in the bin at a solid volume fraction of 0.58. Simulations were done with different grid resolutions, but only a single example is presented here, where the grid size is 2.5 mm.

Table 1: Material properties.

Property	**Value**	**Units**
Particle diameter, d_p	0.875	mm
Particle friction coefficient, μ	0.3	–
Particle restitution coefficient, e_p	0.8	–
Particle density, ρ_s	2500	$kg\ m^{-3}$
Gas viscosity, μ_g	1.78×10^{-5}	$kg\ m^{-1}\ s^{-1}$
Gas density, ρ_g	1.224	$kg\ m^{-3}$

As shown in Figure 5, the discharge rate predicted using MKT implemented in OpenFOAM quickly reaches a nearly steady value, which is consistent with experiments [10]. Steady-state discharge rate is also observed using MKT implemented in MFIX. As shown in Table 2, MKT implemented in OpenFOAM predicts a discharge rate very close to the experimental value; in contrast, the Standard Kinetic Theory (SKT), which does not consider the corrections needed for dense granular flows as well as the role of frictional contact, predicts a much larger discharge rate. (See Table 2 under Standard Kinetic Theory. In both the MKT and SKT simulations, we employed the same radial distribution function model to ensure that the same jamming condition is used in both simulations.) Thus, the dense granular rheology modifications introduced by the MKT contribute to dramatically lowering the discharge rate and bringing it in line with experimental data. MKT implementation in MFIX yields a value that is somewhat different from that obtained using OpenFOAM implementation. The reason for this difference is still not understood and will be probed in the future. In any case, when compared to the difference between standard and modified kinetic theories, the difference seen between MKT implementation in OpenFOAM and MFIX is small.

Table 2: Discharge rates from experiments [10] and simulations using various models in OpenFOAM and MFIX

	Discharge rate (g/s)	
Experimental data [10]	165	
	OpenFOAM	MFIX
MKT [7]	166	120
SKT with g_0 expression of Chialvo et al. [7]	364	312

Milestone #3: Complete at least 50 DEM simulations of shear flows of frictional particles in periodic domains to help develop a multi-dimensional modified kinetic theory of granular materials that is applicable over a wider range of conditions.

Milestone #4: Propose a modified kinetic theory that applies for frictional particles undergoing time-dependent, multi-dimensional flows.

Milestone #8: Complete MFIX implementation of modified kinetic theory mentioned in Milestone #4 and run at least 2 MFIX simulations of hopper or bin flows.

These milestones are associated with the tasks mentioned above. They have all been completed and the milestones have been achieved.

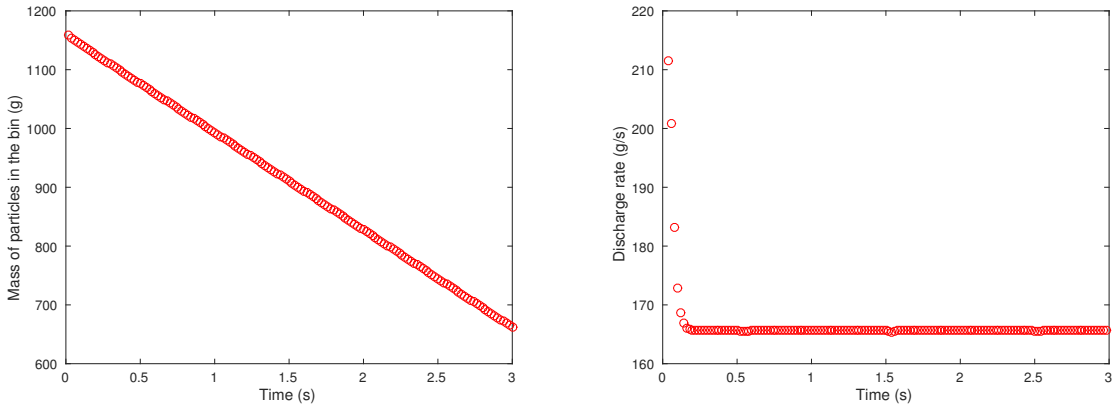

(a) (b)

Figure 5: (a) Mass of the particles in the bed versus time. (b) Discharge rate of particles versus time. The data are obtained using MKT [1] in OpenFOAM. Similar curves are obtained using MKT [1] in MFIX.

5.3 Accomplishment in Task 4

In order to probe boundary conditions (BC) that are suitable for dense granular flows, a number of simulations of shear flow of assemblies confined between flat, frictional walls have been performed to develop effective boundary conditions.

As described in previous works [11, 12], wall-bounded shear flows exhibit two regions of flow: 1) a central or *core* region characterized by spatially-invariant, local rheology and 2) a boundary region within about $10d$ of each wall featuring strong gradients in shear rate $\dot{\gamma}$ and volume fraction ϕ due to non-local conduction of granular energy. Indeed we observed these regions in our simulations, as demonstrated in Figure 6, where exponential tails towards the walls are clearly visible for the shear rate, volume fraction, and granular temperature. The measured pressure p and shear stress ratio η are found to obey local, inertial-number rheological behavior [1, 9] in the core region, as shown in Figure 7. This local behavior in the core supports the notion that a BC model that absorbs the near-wall behavior can be successfully coupled with a simple, local rheological model without the need for inclusion of further complexity to the rheology.

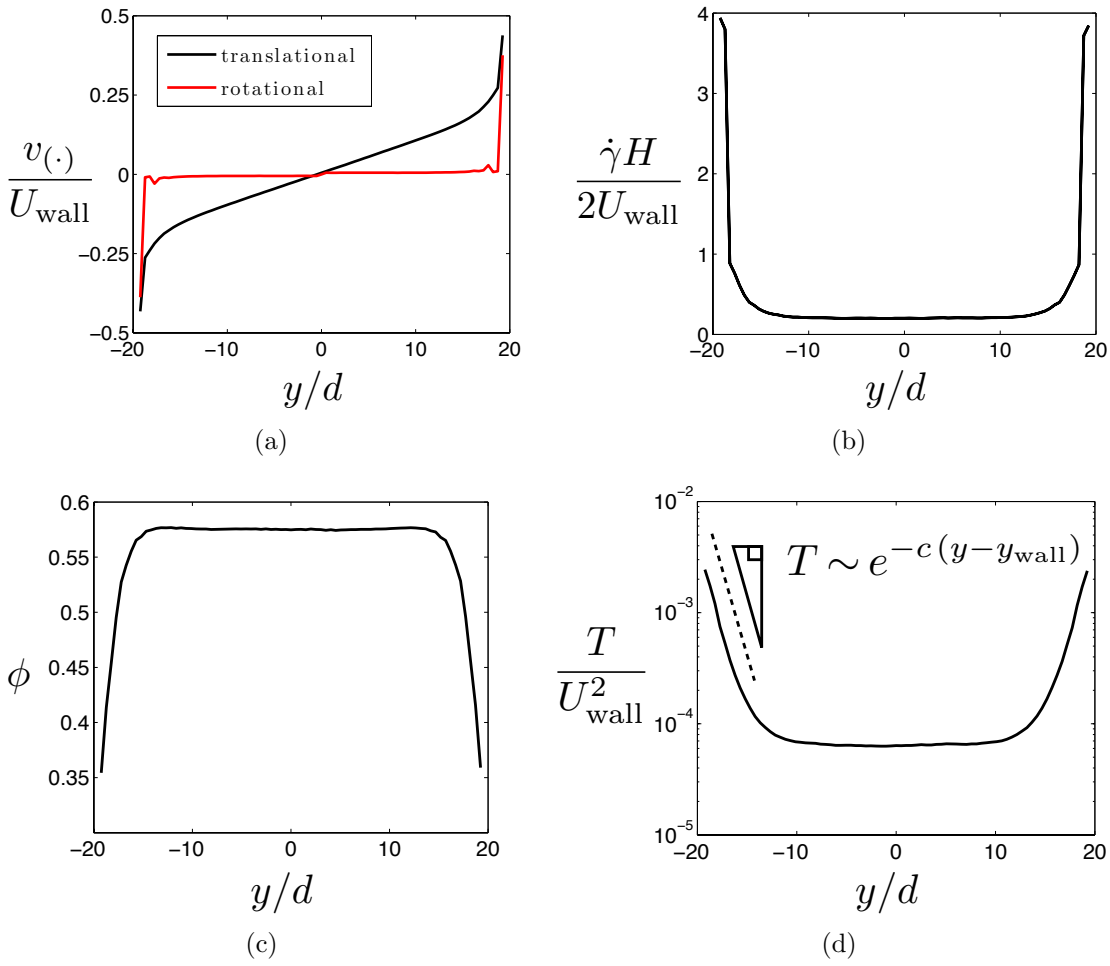

Figure 6: Profiles of (a) velocity, (b) shear rate, (c) volume fraction, and (d) granular temperature vs. position between wall boundaries for Hookean contact. The interparticle friction coefficient and wall-particle friction $\mu = \mu_w = 0.5$ and $\bar{\phi} = 0.55$. Quantities are scaled by wall velocity U_{wall} and gap width H. A core region with spatially invariant rheological properties is observed to lie between boundary layers of thickness $\sim 10d$ at each wall. Exponential tails are observed in the boundary layers. Analogous results were obtained for Hertzian contact model as well (not shown).

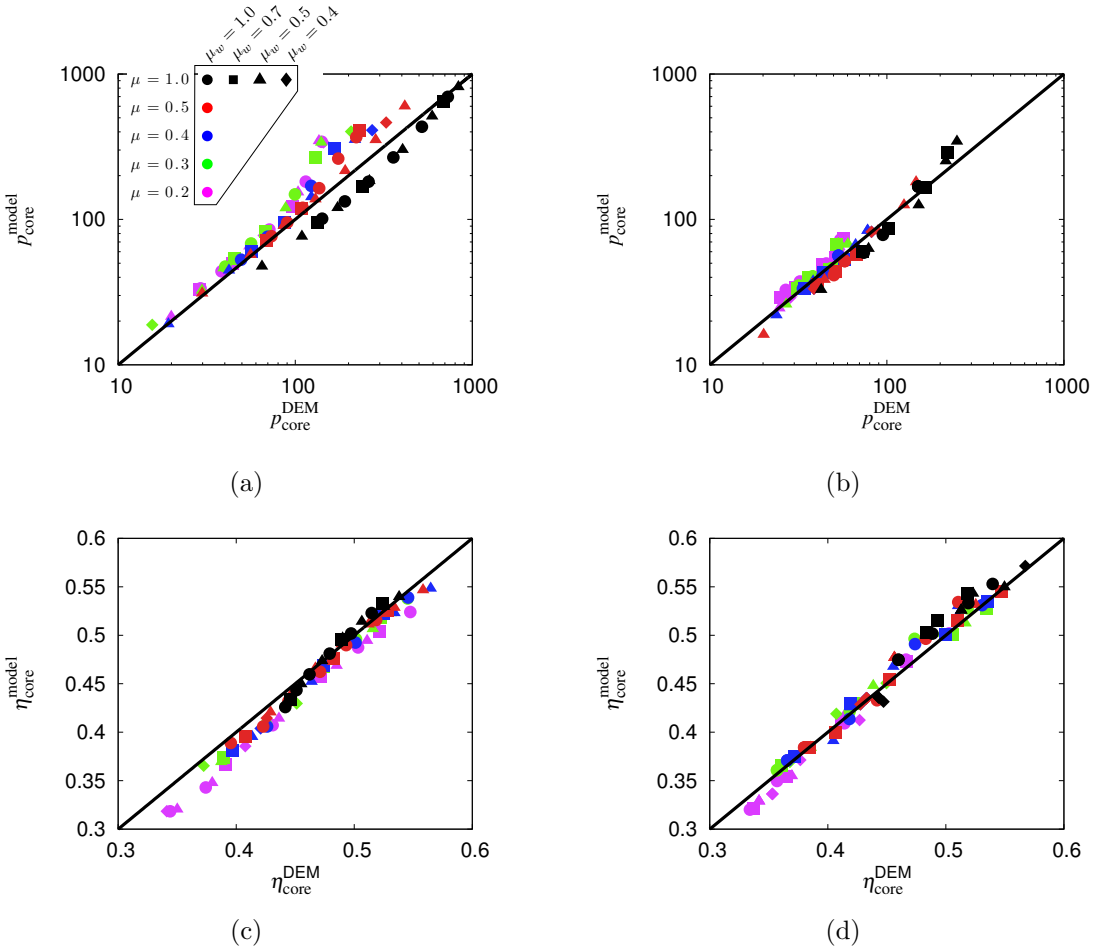

Figure 7: Comparison of core data for scaled pressure and shear stress ratio with predictions of the local rheological model of Chialvo *et al.* [1](Eqs. (7)-(10)) and Gu *et al.* [13] (Eqs. (6),(20)-(22)). (a) scaled pressure for Hookean contact versus the rheological model of Chialvo *et al.* [1], (b) scaled pressure for Hertzian contact versus the rheological model of Gu *et al.* [13], (c) shear stress ratio for Hookean contact versus the rheological model of Chialvo *et al.* [1], (d) shear stress ratio for Hertzian contact versus the rheological model of Gu *et al.* [13]. Reasonably good agreement confirms the locality of the rheological behavior in the core.

Based on these wall-bounded simple-shear simulations, we introduced a novel scaling based on granular viscosity and used it to collapse data of the 'surface' slip velocity, which includes rotational and boundary-layer velocity contributions, and proposed an empirical model for use in finely-resolved flow problems considering both translational and angular velocity fields. We then separately constituted the rotational contribution to produce a slip velocity model for use in finely-resolved, translation-only flow problems. Finally, we coarse-grained the model by subsuming the boundary-layer contribution into the boundary condition, in analogy to the wall functions used in turbulence modeling, to produce a constitutive expression for use in coarsely-resolved flows considering only translational motion — *i.e.* the vast majority of applications. The final versions of the model that can handle general flow problems are included in Eqns. (32–40) of the draft manuscript attached here as Appendix C.

Converting these results into an implementable boundary condition model is still proving to be a challenge. So, implementation of this boundary condition into OpenFOAM and MFIX could not be completed during this project; but work along this line will continue. Milestones 9 and 10 are therefore incomplete.

Milestone #5: Complete at least 50 DEM simulations of wall-bounded shear flows of dense assemblies spanning the quasi-static and intermediate regimes.

Milestone #6: Propose new boundary conditions at flat frictional boundaries to be employed in continuum model simulations.

Milestone #9: Complete MFIX implementation of the improved boundary conditions mentioned in Milestone #6 and run at least 2 MFIX simulations of hopper or bin flows in conjunction with the simpler steady shear rheological model of Milestone #2.

Milestone #10: Using the final model developed in this study – modified kinetic theory of Milestone #4 and wall boundary condition of Milestone #6, complete at least 2 MFIX simulations of hopper or bin flows, and at least 2 simulations of chute flows.

These milestones are associated with the tasks mentioned above. Tasks 4.1 and 4.2 have been completed. Milestones 5 and 6 are achieved. Tasks 4.3 and 4.4 are not completed, and Milestones 9 and 10 unachieved.

5.4 Accomplishment in Task 5

Simulations of granular shear flow were performed in periodic domains allowing for cohesive interaction between particles. They were performed for various shear rates, volume fractions, friction coefficients, and modified Bond numbers. As gravity is not included in the simulations, a modified Bond number Bo^* is defined as the ratio between the maximum net cohesive force experienced by a particle to a characteristic contact force, kd, where k is particle stiffness. Figure 8(a) plots the scaled pressure pd/k against the scaled shear rate $\hat{\dot{\gamma}} = \dot{\gamma}d/\sqrt{k/(\rho_s d)}$ for non-cohesive particles with particle friction coefficient $\mu = 0.1$. Three regimes are present [14, 1, 15, 16]: quasistatic at low shear rates and high volume fractions, inertial at low shear rates and low volume fractions, and intermediate at high shear rates and all volume fractions. The quasistatic and inertial regimes are separated by a critical volume fraction ϕ_c which is a function of μ. When cohesive forces are included, however, it is found that this regime map is modified, as shown in Figures 8(b) and (c), where Bo^* is 5×10^{-6} and 5×10^{-5} respectively. Some aspects remain unchanged: all three non-cohesive regimes persist with no change in $\phi_c(\mu)$, and the quasistatic and intermediate pressure values show no appreciable changes. However, the inertial regime is now bifurcated into two regimes occurring at different scaled shear rates: at higher $\hat{\dot{\gamma}}$ the flow remains inertial (i.e. exhibiting Bagnold scaling), while at lower $\hat{\dot{\gamma}}$ the flow becomes rate-independent. We term this latter, new regime the *cohesive regime*. As Bo^* increases, this cohesive regime expands to encompass a larger domain of $\hat{\dot{\gamma}}$, as illustrated in Figures 8(b) and (c).

In Figures 8, we present the results only from simulations in which the velocity profile in the statistical steady state is found to be linear indicating homogeneous shear. There

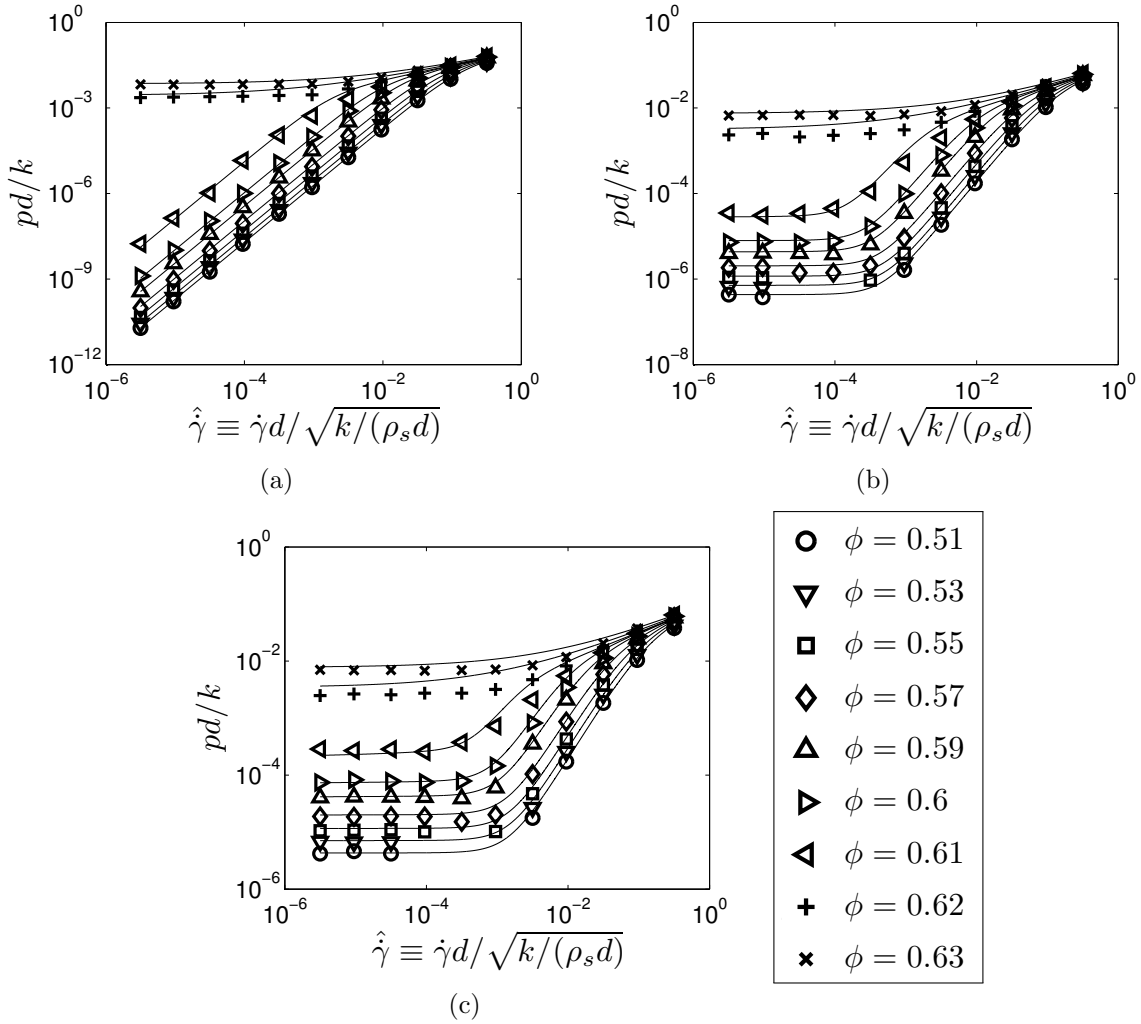

Figure 8: Scaled pressure versus scaled shear rate for (a) non-cohesive particles, (b) cohesive particles with $Bo^* = 5 \times 10^{-6}$, (c) cohesive particles with $Bo^* = 5 \times 10^{-5}$. In all cases, Hookean contact and van der Waals force model are used, and interparticle friction coefficient $\mu = 0.1$. Symbols denote simulation results, while lines denote model predictions from Eqns. (7–12) of the attached paper in Appendix D.

is a conspicuous absence of simulation results in Figures 8(b) and (c) at the lower volume fractions and shear rates in the region representing transition from cohesive regime to inertial regime. In this region, the velocity profiles are found to be inhomogeneous. These cases are not included in the analysis of the homogeneously sheared state presented here.

Blended stress models similar to the non-cohesive system [1] have been proposed for the cohesive granular flows. The model predictions using these models are denoted by lines in Figure 8, which describe the data well. The pressure and shear stress ratio models for the cohesive granular flows can be found in Eqns. (7–12) and Eqns. (13–15) (19) in the attached paper in Appendix D, respectively.

Milestone #7: Complete at least 50 DEM simulations of shear flows of cohesive, frictional particles in periodic domains and refine the steady-shear rheological model.

This milestone is associated with the task specified in this subsection. This milestone was completed, as illustrated above.

6 PROBLEMS ENCOUNTERED

Implementation of the model in MFIX led to unexpected challenges. Only recently did we manage to resolve this challenge, with much help from Dr. Tingwen Li of National Energy Technology Laboratory, Morgantown. In view of this challenge, we set out to implement the model in OpenFOAM, which we could complete quite readily.

While our DEM simulations have led to good insights on the flow behavior in the boundary layer close to the wall, we have still not succeeded in reducing the highly non-linear correlations we came up with into usable boundary conditions. As a result, the project failed to complete the boundary condition implementation in MFIX or OpenFOAM.

7 PUBLICATIONS AND PRESENTATIONS

The following publications and presentations were made during the course of this project.

Publications

1. S. Chialvo, A. Ozel, O. Bonnefoy, and S. Sundaresan. Boundary conditions for dense, wall-bounded ows of granular material. (under preparation)
2. Y. Gu, S. Chialvo, and S. Sundaresan. Rheology of cohesive granular materials across multiple dense-flow regimes. *Physical Review E* **90**, 032206 (2014).
3. S. Chialvo and S. Sundaresan. A modified kinetic theory for frictional granular flows in dense and dilute regimes. *Physics of Fluids* **25**, 070603 (2013).
4. S. Chialvo, J. Sun, and S. Sundaresan. Bridging the rheology of granular flows in three regimes. *Physical Review E* **85**, 021305 (2012).

Presentations

1. Y. Gu, A. Ozel and S. Sundaresan. Implementation of a modified kinetic theory model for frictional granular Flows. *AIChE Annual Meeting*. Salt Lake City, UT, 11 November 2015.
2. Y. Gu, S. Chialvo and S. Sundaresan. Implementation and refinement of a comprehensive model for dense granular flows. *2014 NETL Cross-cutting Research Review Meeting*. Pittsburgh, PA, 19-23 May 2014.
3. S. Chialvo and S. Sundaresan. Implementation and refinement of a comprehensive model for dense granular flows. *University Coal Research Contractors Review Conference*. Pittsburgh, PA, 13 June 2013.
4. Y. Gu, S. Chialvo and S. Sundaresan. Rheology of cohesive granular materials across multiple dense flow regimes. *AIChE Annual Meeting*. San Francisco, CA, 5 November 2013.
5. S. Chialvo and S. Sundaresan. Effective wall-boundary conditions for dense flows of granular materials *AIChE Annual Meeting*. San Francisco, CA, 4 November 2013.
6. S. Chialvo and S. Sundaresan. A modified kinetic theory for frictional granular flows in dense and dilute regimes. *APS Division of Fluid Dynamics Annual Meeting*. San Diego, CA, 19 November 2012.
7. S. Chialvo and S. Sundaresan. A modified kinetic-theory model bridging dense and dilute regimes of frictional granular flow. *AIChE Annual Meeting*. Pittsburgh, PA, 30 October 2012.

8. S. Chialvo and S. Sundaresan. Implementation and Refinement of a Comprehensive Model for Dense Granular Flows. *University Coal Research Contractors Review Conference*. Pittsburgh, PA, 31 May 2012.

9. S. Chialvo and S. Sundaresan. Modified kinetic theory for flows of frictional granular materials. *NETL Conference on Multiphase Flow Science*. Morgantown, WV, 22 May 2012.

10. S. Chialvo and S. Sundaresan. An introduction to the evolution of debate concerning the intermediate regime. *IUTAM Symposium on Mobile Particulate Systems: Kinematics, Rheology and Complex Phenomena*. Bangalore, India, 25 January 2012.

11. S. Chialvo, J. Sun, and S. Sundaresan. Rheology of dense granular flows: regime bridging and implications for kinetic theory. *IUTAM Symposium on Mobile Particulate Systems: Kinematics, Rheology and Complex Phenomena*. Bangalore, India, 25 January 2012.

12. S. Chialvo, J. Sun, and S. Sundaresan. Bridging the rheology of granular flows in three regimes. *Annual Meeting of the American Physical Society Division of Fluid Dynamics*. Baltimore, MD, 21 November 2011.

13. S. Chialvo, J. Sun, and S. Sundaresan. Bridging the rheology of granular flows in three regimes. *Princeton University Department of Chemical and Biological Engineering Graduate Student Symposium*. Princeton, NJ, 28 October 2011.

8 PARTICIPANTS IN THE PROJECT

- Prof. Sankaran Sundaresan (**PI**)
- Sebastian Chialvo: graduate student in Chemical Engineering
- Yile Gu: graduate student in Chemical Engineering
- Ali Ozel: research associate in Chemical Engineering

References

[1] S. Chialvo, J. Sun, and S. Sundaresan, "Bridging the rheology of granular flows in three regimes," *Physical Review E*, vol. 85, p. 021305, feb 2012.

[2] P. Jop, Y. Forterre, and O. Pouliquen, "A constitutive law for dense granular flows.," *Nature*, vol. 441, pp. 727–730, 2006.

[3] P. Jop, Y. O. Forterre, and O. Pouliquen, "Crucial role of sidewalls in granular surface flows: consequences for the rheology," *J. Fluid Mech.*, vol. 541, no. -1, pp. 167–192, 2005.

[4] C. K. K. Lun, S. B. Savage, D. J. Jeffrey, and N. Chepurniy, "Kinetic theories for granular flow: inelastic particles in Couette flow and slightly inelastic particles in a general flowfield," *J. Fluid Mech.*, vol. 140, pp. 223–256, 1984.

[5] R. M. Nedderman, *Statics and Kinematics of Granular Materials*. Cambridge: Cambridge University Press, 1992.

[6] A. W. Lees and S. F. Edwards, "The computer study of transport processes under extreme conditions," *J. Phys. C*, vol. 5, no. 15, p. 1921, 1972.

[7] S. Chialvo and S. Sundaresan, "A modified kinetic theory for frictional granular flows in dense and dilute regimes," *Physics of Fluids*, vol. 25, no. 7, p. 070603, 2013.

[8] G. D. R. MiDi, "On dense granular flows," *Eur. Phys. J. E*, vol. 14, pp. 341–365, 2004.

[9] F. da Cruz, S. Emam, M. Prochnow, J.-N. Roux, and F. Chevoir, "Rheophysics of dense granular materials: Discrete simulation of plane shear flows," *Phys. Rev. E*, vol. 72, p. 21309, aug 2005.

[10] S. Schneiderbauer, A. Aigner, and S. Pirker, "A comprehensive frictional-kinetic model for gas–particle flows: Analysis of fluidized and moving bed regimes," *Chem. Eng. Sci.*, vol. 80, no. 0, pp. 279–292, 2012.

[11] C. S. Campbell, "Boundary interactions for two-dimensional granular flows. Part 1. Flat boundaries, asymmetric stresses and couple stresses," *Journal of Fluid Mechanics*, vol. 247, pp. 111–136, 1993.

[12] Z. Shojaaee, J.-N. Roux, F. b. ç. Chevoir, and D. E. Wolf, "Shear flow of dense granular materials near smooth walls. I. Shear localization and constitutive laws in the boundary region," *Phys. Rev. E*, vol. 86, p. 11301, jul 2012.

[13] Y. Gu, S. Chialvo, and S. Sundaresan, "Rheology of cohesive granular materials across multiple dense-flow regimes," *Phys. Rev. E*, vol. 90, p. 32206, sep 2014.

[14] C. S. Campbell, "Granular shear flows at the elastic limit," *J. Fluid Mech.*, vol. 465, pp. 261–291, 2002.

[15] M. Otsuki and H. Hayakawa, "Critical scaling near jamming transition for frictional granular particles," *Phys. Rev. E*, vol. 83, p. 51301, may 2011.

[16] G. Lois and J. M. Carlson, "Force networks and the dynamic approach to jamming in sheared granular media," *Europhys. Lett.*, vol. 80, no. 5, p. 58001, 2007.

9 Appendix A

Please see the next page for the manuscript "Bridging the rheology of granular flows in three regimes," which was published in *Physical Review E*.

Bridging the rheology of granular flows in three regimes

Sebastian Chialvo,[1] Jin Sun,[2] and Sankaran Sundaresan[1]

[1]*Chemical and Biological Engineering Department, Princeton University, Princeton, New Jersey 08540, USA*

[2]*Institute for Infrastructure and Environment, University of Edinburgh, Edinburgh EH9 3JL, Scotland, United Kingdom*

(Received 16 March 2011; revised manuscript received 14 November 2011; published 13 February 2012)

We investigate the rheology of granular materials via molecular dynamics simulations of homogeneous, simple shear flows of soft, frictional, noncohesive spheres. In agreement with previous results for frictionless particles, we observe three flow regimes existing in different domains of particle volume fraction and shear rate, with all stress data collapsing upon scaling by powers of the distance to the jamming point. Though this jamming point is a function of the interparticle friction coefficient, the relation between pressure and strain rate at this point is found to be independent of friction. We also propose a rheological model that blends the asymptotic relations in each regime to obtain a general description for these flows. Finally, we show that departure from inertial number scalings is a direct result of particle softness, with a dimensionless shear rate characterizing the transition.

DOI: 10.1103/PhysRevE.85.021305 PACS number(s): 45.70.−n, 47.57.Gc, 64.60.F−, 64.70.ps

I. INTRODUCTION

Flows of granular matter occur in numerous geophysical and industrial processes and, as such, have garnered the attention of researchers for many years. Early efforts to describe these flows focused on either dilute flows (where kinetic theories [1–4] apply and which belong to the *inertial* regime) or very dense, slow flows (or *quasistatic* flows, for which plasticity models [5,6] can be used). However, attention has turned recently to the interface between these two regimes in the context of a jamming transition, proposed to occur in granular and other soft matter [7]. Of particular interest are several works that find a critical rheology around this transition in flows of frictionless, soft spheres [8–12] and disks [13,14]. Furthermore, they find scalings for the mean normal and shear stresses with respect to volume fraction that apply over a wide range of volume fractions and shear rates. Granular materials, though, are typically considered stiff, frictional materials, and to date there has been little work on identifying a critical rheology [15,16] for such matter despite significant progress in understanding their static jamming behavior [17–20]. In this paper, we investigate the rheology of frictional granular matter about the jamming transition and discuss the construction of a rheological model for flows in the quasistatic, inertial, and *intermediate* (i.e., critical) regimes.

II. SIMULATION METHODS

We perform computer simulations using a package of the discrete element method (DEM) [21] implemented in the molecular dynamics package LAMMPS [22]. In DEM, particles interact only via repulsive, finite-range contact forces. We employ a spring-dashpot model, for which the normal and tangential forces on a spherical particle i resulting from the contact of two identical spheres i and j are

$$\mathbf{F}_{ij}^{n} = f(\delta/d)\left[k_n \delta_{ij}\mathbf{n}_{ij} - \gamma_n m_{\text{eff}}\mathbf{v}_{ij}^{n}\right], \tag{1}$$

$$\mathbf{F}_{ij}^{t} = f(\delta/d)\left[-k_t \mathbf{u}_{ij}^{t} - \gamma_t m_{\text{eff}}\mathbf{v}_{ij}^{t}\right], \tag{2}$$

for overlap distance δ_{ij}, particle diameter d, spring stiffness constants k_n and k_t, viscous damping constants γ_n and γ_t, effective mass $m_{\text{eff}} = m_i m_j/(m_i + m_j)$ for particle masses m_i and m_j, relative particle velocity components $\mathbf{v}_{ij}^{n}$ and $\mathbf{v}_{ij}^{t}$, and elastic shear displacement $\mathbf{u}_{ij}^{t}$. A linear spring-dashpot (LSD) model is chosen by setting the function $f(x) = 1$, while a Hertzian model is set by $f(x) = \sqrt{x}$; the LSD model will be used throughout this paper except where noted explicitly. By Newton's third law, particle j experiences the force $\mathbf{F}_{ji} = -\mathbf{F}_{ij}$. Particle sliding occurs when the Coulomb criterion $|\mathbf{F}_{ij}^{t}| < \mu|\mathbf{F}_{ij}^{n}|$ is not satisfied for particle friction coefficient μ. Additionally, after setting $k_t/k_n = 2/7$ and $\gamma_t = 0$, we set γ_n such that the restitution coefficient $e = \exp(-\gamma_n\pi/\sqrt{4k_n/m_{\text{eff}} - \gamma_n^2}) = 0.7$ in the LSD case.

Using the above contact model, assemblies of about 2000 particles in a periodic box are subjected to homogeneous steady simple shear at a shear rate $\dot{\gamma}$ via the Lees-Edwards boundary condition [23]. The box size, and hence the solids volume fraction ϕ, are kept constant for each simulation. The macroscopic stress tensor is calculated as

$$\boldsymbol{\sigma} = \frac{1}{V}\sum_i \left[\sum_{j\neq i}\frac{1}{2}\mathbf{r}_{ij}\mathbf{F}_{ij} + m_i(\mathbf{v}_i')(\mathbf{v}_i')\right], \tag{3}$$

where V is the box volume, $\mathbf{r}_{ij}$ is the center-to-center contact vector from particle j to particle i, and $\mathbf{v}_i'$ is the particle velocity relative to its mean streaming velocity; from this result, an ensemble-averaged pressure $p = (\sigma_{xx} + \sigma_{yy} + \sigma_{zz})/3$ and shear stress $\tau = \sigma_{xz}$ can be extracted. All macroscopic quantities will be presented in dimensionless form, scaled by some combination of the particle diameter d, stiffness $k = k_n$, and solid density ρ_s. Since particles are assumed to overlap without deformation, we ensure that the average overlap is small (i.e., $\delta/d \approx pd/k \lesssim 0.07$).

III. FLOW REGIMES

We performed a series of simple shear simulations over a range of shear rates and volume fractions reaching into all three flow regimes and for several particle friction coefficients between 0 and 1. Figure 1 shows the scaled pressure pd/k versus the scaled shear rate $\hat{\dot{\gamma}} = \dot{\gamma}d/\sqrt{k/(\rho_s d)}$ at various volume fractions for (a) $\mu = 0.5$ and (b) $\mu = 0.1$. At low shear rates, there is an observed separatrix occurring at a

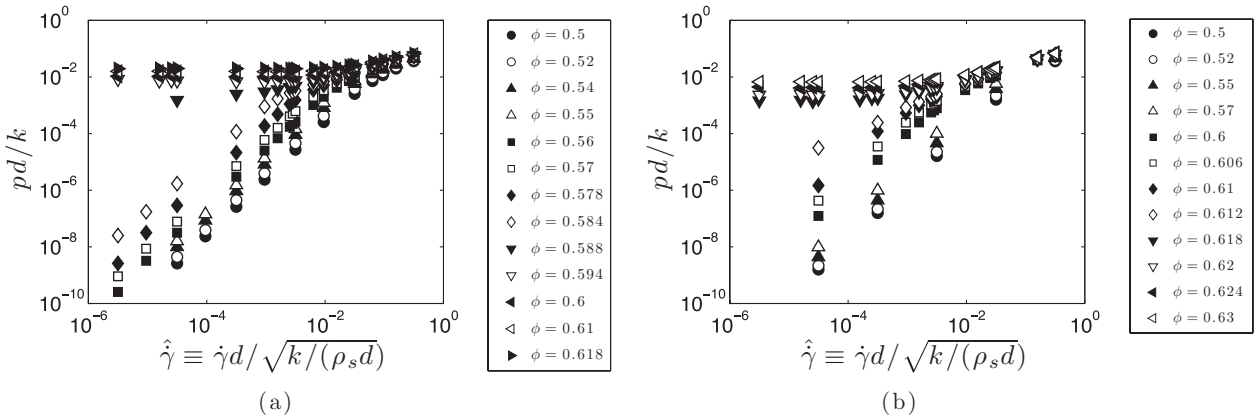

FIG. 1. Dimensionless pressure vs dimensionless shear rate for various volume fractions with (a) $\mu = 0.5$ and (b) $\mu = 0.1$. In both cases, three flow regimes are observed, each with the scalings $p \sim \dot{\gamma}^m$: a quasistatic regime with $m = 0$, an inertial regime with $m = 2$, and an intermediate regime with $m \approx 1/2$. At low $\hat{\dot{\gamma}}$, a critical volume fraction ϕ_c separates the quasistatic and inertial regimes; values of $\phi_c(\mu)$ are given in Table I.

critical volume fraction ϕ_c, which we identify as the jamming point; stresses scale quadratically with shear rate below ϕ_c but show no rate dependence above it. These two bands correspond to the inertial and quasistatic regimes, respectively. As shear rate increases, the quasistatic and inertial isochores approach a shared asymptote characteristic of the critical point in which dependence on the volume fraction vanishes; this region corresponds to the intermediate regime. Interestingly, the intermediate asymptote appears to be independent of the friction coefficient, in contrast to results at lower shear rates and despite the fact that $\phi_c = \phi_c(\mu)$. Values of ϕ_c for different cases of μ are presented in Table I. It should be noted that these critical values inferred from dynamical behavior of sheared systems are unique for each case of μ and hence may differ from the jamming points of static packings, which are not unique and depend on the compactivity [18].

A better understanding of the regime transitions can be gained by constructing a regime map, or "phase diagram," from the slopes of the curves in Fig. 1. Such a map is shown in Fig. 2. The intermediate regime is observed to lie in a window centered around $\phi = \phi_c$, and the width of this window is dependent on the value of the dimensionless shear rate. This feature has important implications for the modeling of dense granular flows. The large stiffness of granular materials such as sand or glass beads has been used to justify the modeling of granular particles as (infinitely) hard spheres. For such particles, dimensional analysis requires the traditional Bagnold scaling of the stresses (i.e., $p, \tau \sim \dot{\gamma}^2$), thereby rendering the intermediate and quasistatic regimes impossible. This picture is consistent with the vanishing of the intermediate regime observed in Fig. 2 as $k \to \infty$. However, real granular materials do nevertheless have a finite stiffness. Therefore, in the context of building a general rheological model for granular flows, it is preferable to choose a framework that includes all three regimes.

Another important observation from Fig. 2 is the smoothness of the transitions between the regimes. This feature suggests that purely quasistatic, inertial, or intermediate flow is achieved only in certain limits. As $\hat{\dot{\gamma}} \to 0$, we see quasistatic flow for $\phi > \phi_c$, inertial flow for $\phi < \phi_c$, and intermediate flow at $\phi = \phi_c$. We also see intermediate flow as $\hat{\dot{\gamma}} \to \infty$ for all volume fractions over the wide range examined in this study. The smooth transitions also suggest that the rheology at a particular $(\dot{\gamma}, \phi)$ is a composite of contributions from low-$\hat{\dot{\gamma}}$ and high-$\hat{\dot{\gamma}}$ behaviors, and this notion will play a large role in our construction of a rheological model.

TABLE I. Estimates of the critical volume fraction ϕ_c for different cases of the interparticle friction coefficient. The value of ϕ_c for the frictionless case agrees with the experimentally determined result of Nordstrom [10].

μ	0.0	0.1	0.3	0.5	1.0
ϕ_c	0.636	0.613	0.596	0.587	0.581

IV. CRITICAL VOLUME FRACTION ϕ_c

Because ϕ_c plays such an important role in governing the rheology in each of the three flow regimes, accurate estimation of its value for each case of μ is required for the construction of a valid rheological model. However, this task is made

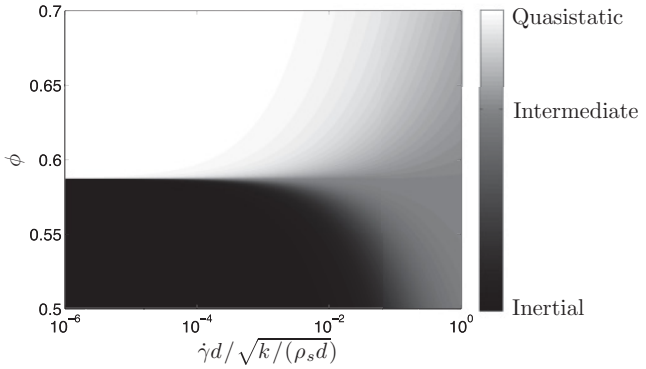

FIG. 2. Regime map for $\mu = 0.5$, with volume fraction vs dimensionless shear rate. The intermediate regime occurs only at ϕ_c in the limit $\hat{\dot{\gamma}} \to 0$ but emerges from this point to encompass all volume fractions as $\hat{\dot{\gamma}} \to \infty$.

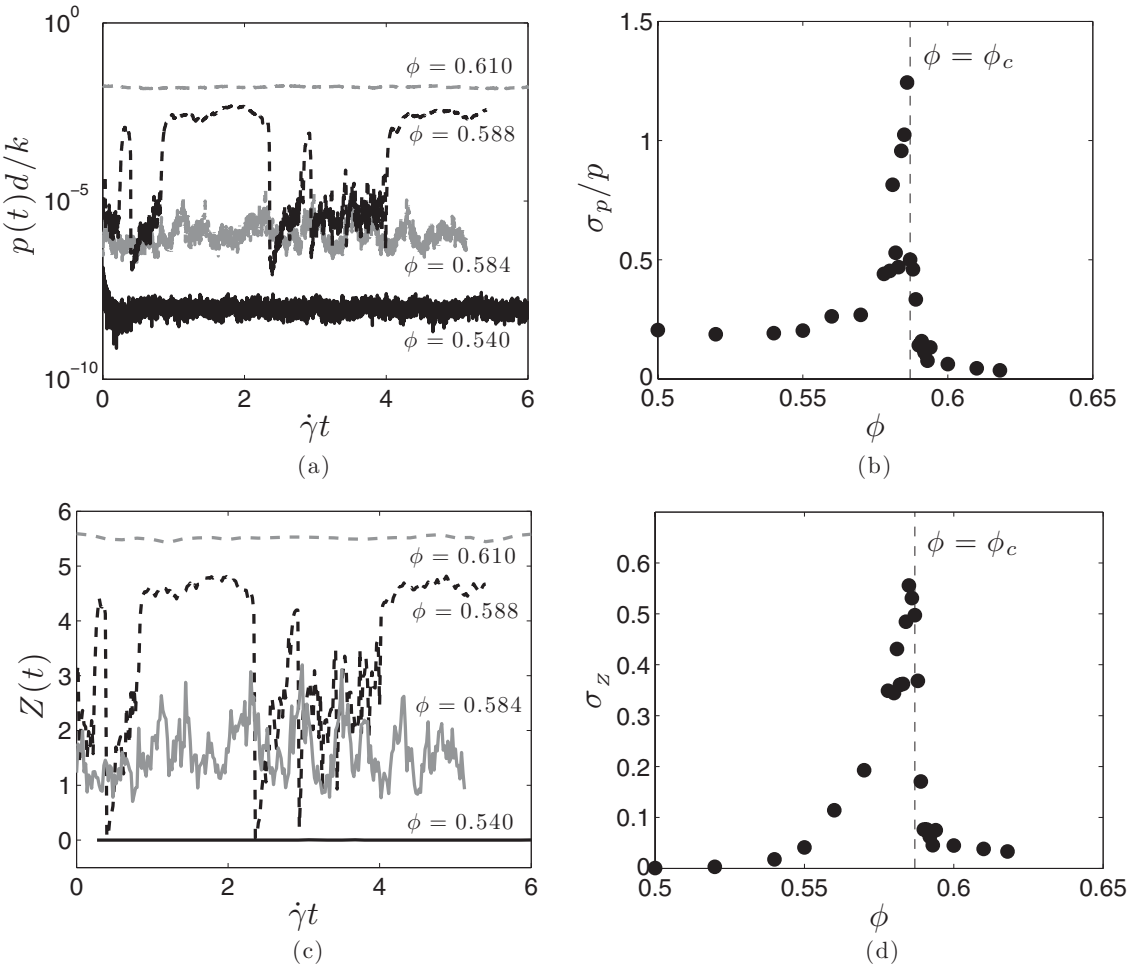

FIG. 3. Characteristics of the critical point for $\mu = 0.5$ and $\dot{\hat{\gamma}} = 3.2 \times 10^{-5}$. (a) Pressure fluctuations in time are observed to become larger near the critical point. (b) The standard deviation of pressure, scaled by the mean pressure, exhibits a spike at ϕ_c. [(c), (d)] The coordination number fluctuations are similar to those of the pressure in terms of both dynamics and ϕ dependence.

difficult by fluctuations of our measurements in time t. We observe a propensity for assemblies near ϕ_c to form and break force chains intermittently during the shearing process, resulting in stress fluctuations of several orders of magnitude as seen in Fig. 3(a). Though fluctuations occur at all volume fractions, their size relative to the mean is markedly large near the critical point. In Fig. 3(b) the standard deviation $\sigma_p \equiv \sqrt{\langle p^2(t)\rangle - \langle p(t)\rangle^2}$ of the pressure, when scaled by the time-averaged pressure p, exhibits a spike centered slightly under ϕ_c. This phenomenon increases the potential error in the time-averaged stress values near the critical point, thereby limiting the precision of our ϕ_c estimates to within about ± 0.001.

Additionally, though ϕ_c is certainly an important quantity, it is not necessarily the only or even the most influential parameter describing the jamming transition. The fact that stress can vary significantly at a constant volume fraction indicates that, while ϕ is a useful predictor of time-averaged stresses, other state variables may be more suitable for predicting instantaneous stresses. This quality has been observed previously with the coordination number $Z(t)$, for example, which was shown to exhibit a one-to-one correspondence with $p(t)$ in the quasistatic regime [24]. Indeed, we observe that $p(t)$ and $Z(t)$ exhibit the same qualitative evolution in time [Fig. 3(c)] and a similar ϕ dependence in their fluctuations [Fig. 3(d)]. Here we define $Z(t) \equiv 2N_c(t)/N$ for N_c contacts occurring in the N-particle assembly. The $p(t)$-$Z(t)$ relationship suggests that the critical point is better defined by some critical coordination number Z_c. However, because our goal is the construction of a *steady-state* rheological model, it is convenient to ignore all dynamics and assume that Z_c and ϕ_c correspond to the same conditions. We therefore proceed with ϕ_c as the definition of the critical point for our model.

In addition to being a function of μ, the critical point has also been proposed to change with the restitution coefficient e [25], and such a $\phi_c(e)$ has been used in a kinetic theory for frictional particles [26]. However, our DEM results do not support this conclusion, especially for frictional particles. As seen in Figs. 4(a) and 4(b) for $\mu = 0.5$ and $\mu = 0.1$, the spike in the pressure fluctuations occurs at the same volume fraction for a given μ regardless of the value of e, suggesting that $\phi_c = \phi_c(\mu)$ only. Even for the frictionless case [Fig. 4(c)], where fluctuations tend to occur over a wider range of volume fractions, there is no clear trend in the peak toward lower ϕ. One possible reason for the discrepancy is

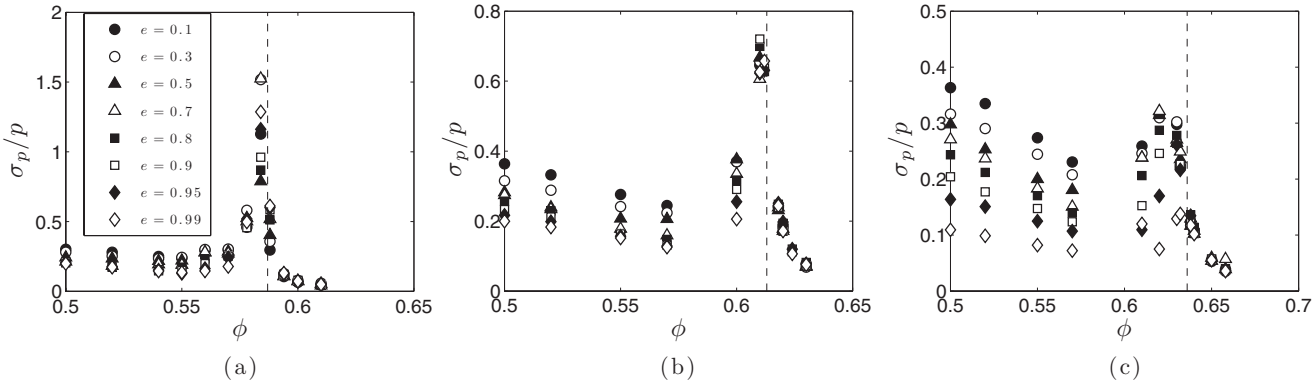

FIG. 4. Effect of changing the restitution coefficient on the pressure fluctuations for $\hat{\dot{\gamma}} = 3.2 \times 10^{-5}$. Dotted lines demarcate the critical point ϕ_c. For (a) $\mu = 0.5$ and (b) $\mu = 0.1$, the location of the spike in pressure fluctuations is independent of e. (c) Even for the frictionless case, there is little evidence to suggest $\phi_c = \phi_c(e)$.

the methods used for determining ϕ_c. Because hard-sphere codes, used in Ref. [25], prohibit particle overlaps, they are unable to simulate sheared particle systems near or above ϕ_c [27]. This shortcoming limits the performable simulations to one side of ϕ_c, thus requiring the critical point to be estimated via extrapolation. Furthermore, while hard-sphere methods treat collisions as binary interactions, entrance into the quasistatic regime coincides with the development of multibody interactions that persist even in the hard-sphere limit [28]. This conflict may render even-driven algorithms less accurate at resolving collisions upon approaching ϕ_c and perhaps result in an erroneous estimation of the value of ϕ_c. Soft-sphere DEM, on the other hand, enables us to resolve multibody contacts and simulate shear flows at any volume fraction on either side of ϕ_c, thereby allowing us to *interpolate* the value of ϕ_c. For these reasons, we expect the latter approach to provide more accurate ϕ_c estimates.

V. PRESSURE SCALINGS AND REGIME BLENDING

It has been demonstrated in experimental [10] and computational [8,9,13] studies of frictionless particles that stress data will collapse onto two curves (one above ϕ_c and one below) upon scaling the stresses and shear rate by powers of $|\phi - \phi_c|$, the distance to jamming. This idea is consistent with several models of the radial distribution function, used in kinetic theories for the inertial regime, that diverge at close packing [29–31]. Such a collapse can be achieved for frictional particles as well, as shown in Fig. 5, with

$$p^* = p/|\phi - \phi_c|^a, \quad \dot{\gamma}_p^* = \dot{\gamma}/|\phi - \phi_c|^b, \tag{4}$$

and constitutive exponents a and b. This result for frictional disks was also found independently in Ref. [16]. From the collapse it is clear that an asymptotic power-law relationship between stress and shear rate exists for each flow regime j, and we can write the form of each asymptote as

$$\frac{p_j}{|\phi - \phi_c|^a} \sim \left[\frac{\dot{\gamma}}{|\phi - \phi_c|^b}\right]^{m_j}, \tag{5}$$

where $m_{\mathrm{QS}} = 0$, $m_{\mathrm{inert}} = 2$, and $m_{\mathrm{int}} = m^*$. The exponents a and b can be fitted from the DEM data, but the values are sensitive to the choice of ϕ_c used [9] and hence should be chosen with care. Our inertial regime data suggest that $p_{\mathrm{inert}} \sim |\phi - \phi_c|^{-2}$, which is consistent with previous results

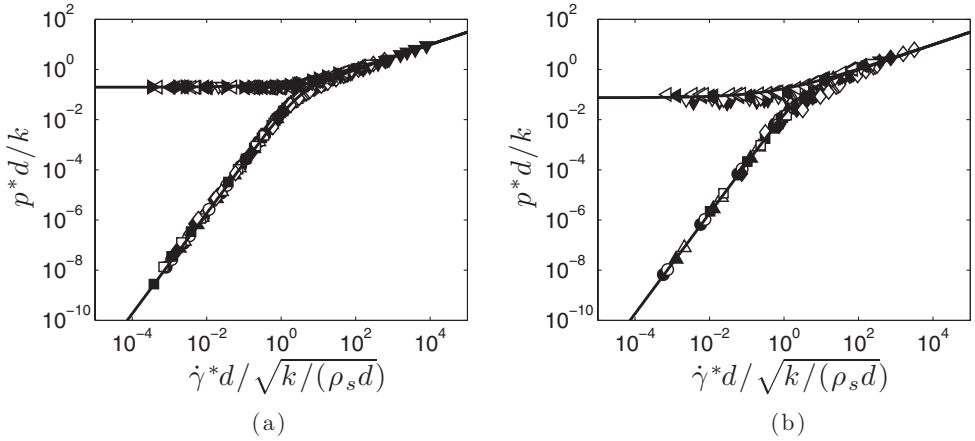

FIG. 5. Collapse of pressure vs shear rate curves from Fig. 1 for (a) $\mu = 0.5$ and (b) $\mu = 0.1$. In both cases, the pressure is scaled as $p^* = p/|\phi - \phi_c|^{2/3}$ and the shear rate as $\dot{\gamma}^* = \dot{\gamma}/|\phi - \phi_c|^{4/3}$. A simple blending function (solid lines) captures regime asymptotes and transitions.

[32]; quasistatic regime data reveal that $p_{QS} \sim |\phi - \phi_c|^{2/3}$; and, as noted earlier, $p_{int} \sim |\phi - \phi_c|^0$. These trends lead us to set $a = 2/3$, $b = 4/3$, and $m^* = 1/2$. The m^* value is consistent with our fits of the intermediate asymptote (Table I) and with experimental results [10–12], and it is similar to other values proposed for frictionless particles using the linear spring-dashpot model [8,9]. The value of a used in Ref. [24] ($a = 1$), though different, still yields a decent collapse. However, in that work, ϕ_c is determined by extrapolation from the quasistatic regime, while here we interpolate it from quasistatic and inertial regime data and furthermore verify it with stress fluctuation data, as described in Sec. IV; hence we believe our current ϕ_c values and the resulting a value to be more accurate. We also point out that the above scaling exponents depend on the contact model used [8,33]. Based on a small set of simple shear simulations with a Hertzian contact model, we observe the values of $a \approx 1$ and $m^* \approx 3/4$ to be larger than in the LSD case by a factor of 3/2, which is consistent with previous results for static, jammed systems [17]. The value of b, however, remains the same for both contact models; note that in both cases $a = bm^*$ in order to satisfy the functional forms implied by the collapse. The resulting collapse for the Hertzian particles is shown in Fig. 6.

Though the individual regime limits can be described using Eq. (5), the transitions between them have yet to be modeled. To this end, we employ a blending function B of the form

$$B(y_1, y_2) = \left(y_1^w + y_2^w\right)^{1/w}, \tag{6}$$

with $w > 0$ yielding an additive blend for the quasistatic-to-intermediate transition and $w < 0$ providing a harmonic blend for the inertial-to-intermediate transition. Figure 5 demonstrates the use of Eq. (6) with the asymptotic forms of Eq. (5) and $w = \pm 1$.

The blended model is able to capture the pressure behavior continuously in shear rate for all three regime limits as well as the transitions; moreover, it does so without defining the stresses in piecewise fashion over arbitrary shear rate domains. Notably, it also predicts the narrowing intermediate window

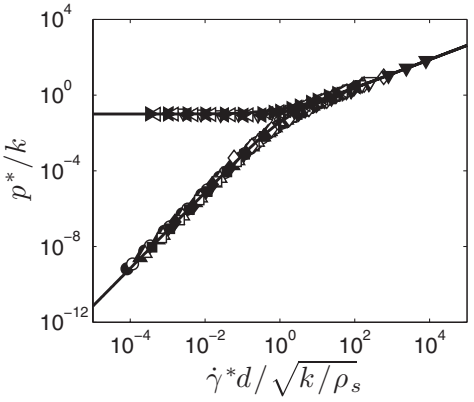

FIG. 6. Collapse of pressure vs shear rate curves for Hertzian particles with $\mu = 0.5$. The volume fractions (and legend) are the same as from Fig. 1(a). Here, $p^* = p/|\phi - \phi_c|^1$, $\dot{\gamma}^* = \dot{\gamma}/|\phi - \phi_c|^{4/3}$, and $m^* \approx 3/4$. Regime asymptotes and transitions are captured by the same blending function (solid lines) as in the Hookean case.

TABLE II. Values of model constants.

μ-Dependent parameters					
μ	0.0	0.1	0.3	0.5	1.0
η_s	0.105	0.268	0.357	0.382	0.405
α_{QS}	0.095	0.083	0.14	0.20	0.25

μ-Independent parameters							
α_{inert}	α_{int}	I_0	α_1	β_1	$\hat{\gamma}_0$	α_2	β_2
0.021	0.099	0.32	0.37	1.5	0.1	0.2	1.0

around $\phi = \phi_c$ in the limit of zero shear rate, as the quasistatic and inertial contributions to the stress become small near the jamming point. The general form of the pressure model based on the Hookean-case results can hence be written as

$$p = \begin{cases} p_{QS} + p_{int} & \text{for } \phi \geqslant \phi_c \\ \left(p_{inert}^{-1} + p_{int}^{-1}\right)^{-1} & \text{for } \phi < \phi_c, \end{cases} \tag{7}$$

with the individual regime contributions defined as

$$p_{QS} d/k = \alpha_{QS} |\phi - \phi_c|^{2/3}, \tag{8}$$

$$p_{int} d/k = \alpha_{int} \hat{\gamma}^{1/2}, \tag{9}$$

$$p_{inert} d/k = \frac{\alpha_{inert} \hat{\gamma}^2}{|\phi - \phi_c|^2}. \tag{10}$$

The pressure at $\phi = \phi_c$ can be calculated using either blend, since Eqs. (8) and (10) yield $p_{QS}(\phi = \phi_c) = 0$ and $p_{inert}(\phi = \phi_c) = \infty$, which both yield $p = p_{int}$ upon substitution into Eq. (7); this case is included with the quasistatic blending solely for the sake of simplicity. The constitutive parameter α_{QS} is a function of μ, while α_{inert} and α_{int} are fairly μ independent. These and other model constants are given in Table II.

There are a few features of Eqs. (7)–(10) that are worth noting. First, for systems above the critical volume fraction, the blending function yields a model of Herschel-Bulkley form, which has been shown previously to capture the shear stress of soft-sphere systems [10–12]. Additionally, the individual regime contributions are consistent with some known scalings. For example, the quasistatic pressure is proportional to the particle stiffness [24], while $p_{inert} = \alpha_{inert} \rho_s (\dot{\gamma} d)^2 / |\phi - \phi_c|^2$ rightly exhibits no dependence on k [1–4]. Finally, the viability of the ϕ scaling in Eq. (10) for all μ values suggests that the $\phi_c = \phi_c(\mu)$ formulation could be a simple but effective step in improving current kinetic theory models.

VI. DIMENSIONLESS GROUPS AND STRESS RATIO MODEL

It is possible to construct an analogous model for the shear stress as for the pressure, as previous works have shown τ to exhibit similar scalings with respect to the distance to jamming [8,9,14]. However, because τ and p both vary over several orders of magnitude, fitting them directly can result in poor predictions of their ratio, i.e., the shear stress ratio $\eta \equiv \tau/p$, which varies over a much narrower range. For this reason, we choose to construct a model for η and then express the shear stress as $\tau = \eta p$.

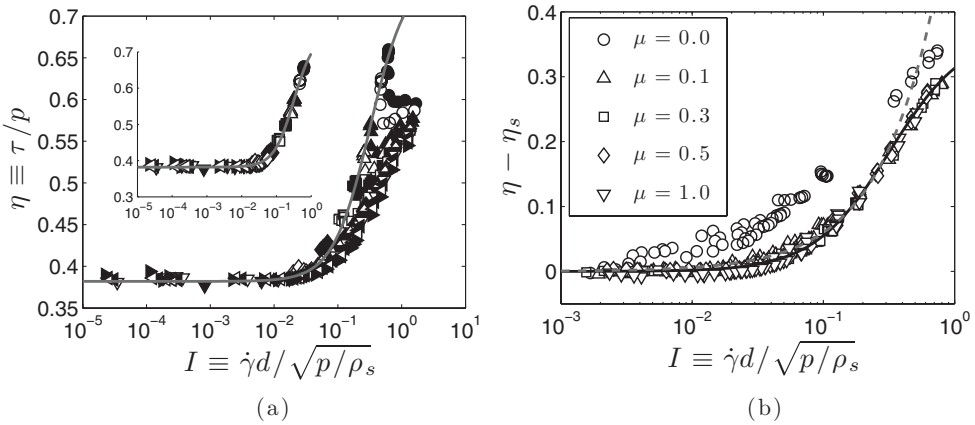

FIG. 7. Behavior of the shear stress ratio with respect to inertial number. (a) Significant scatter is observed when data from all three regimes are included. Data are shown for $\mu = 0.5$ [see legend in Fig. 1(a)]. Inset: A good collapse is achieved, however, for cases in which $\hat{\dot{\gamma}} \leqslant 3.2 \times 10^{-5}$. These cases correspond essentially to the quasistatic ($I \lesssim 10^{-2}$) and inertial regimes ($I \gtrsim 10^{-2}$) and are also indicated with a best-fit line Eq. (11) in the main figure. Intermediate regime data lie below this line. (b) The increase in the stress ratio from the yield stress ratio for these small-$\hat{\dot{\gamma}}$ cases collapses for $\mu \geqslant 0.1$. Equation (11) captures these data well (solid line), as does the model of da Cruz *et al*. [32] for $I \lesssim 0.3$ (dashed line).

Some recent, successful rheological models for dense granular flows employ a dimensionless parameter called the inertial number as the basis for achieving stress collapses over a range of volume fractions and shear rates [32,34,35]. This inertial number $I \equiv \dot{\gamma} d/\sqrt{p/\rho_s}$ is a ratio of the time scales of shear deformation and particle rearrangement, and the physics of granular flows of hard particles is said to be determined by the competition of these two mechanisms. When the particles have a finite stiffness, however, the binary collision time is nonzero and therefore presents yet another important time scale. With this point in mind, we note that the dimensionless shear rate $\hat{\dot{\gamma}}$ identified earlier is in fact the ratio of the binary collision time to the macroscopic deformation time [15], and we show here that it can be used along with the inertial number to characterize soft particle rheology.

In Fig. 7 we plot the stress ratio versus the inertial number for $\mu = 0.5$. For the densest systems, i.e., for low I, η exhibits a constant-value asymptote that we identify as the yield stress ratio $\eta_s = \eta_s(\mu)$; values of η_s for different cases of μ are presented in Table II. As I increases, η then also increases. These same observations were made in previous studies of particles in the infinitely hard limit [32,34,35]. However, unlike in these works, we also observe significant scatter as I becomes larger, which we will now show to be a consequence of the particle softness.

Because the inertial number models are designed for hard particles, we first limit our analysis to cases in which particle softness has little effect, i.e., for small $\hat{\dot{\gamma}}$. Indeed, quasistatic and inertial regime data of η versus I from our DEM simulations collapse onto a single curve, with the quasistatic regime occurring for $I \lesssim 10^{-2}$ and inertial regimes occurring for $I \gtrsim 10^{-2}$. This collapse is seen in the inset of Fig. 7(a) for $\mu = 0.5$. We model this curve as

$$\eta_{\text{hard}}(I) = \eta_s(\mu) + \frac{\alpha_1}{(I_0/I)^{\beta_1} + 1}, \tag{11}$$

where I_0, α_1, and β_1 are parameters dictating the transition from quasistatic to inertial flow. This form is similar to that of Jop *et al*. [35]. Interestingly, the increase of η from η_s is nearly identical for all cases of $\mu \geqslant 0.1$ [Fig. 7(b)]. Since the interparticle friction coefficient for most real granular materials falls in this range, we conveniently take one set of constitutive parameter values as suitable averages for our model; these values are presented in Table II.

The form of η_{hard} presented in Eq. (11) is not the only viable option. Another possibility is a simple power law, which can be written as $\eta_{\text{hard}}(I) = \eta_s + \alpha_1' I^{\beta_1'}$. This form has been used previously by da Cruz and co-workers [32] with $\beta_1' = 1$. A comparison between this form, with $\beta_1' = 1$ and $\alpha_1' = 0.6$, and the one in Eq. (11) is shown in Fig. 7(b). The two models agree closely for all values of $I \lesssim 0.3$, with a departure occurring for larger I. However, with the inertial number models, we need to be concerned only with volume fractions greater than the freezing transition $\phi_f = 0.49$ [29], where traditional kinetic theories fail [26,36]. At ϕ_f, the kinetic theory of Garzó and Dufty [1] predicts $I = 0.83$, which is consistent with our DEM results and beyond which we can ignore disparities in the η_{hard} predictions between the two models. Hence, though we continue with Eq. (11), we view both forms as being acceptable.

Though Eq. (11) captures low-$\hat{\dot{\gamma}}$ behavior well, inclusion of higher-$\hat{\dot{\gamma}}$ cases reveals a noticeable departure from the $\eta_{\text{hard}}(I)$ curve, as seen in Fig. 7. Specifically, for a given value of I, the value of η from an intermediate-regime flow is consistently lower than that given by Eq. (11). This deviation is a consequence of particle softness and, in the context of our regime blending, grows in magnitude with the intermediate-regime contribution to the pressure. Figure 8(a) shows the connection between the magnitude of this departure $\eta_{\text{soft}} \equiv \eta_{\text{hard}} - \eta$ and $\hat{\dot{\gamma}}$. This softness effect, similarly to η_{hard}, can be modeled as

$$\eta_{\text{soft}}(\hat{\dot{\gamma}}) = \frac{\alpha_2}{(\hat{\dot{\gamma}}_0/\hat{\dot{\gamma}})^{\beta_2} + 1}, \tag{12}$$

where $\hat{\dot{\gamma}}_0 = 0.1$, $\alpha_2 = 0.2$, and $\beta_2 = 1$ are constants describing the transition to intermediate flow. Finally, we can

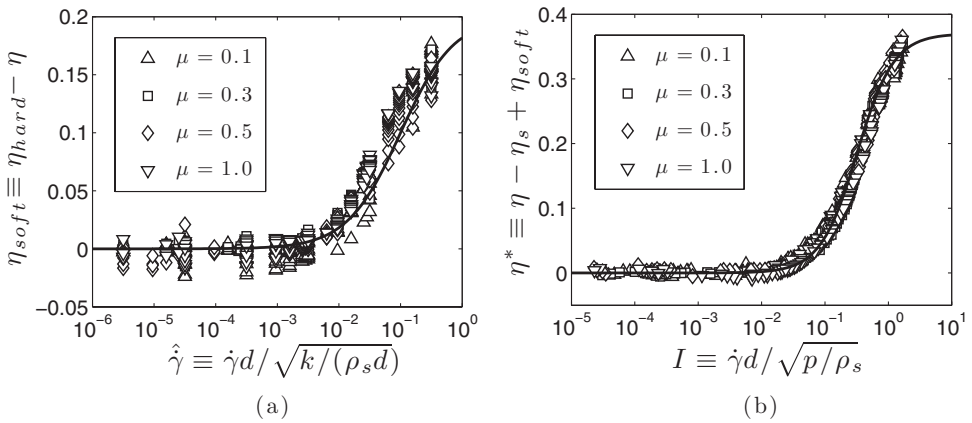

FIG. 8. Shear stress ratio contribution from $\hat{\dot{\gamma}}$ for all values of $\hat{\dot{\gamma}}$ and $\mu \geqslant 0.1$. (a) The softness-induced departure η_{soft} of the stress ratio from its hard-particle limit is essentially a function of only $\hat{\dot{\gamma}}$. (b) The correction for particle softness yields a collapse of the data in all three regimes.

write

$$\eta(I, \hat{\dot{\gamma}}) = \eta_{\text{hard}}(I) - \eta_{\text{soft}}(\hat{\dot{\gamma}}), \tag{13}$$

and, by plotting $\eta^* \equiv \eta - \eta_s + \eta_{\text{soft}}$ vs I as in Fig. 8(b), we arrive at a collapse of the stress ratio data from all three regimes.

VII. GENERALIZED CONTINUUM MODEL

Our rheological model therefore consists of Eqs. (7)–(10) for the pressure and Eqs. (11)–(13) for the shear stress ratio. Though the collapses can generally be improved by allowing the fitting parameters to be functions of μ rather than constants, the fits are nevertheless fairly good and hence justify the use of simpler forms.

While this model was developed for simple shear flows, it can be recast to handle general deformation types as done in Ref. [24]. First, we note that the strain rate tensor for simple shear flows is $\mathbf{D} = \frac{1}{2}\dot{\gamma}(\mathbf{e}_x\mathbf{e}_z + \mathbf{e}_z\mathbf{e}_x)$, where $\mathbf{e}_i$ are the unit vectors in the i direction. This expression can be rearranged to yield

$$\dot{\gamma} = 2|\mathbf{D}|, \tag{14}$$

where $|\mathbf{D}| = \sqrt{\frac{1}{2}\mathbf{D}^{\mathbf{T}} : \mathbf{D}}$ is the modulus of $\mathbf{D}$, and $\mathbf{D}$ is taken to correspond to general deformation types. Finally, we write the stress tensor as

$$\boldsymbol{\sigma} = p\,(\mathbf{I} - \eta\hat{\mathbf{S}}), \tag{15}$$

where p and η are given by our model, $\mathbf{I}$ is the identity tensor, and $\hat{\mathbf{S}} = \mathbf{S}/|\mathbf{D}|$ with $\mathbf{S} = \mathbf{D} - \frac{1}{3}\text{tr}(\mathbf{D})$. Equations (14) and (15) allow our rheological model to handle flows in more complex geometries as are commonly found in real flow scenarios.

VIII. SUMMARY

We have investigated shear flows of dense frictional granular materials in all three flow regimes in order to gain a better understanding of the scalings within each regime and the transitions between them. We find scaling relations for the pressure with respect to both shear rate and the distance to the jamming point and, for the intermediate regime, observe identical power-law behavior for particles with different friction coefficients. Furthermore, we propose a simple blending function for patching each regime's asymptotic form in order to predict pressure in between regimes. Finally, we decompose the shear stress ratio into contributions from two dimensionless shear rates, enabling us to quantify the effect of particle softness. These findings establish a framework for a global model for steady-state simple shear flows of dense granular matter.

ACKNOWLEDGMENT

We gratefully acknowledge the support of DOE/NETL Grant No. DE-FG26-07NT43070.

[1] V. Garzó and J. W. Dufty, Phys. Rev. E **59**, 5895 (1999).
[2] C. K. K. Lun, S. B. Savage, D. J. Jeffrey, and N. Chepurniy, J. Fluid Mech. **140**, 223 (1984).
[3] J. T. Jenkins and M. W. Richman, Phys. Fluids **28**, 3485 (1985).
[4] P. C. Johnson and R. Jackson, J. Fluid Mech. **176**, 67 (1987).
[5] D. G. Schaeffer, J. Differ. Equations **66**, 19 (1987).
[6] J. H. Prevost, Soil Dyn. Earthquake Eng. **4**, 9 (1985).
[7] A. J. Liu and S. R. Nagel, Nature (London) **396**, 21 (1998).
[8] T. Hatano, J. Phys. Soc. Jpn. **77**, 123002 (2008).
[9] M. Otsuki and H. Hayakawa, Phys. Rev. E **80**, 011308 (2009).
[10] K. N. Nordstrom, E. Verneuil, P. E. Arratia, A. Basu, Z. Zhang, A. G. Yodh, J. P. Gollub, and D. J. Durian, Phys. Rev. Lett. **105**, 175701 (2010).
[11] J. R. Seth, M. Cloitre, and R. T. Bonnecaze, J. Rheol. **52**, 1241 (2008).

[12] J. R. Seth, L. Mohan, C. Locatelli-Champagne, M. Cloitre, and R. T. Bonnecaze, Nat. Mater. **10**, 838 (2011).
[13] P. Olsson and S. Teitel, Phys. Rev. Lett. **99**, 178001 (2007).
[14] B. P. Tighe, E. Woldhuis, J. J. C. Remmers, W. van Saarloos, and M. van Hecke, Phys. Rev. Lett. **105**, 088303 (2010).
[15] C. S. Campbell, J. Fluid Mech. **465**, 261 (2002).
[16] M. Otsuki and H. Hayakawa, Phys. Rev. E **83**, 051301 (2011).
[17] H. P. Zhang and H. A. Makse, Phys. Rev. E **72**, 011301 (2005).
[18] C. Song, P. Wang, and H. A. Makse, Nature (London) **453**, 629 (2008).
[19] T. S. Majmudar, M. Sperl, S. Luding, and R. P. Behringer, Phys. Rev. Lett. **98**, 058001 (2007).
[20] M. van Hecke, J. Phys.: Condens. Matter **22**, 033101 (2010).
[21] P. A. Cundall and O. D. L. Strack, Geotechnique **29**, 47 (1979).
[22] S. Plimpton, J. Comput. Phys. **117**, 1 (1995).
[23] A. W. Lees and S. F. Edwards, J. Phys. C **5**, 1921 (1972).
[24] J. Sun and S. Sundaresan, J. Fluid Mech. **682**, 590 (2011).
[25] V. Kumaran, J. Fluid Mech. **632**, 109 (2009).
[26] J. Jenkins and D. Berzi, Granular Matter **12**, 151 (2010).
[27] T. Pöschel and T. Schwager, *Computational Granular Dynamics: Models and Algorithms* (Springer, Berlin, 2005).
[28] N. Mitarai and H. Nakanishi, Phys. Rev. E **67**, 021301 (2003).
[29] S. Torquato, Phys. Rev. E **51**, 3170 (1995).
[30] C. Lun and S. Savage, Acta Mech. **63**, 15 (1986).
[31] S. Ogawa, A. Umemura, and N. Oshima, Z. Angew. Math. Phys. **31**, 483 (1980).
[32] F. da Cruz, S. Emam, M. Prochnow, J.-N. Roux, and F. Chevoir, Phys. Rev. E **72**, 021309 (2005).
[33] M. Otsuki and H. Hayakawa, Prog. Theor. Phys. **121**, 647 (2009).
[34] G. MiDi, Eur. Phys. J. E **14**, 341 (2004).
[35] P. Jop, Y. Forterre, and O. Pouliquen, Nature (London) **441**, 727 (2006).
[36] Y. Forterre and O. Pouliquen, Annu. Rev. Fluid Mech. **40**, 1 (2008).

10 Appendix B

Please see the next page for the manuscript "A modified kinetic theory for frictional granular flows in dense and dilute regimes," which was published in *Physics of Fluids*.

PHYSICS OF FLUIDS **25**, 070603 (2013)

A modified kinetic theory for frictional granular flows in dense and dilute regimes

Sebastian Chialvo and Sankaran Sundaresan
Department of Chemical and Biological Engineering, Princeton University, Princeton, New Jersey 08540, USA

(Received 4 September 2012; accepted 11 February 2013; published online 18 July 2013)

Continuum modeling of granular and gas-solid flows generally involves the use of a kinetic-theory (KT) model for the particulate phase, and the most widely used KT models have been derived for dilute flows of smooth, frictionless spheres. In reality, however, granular particles are frictional and can achieve dense packing, and these features must be taken into account to improve rheological predictions in these flow scenarios. Existing approaches in the literature for producing closed-form KT-based models employ empirical modifications to adapt the original models for use in dense and frictional systems. In this article, we investigate the capacity for such modifications to improve the rheological predictions of the Garzó–Dufty (GD) KT model [V. Garzó and J. W. Dufty, "Dense fluid transport for inelastic hard spheres," Phys. Rev. E **59**, 5895–5911 (1999)]. On the basis of molecular dynamics simulations of homogeneous, simple shear flows of soft, frictional spheres, we propose a new expression for the radial distribution function at contact as well as modifications to the GD expressions for shear stress and energy dissipation rate. These changes account for dense-regime scalings observed in inertial-number models as well as the effects of interparticle friction while preserving the dynamic nature of the KT model.
 [http://dx.doi.org/10.1063/1.4812804]

I. INTRODUCTION

Granular rheology has been a commonly studied topic for many years owing in part to the diversity of behavior that granular flows exhibit. Depending on the local solids volume fraction ϕ and shear rate $\dot{\gamma}$, one can observe any of three distinct flow regimes:[1–3] (1) a quasi-static regime for ϕ exceeding the critical volume fraction ϕ_c in which pressure p and shear stress τ are independent of shear rate; (2) an inertial regime below ϕ_c in which $p, \tau \sim \dot{\gamma}^2$; and (3) an intermediate regime occurring in a narrow window of volume fractions about ϕ_c in which $p, \tau \sim \dot{\gamma}^n$ with $0.5 \lesssim n \lesssim 1$. As particle stiffness $k \to \infty$, only the inertial regime can be observed, and, because granular particles are generally extremely hard, a large subset of granular flows belong to the inertial regime.

Stresses in the inertial regime are typically modeled using the kinetic theory (KT) of granular gases,[4–7] a class of dynamic models capable of predicting a variety of clustering behaviors.[8,9] Development of these models involves following what we call the *KT approach* or *KT analysis*, which is the general process of evaluating the transport coefficients by moment analysis of the Boltzmann equation while making simplifying assumptions regarding the collision integral. These assumptions, which include the two-particle interaction model and the nature of the velocity distributions, will affect not only the regimes of validity for any resulting relations but also their attainability in closed form, as oftentimes the collision integral can only be evaluated numerically. The earliest and most widely used KT models have been derived for dilute flows of inelastic, smooth, frictionless spheres,[4–7] though there also exist more sophisticated models that account for particle roughness by including tangential restitution and rotational degrees of freedom.[10,11] We refer collectively to these two types of models, which consist of closed-form constitutive expressions, as *traditional* KT models.

Though all flows in the inertial regime are amenable to KT analysis, this regime in itself contains two ranges of volume fractions exhibiting somewhat different behavior. The first is the *dilute inertial* regime and encompasses volume fractions between zero and $\phi_f \approx 0.49$. In this range, traditional KT models exhibit generally good agreement with discrete particle simulations. On the other hand, for volume fractions between ϕ_f and ϕ_c, which constitute the *dense inertial* regime, KT models are less successful, with discrepancies resulting from a few assumptions made in their derivation. For example, one typically assumes "molecular chaos," i.e., that the collisions of a particle with its neighbors are uncorrelated, allowing one to express the two-particle velocity distribution function as the product of the single-particle distribution functions (which are Gaussian). In dense flows, though, a particle will interact many times with the same neighbors[12,13] as steric effects become predominant, thereby resulting in a non-Gaussian distribution of normal relative velocities.[14] Additionally, these models assume a small Péclet number $Pe \equiv \dot{\gamma} d/\sqrt{T}$, which represents the extent of departure from the equilibrium, isotropic state of an assembly of particles of diameter d and with a granular temperature T. If $Pe \ll 1$, thermal forces predominate and preserve a nearly isotropic structure within the assembly. However, shear flows are distinctly nonequilibrium, as demonstrated by the emergence of prominent structural features including force chains[15] and anisotropy of the fabric of contacts,[16–18] which would not survive in a thermal system. This phenomenon arises in part because collisions between granular particles are dissipative, characterized by a restitution coefficient e often not near unity that serves to increase Pe by decreasing T. It is hence understandable that traditional KT models are unable to predict some features of the dense inertial regime, including the increase in T near the critical volume fraction[19] and the saturation of the shear stress ratio $\eta \equiv \tau/p$ to its correct close-packing limit[20] η_s. Recent inertial-number models do predict the yield stress[1,21,22] but do not apply to dilute flows; they also do not account for important nonlocal effects[23] that KT can capture via conduction of pseudothermal energy. There is a need, therefore, for a rheological model that bridges the dense and dilute behaviors within the KT framework.

In addition to their dense-regime limitations, traditional KT models are derived assuming collisions of *frictionless* particles only and hence are unequipped to handle any dependence on the interparticle friction coefficient μ. In reality, however, granular materials are frictional, and the value of μ has been shown to have a significant effect on stresses at least in the quasistatic regime,[18] where increasing μ generally increases the stress because of larger tangential interparticle forces arising from enduring contacts. Attempts to quantify the friction effect in the inertial regime, though, have been somewhat more limited. Many KT works have considered tangential restitution,[10,11,14,24,25] which similarly describes roughness but is nevertheless microscopically different from friction. A KT model that explicitly and accurately accounts for dependence on μ is currently lacking.

One important quantity in which friction, shearing, and large packing density all play an important role is the radial distribution function at contact $g_0(\phi)$. Most expressions for g_0, in agreement with g_0 data extrapolated directly from equilibrium hard-sphere simulations,[26] predict its divergence at close packing,[26–28] i.e., $g_0 \sim (\phi_c - \phi)^m$ for some constant $m < 0$. However, shear simulations of discrete-particle assemblies suggest that these expressions significantly underpredict g_0 for systems far from equilibrium and featuring strong contact anisotropy.[19,29] Additionally, these expressions tend to neglect the dependence of the critical volume fraction on the friction coefficient, which has been observed both in static systems[30] and sheared systems.[1] Since $\phi_c(\mu)$ determines the point at which the pressure diverges, any extension of KT to the dense regime must take this dependence into account.

Given the need for a KT model that spans dense and dilute regimes while accounting for anisotropy and interparticle friction, it is natural to attempt to revisit the KT approach without making the aforementioned inappropriate assumptions. Doing so would, in theory, yield a model applicable to a wide array of flows and particle types without the need for empirical fitting of rheological data. However, two major problems arise in this endeavor. First, at the present time it does not appear possible to deduce *closed-form* expressions for the transport coefficients in the dense regime when employing the non-Gaussian relative velocity distribution function.[14] Because the rheological behavior of the material would need to be evaluated numerically for every given set of particle parameters, it is impractical to implement such a model into a continuum-model solver for application to large-scale flow problems. Second, this approach still does not avoid the need for

empiricism, as the dense-regime relative velocity distribution function[14] and the radial distribution function at contact cannot yet be predicted *a priori*. Hence, it appears that the most promising path toward a comprehensive rheological model in the near term lies in empirical modification of existing closed-form KT models.

Indeed, such KT modifications have been proposed numerous times in the recent literature.[31–34] Of particular interest are the changes proposed by Jenkins and co-workers[31,33] for extending the commonly used theory of Garzó and Dufty[4] (GD), which is originally derived for flows of frictionless, moderately dissipative spheres in the dilute regime. The first modification calls for introduction of a length scale L, which the authors call a "chain length," into the expression for the energy dissipation rate.[31] This length scale is said to represent the typical length of force chains that form in dense granular flows and that grow large upon approaching ϕ_c. While the existence of a large or diverging length scale in such flows is a topic of debate,[2,25,35,36] the use of such a functional form is nevertheless successful in qualitatively describing the dense-regime increase in temperature and decrease in shear stress ratio. The second modification is the replacement of the normal restitution coefficient with an "effective" restitution coefficient $e_{\text{eff}}(\mu, e) < e$ that accounts for the increased dissipation resulting from interparticle friction.[33] This substitution has been shown to improve stress predictions for dilute flows of slightly frictional particles. Modifications such as these are not only successful in improving the predictions of traditional KT models but moreover are convenient to constitute based on stress and temperature data from granular flow experiments and simulations.

In the present work, we assess the capacity for these two modifications to yield accurate model expressions by comparing their steady-state predictions for pressure, shear stress, and temperature with data obtained from discrete element method[37] (DEM) simulations of sheared particle assemblies; and, when these approaches prove insufficient, we propose additional corrections to bring the GD model predictions into closer agreement with those of the DEM simulations.

In Secs. II–IV, we present the original (GD) KT model, an explanation of our simulation methodology, and a validation of our simulations for the case of *frictionless* particles *below* ϕ_f. We then demonstrate the stark disagreement between the GD model predictions and our DEM results *above* ϕ_f and for *frictional* particles at all volume fractions. Finally, we outline the steps taken to constitute various model quantities used in our modified KT expressions based on our DEM results.

II. GARZÓ–DUFTY KT MODEL

As aforementioned, the kinetic theory of choice for the modifications will be that of Garzó and Dufty,[4] which is designed for smooth, frictionless, moderately inelastic particles in the dilute regime. According to this model, for simple shear flows one can write the pressure p as

$$p = \rho_s H(\phi, e) T, \tag{1}$$

the shear stress τ as

$$\tau = \rho_s d\dot{\gamma} J(\phi, e)\sqrt{T}, \tag{2}$$

and the energy dissipation rate Γ as

$$\Gamma = \frac{\rho_s}{d} K(\phi, e) T^{3/2}. \tag{3}$$

Here, ρ_s is the solid material density, and the definitions of the dimensionless expressions H, J, and K and their components are

$$H(\phi, e) = \phi[1 + 2(1 + e)\phi g_0], \tag{4}$$

$$J(\phi, e) = \frac{5\sqrt{\pi}}{96}\eta^*, \tag{5}$$

$$K(\phi, e) = \frac{12}{\sqrt{\pi}}\phi^2 g_0(1 - e^2), \tag{6}$$

$$\eta^* = \eta_k^* + \eta_c^* + \eta_b^*, \tag{7}$$

$$\eta_k^* = \frac{1 - \frac{2}{5}(1+e)(1-3e)\phi g_0}{[1 - \frac{1}{4}(1-e)^2 - \frac{5}{24}(1-e^2)]g_0}, \tag{8}$$

$$\eta_c^* = \frac{4}{5}(1+e)\phi g_0 \eta_k^*, \tag{9}$$

and

$$\eta_b^* = \frac{384}{25\pi}(1+e)\phi^2 g_0. \tag{10}$$

The quantities η_k^*, η_c^*, and η_b^* are the scaled kinetic, collisional, and bulk viscosity contributions, respectively. As per Jenkins and Berzi,[31] we have neglected here the very small contribution of all terms proportional to a quantity that Garzó and Dufty[4] denote as $c^*(e)$. The radial distribution function at contact $g_0(\phi)$ has been modeled in numerous ways,[26–28,32,38] but two formulations in particular have been validated by simulation data of frictionless hard spheres at equilibrium. The first of these is the Carnahan–Starling expression,[38]

$$g_0^{\mathrm{CS}} = \frac{1 - \phi/2}{(1-\phi)^3}, \tag{11}$$

which is valid for systems below ϕ_f. The second is a modification to g_0^{CS} proposed by Torquato[26] for denser systems. Written as

$$g_0^{\mathrm{Torquato}} = \begin{cases} g_0^{\mathrm{CS}}(\phi) & \text{for } \phi \le \phi_f \\ g_0^{\mathrm{CS}}(\phi_f)\frac{\phi_c - \phi_f}{\phi_c - \phi} & \text{for } \phi > \phi_f \end{cases}, \tag{12}$$

it differs from the Carnahan–Starling result only above ϕ_f, specifically by diverging at ϕ_c. Because of its agreement with simulation data and its use in a recent KT work,[31] we will initially use Torquato's[26] g_0 formulation in Sec. IV together with the GD equations for comparison with DEM results.

For steady-state simple shear flows, we can write the granular energy balance as

$$\Gamma - J_{\mathrm{vis}} = 0, \tag{13}$$

where

$$J_{\mathrm{vis}} = \dot{\gamma}\tau \tag{14}$$

is the viscous energy production rate. With this condition and Eqs. (2) and (3), we can solve for the GD steady-state temperature expression

$$T_{\mathrm{SS}}^{\mathrm{GD}} = \left(\frac{J}{K}\right)(\dot{\gamma}d)^2. \tag{15}$$

This result then allows us to obtain the steady-state GD pressure

$$p_{\mathrm{SS}}^{\mathrm{GD}} = \left(\frac{JH}{K}\right)\rho_s(\dot{\gamma}d)^2 \tag{16}$$

and shear stress

$$\tau_{\mathrm{SS}}^{\mathrm{GD}} = \sqrt{\frac{J^3}{K}}\rho_s(\dot{\gamma}d)^2. \tag{17}$$

Finally, the shear stress ratio η is found from Eqs. (1) and (2) to be

$$\eta_{\mathrm{SS}}^{\mathrm{GD}} = \frac{\sqrt{JK}}{H}. \tag{18}$$

We emphasize that these four expressions are valid *only for simple shear flows that have reached steady state*.

III. SIMULATION METHODS

We use a package of the discrete element method[37] found in the molecular dynamics package LAMMPS[39] in order to simulate simple shear flows of discrete, uniform, spherical particles. These particles interact via a linear spring-dashpot (LSD) model, which gives the normal and tangential forces on a particle i caused by contact with a particle j as

$$\mathbf{F}_{ij}^{n} = k_n \delta_{ij} \mathbf{n}_{ij} - \gamma_n m_{\text{eff}} \mathbf{v}_{ij}^{n}, \tag{19}$$

$$\mathbf{F}_{ij}^{t} = -k_t \mathbf{u}_{ij}^{t} - \gamma_t m_{\text{eff}} \mathbf{v}_{ij}^{t}, \tag{20}$$

for overlap distance δ_{ij}, particle diameter d, spring stiffness constants k_n and k_t, viscous damping constants γ_n and γ_t, effective mass $m_{\text{eff}} = m_i m_j/(m_i + m_j)$ for particle masses m_i and m_j, relative particle velocity components $\mathbf{v}_{ij}^{n}$ and $\mathbf{v}_{ij}^{t}$, and elastic shear displacement $\mathbf{u}_{ij}^{t}$. We choose to set $k_t/k_n = 2/7$ and $\gamma_t = 0$ as done in some previous works[1,40] and by doing so can set γ_n in order to produce the desired restitution coefficient according to the expression $e = \exp\left(-\gamma_n \pi/\sqrt{4k_n/m_{\text{eff}} - \gamma_n^2}\right)$. While experiments have revealed a dependence of the restitution coefficient on the particle impact velocity,[41] a behavior captured by some nonlinear spring-dashpot models,[42] kinetic theory models assume a constant e as produced by the LSD model. Hence, for ease of comparison we neglect more complex, nonlinear behavior.

Samples are prepared by placing 2000 particles on a simple cubic lattice in a periodic box, assigning random, normally distributed initial velocities to the particles, and allowing the assembly to evolve in order to lose any memory of the initial configuration. The assembly then undergoes a simple shear deformation with shear rate $\dot{\gamma}$ imposed via the Lees-Edwards boundary condition,[43] which allows for the system to remain homogeneous during the shearing process. The shearing motion proceeds until the system reaches a steady state and remains there for sufficient time to collect proper statistics as determined by the saturation of the time-averaged stresses. From the particle interaction forces and the constant box volume V, we can calculate the macroscopic stress tensor as

$$\boldsymbol{\sigma} = \frac{1}{V} \sum_i \left[\sum_{j \neq i} \frac{1}{2} \mathbf{r}_{ij} \mathbf{F}_{ij} + m_i (\mathbf{v}_i')(\mathbf{v}_i') \right], \tag{21}$$

where $\mathbf{r}_{ij}$ is the contact vector from the center of particle j to the center of particle i, and $\mathbf{v}_i'$ is the particle fluctuating velocity (i.e., its velocity relative to its mean streaming velocity). From this tensor, we can calculate the ensemble-averaged pressure $p = (\sigma_{xx} + \sigma_{yy} + \sigma_{zz})/3$ and shear stress $\tau = \sigma_{xz}$. Because we limit the focus of our study to inertial regime flows, i.e., flows with $\phi < \phi_c$ and $\hat{\dot{\gamma}} \equiv \dot{\gamma} d/\sqrt{k/\rho_s d} \lesssim 10^{-3}$ [Ref. 1], it is appropriate to scale our stress data by the quantity $\rho_s (\dot{\gamma} d)^2$, where ρ_s is the solid material density and d is the particle diameter; similarly, we scale the temperature data by $(\dot{\gamma} d)^2$. We also have confirmed this Bagnold scaling by running a small set of simulations with varying values of k and observing no substantial changes in the predicted temperature or stresses.

IV. RESULTS

A. Comparison of KT with DEM of frictionless particles

If the kinetic theory is to be extended to frictional and dense flows based on DEM data, we must demonstrate first that the continuum and discrete models make similar stress and temperature predictions for *frictionless* particle flows at *low-to-moderate* volume fractions. Such a comparison is shown in Fig. 1, with scaled pressure, shear stress ratio, and scaled temperature plotted versus volume fraction.

Indeed, as expected, the predictions of the two models display good agreement up to $\phi \approx \phi_f$. For higher volume fractions, however, there appear three salient discrepancies: (1) the scaling of p with respect to ϕ, (2) the close-packed limit of the shear stress ratio, and (3) the scaling of T with respect

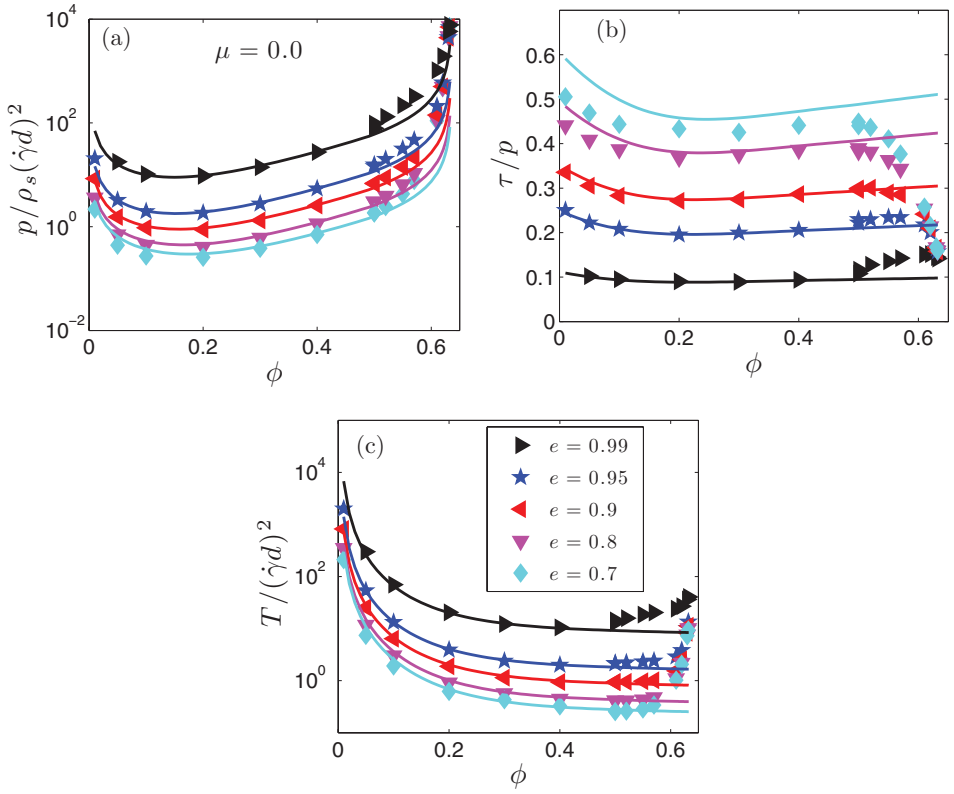

FIG. 1. Results from DEM simulations of steady state simple shear flows of *frictionless* particles. (a) Scaled pressure, (b) shear stress ratio, and (c) scaled temperature are plotted versus volume fraction for various cases of the restitution coefficient e. The predictions of GD kinetic theory with Torquato's[26] radial distribution function and $\phi_c = 0.636$ are shown with solid lines. GD and DEM are in good agreement for volume fractions of $\phi \lesssim \phi_f = 0.49$ but depart above this point.

to ϕ. Of course, the original kinetic theory cannot be expected, as explained earlier, to capture dense flow behavior. However, the good agreement at the low volume fractions for which the original GD model was designed validates our use of DEM for model construction.

B. Comparison of KT with DEM of frictional particles

When the particles are made frictional, on the other hand, the DEM data depart markedly from the GD predictions, as seen in Fig. 2 for $\mu = 0.5$. In addition to its aforementioned dense-regime shortcomings, the GD model now substantially overpredicts the pressure and temperature for $\phi \lesssim \phi_f$ while also underpredicting the shear stress ratio. This behavior is unsurprising, as the GD model is not designed for such systems, and is explained by the additional source of dissipation of pseudothermal energy provided by interparticle friction during collisions between particles.[33] Additionally, the assumption that the critical volume fraction ϕ_c is independent of μ leads the model to predict incorrectly the location of the dense-limit pressure divergence. As expected based on its derivation, the GD model is unequipped to handle either friction or dense packing, and adaptations must be made to extend its applicability to these conditions.

Based on the discrepancies observed between the GD and DEM predictions and on previous approaches to constitutive model refinement, our strategy for modifying the kinetic theory equations will be as follows:

1. The energy dissipation Γ (Eq. (3)) will be modified to include (1) an effective restitution coefficient[33] $e_{\text{eff}} = e_{\text{eff}}(e, \mu)$ in the K term to capture μ-functionality and (2) a multiplicative

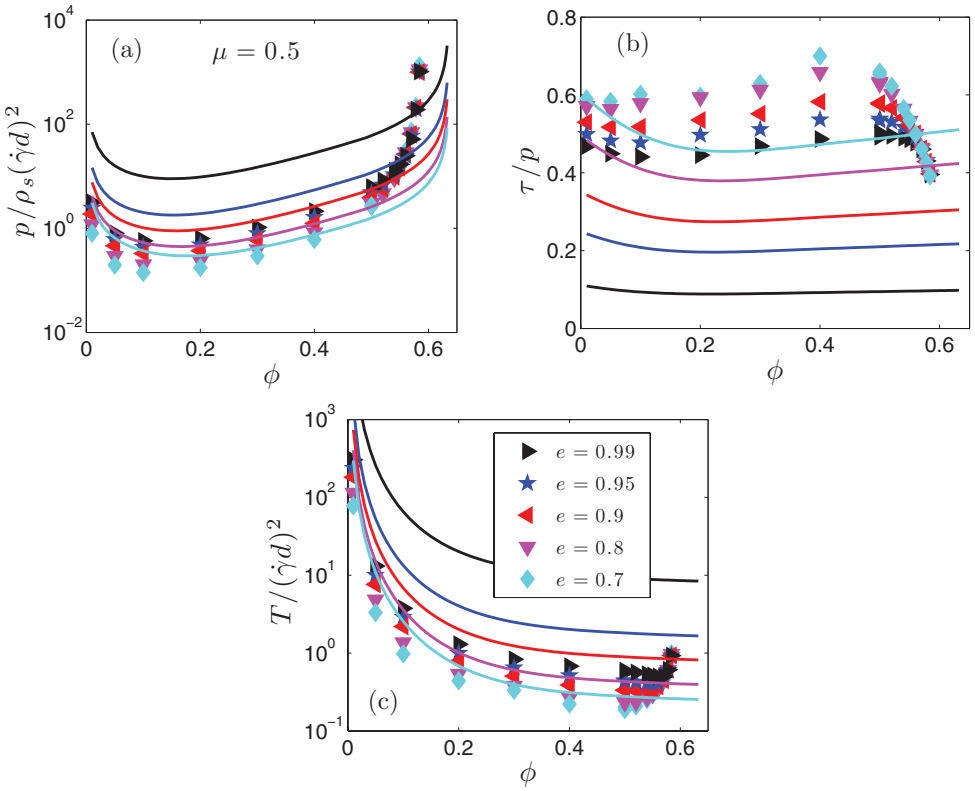

FIG. 2. Results from DEM simulations of steady state simple shear flows of *frictional* particles with $\mu = 0.5$. (a) Scaled pressure, (b) shear stress ratio, and (c) scaled temperature are plotted versus volume fraction for various cases of the restitution coefficient e. The predictions of GD kinetic theory with Torquato's[26] radial distribution function and $\phi_c = 0.636$ are shown with solid lines. GD and DEM are in very poor agreement, even for the dilute regime.

correction factor δ_Γ related to the chain length[31] to capture dense-regime trends with respect to ϕ.

2. A new expression will be proposed for the radial distribution function at contact g_0 that will diverge at close packing in a manner concordant with our DEM data and that is specifically for use in nonequilibrium systems.
3. The shear stress τ will be decomposed into a yield stress and an inertial stress, the latter of which will be similar to Eq. (2) except augmented with a multiplicative correction factor δ_τ (analogous to the adjustable parameter that appears in the τ expression of some previous kinetic theories[7,8,44]). This factor will transition from a dilute-regime limit of δ_τ^{dil} that accounts for μ-functionality at low ϕ to a dense-regime limit $\delta_\tau^{\text{dense}}$ that will force η to obey an inertial-number model[1,20–22] for $\phi \gtrsim \phi_f$.

The correction factors will be applied to the *dynamic* GD equations and, as a result, will change the *steady-shear* GD predictions produced by imposing Eq. (13). The expressions chosen for these corrections, therefore, will be motivated by the steady-state values of the temperature, pressure, and shear stress calculated from our simple shear simulations.

C. Constituting the DEM results

1. DEM temperature

We will focus first on corrections to capture the DEM temperature. Because the behavior of the temperature is qualitatively different in the dense and dilute regimes, we will analyze each case separately. In the dilute regime, temperature is observed to drop upon increasing the friction

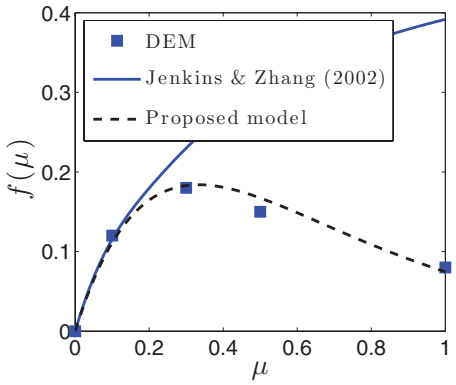

FIG. 3. The dependence of the frictional part $f(\mu)$ (Eq. (23)) of the effective restitution coefficient e_{eff} on the interparticle friction coefficient μ. Our expression agrees with that of Jenkins and Zhang[33] for small values of μ.

coefficient from zero, and following the approach of Jenkins and Zhang[33] we seek to define an *effective* restitution coefficient that describes the total energy loss due to inelasticity and friction during an interparticle collision. To do so, we rewrite Eq. (15) by replacing e in the K term of the denominator with $e_{\text{eff}} = e_{\text{eff}}(e, \mu)$. The value of the effective restitution coefficient is then chosen to reproduce the temperature found in dilute-regime DEM simulations. Based on the DEM data, we find the expression

$$e_{\text{eff}} = e - f(\mu) \tag{22}$$

with

$$f(\mu) = \frac{3}{2}\mu \exp(-3\mu) \tag{23}$$

to provide a good fit. A comparison is made in Fig. 3 between this form and that derived by Jenkins and Zhang[33] for small values of μ. (We note that their expression for f has a very small dependence on e, which we have neglected.) For $\mu \lesssim 0.2$, the two expressions show good agreement but begin to depart thereafter. In particular, following our data, our expression for $f(\mu)$ decreases for larger values of the friction coefficient, seeming to predict lower dissipation for more frictional particles. This nonmonotonic dependence is consistent with the previous finding that the translational temperature reaches the same steady-state values for the zero- and infinite-friction cases.[34] We thus can write

$$T_{\text{DEM}}^{\text{dil}} = \left(\frac{J}{K'}\right)(\dot{\gamma}d)^2 \tag{24}$$

with

$$K'(\phi, e, \mu) = \frac{12}{\sqrt{\pi}}\phi^2 g_0(1 - e_{\text{eff}}^2) \tag{25}$$

$$= K(\phi, e)\left(\frac{1 - e_{\text{eff}}^2}{1 - e^2}\right). \tag{26}$$

For volume fractions above $\phi \approx \phi_f$, an additional correction is needed to capture the increase in temperature with ϕ [Ref. 19], as the original GD model predicts a monotonically decreasing temperature. Plotting the dimensionless temperature versus the distance to the critical volume fraction $\phi_c - \phi$, as in Fig. 4, we observe that

$$T_{\text{DEM}}^{\text{dense}} = \frac{\alpha_1(\dot{\gamma}d)^2}{(\phi_c - \phi)^{1/2}}, \tag{27}$$

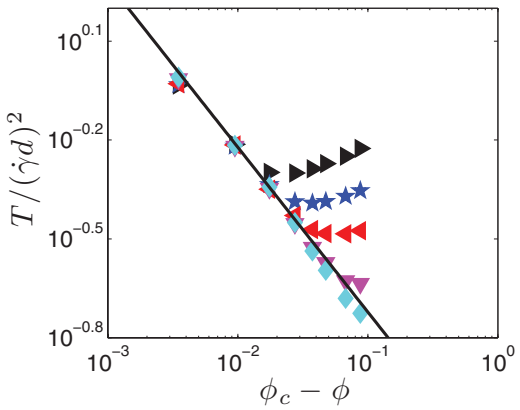

FIG. 4. Dense-regime temperature from DEM simulations. Symbols are the same as in Figs. 1 and 2. Scaled temperature versus volume fraction is shown for $\mu = 0.5$. A power law of slope $-1/2$ is observed (solid line) close to ϕ_c, and the transition from dilute to dense behavior occurs for lower ϕ as e decreases. The power-law fit is reasonably good for all cases of μ.

a power law that is robust to changes in e and μ. The transition in temperature between the dilute and dense regimes can be captured conveniently by

$$T_{\mathrm{DEM}} = \max(T^{\mathrm{dil}}_{\mathrm{DEM}}, T^{\mathrm{dense}}_{\mathrm{DEM}}) \tag{28}$$

or equivalently

$$T_{\mathrm{DEM}} = M(\phi, e, \mu)(\dot{\gamma}d)^2 \tag{29}$$

with

$$M(\phi, e, \mu) = \max\left(\frac{J}{K'}, \frac{\alpha_1}{[\phi_c - \phi]^{1/2}}\right). \tag{30}$$

This form succeeds in capturing the sharp transition between the two behaviors as well as the loss of e-dependence observed in the close-packing limit, as seen in the comparison of Eq. (29) with the DEM temperature in Fig. 5. Moreover, it succeeds in reproducing the e-dependence of the volume fraction at which the dilute-to-dense crossover occurs without needing to specify this point explicitly. There is some minor quantitative disagreement in very dilute cases ($\phi \lesssim 0.2$), but we will neglect them here and reserve this topic for Sec. V.

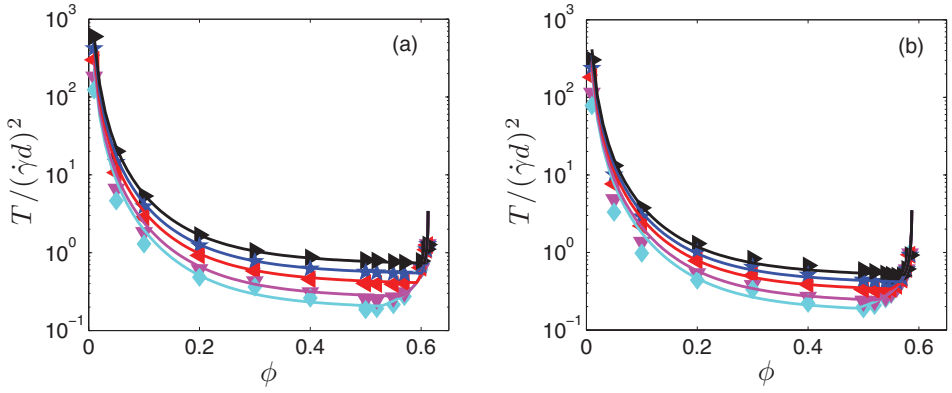

FIG. 5. Comparison of the new steady-state temperature model with DEM results. Scaled temperature versus volume fraction is shown for (a) $\mu = 0.1$ and (b) $\mu = 0.5$. The agreement observed here between the KT and DEM predictions is substantially better than in Fig. 2. Symbols are the same as in Figs. 1 and 2.

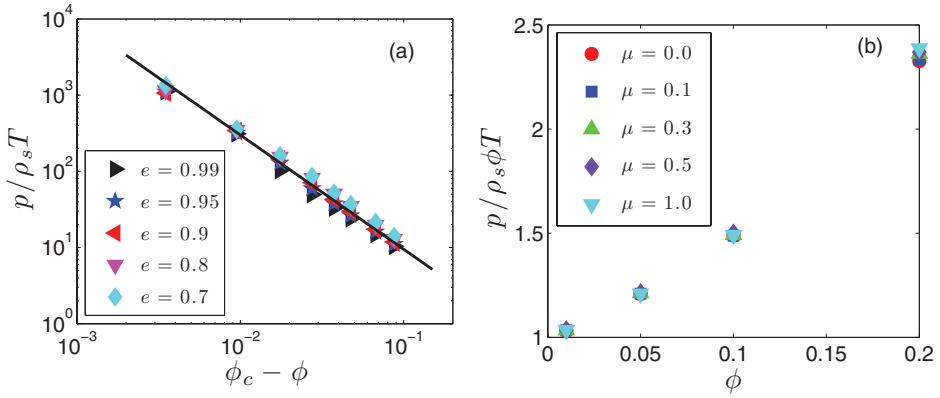

FIG. 6. Behavior of the quantity $p/\rho_s \phi T$ from DEM simulations in (a) the dense regime with $\mu = 0.5$ and (b) the dilute regime with $e = 0.9$. (a) The clear power-law dependence with slope $-3/2$ (solid line) suggests that $g_0 \sim (\phi_c - \phi)^{-3/2}$ in the dense regime, in disagreement with Torquato's[26] equilibrium results. (b) Varying the friction coefficient μ has no effect on this quantity in the dilute regime, indicating that e need not be replaced with e_{eff} in the pressure equation (Eq. (1)). Similar results are obtained for other cases of μ and e.

2. DEM pressure

With the temperature now described accurately, we turn our attention to the pressure, which depends primarily on T and the contact value $g_0(\phi)$ of the radial distribution function. As demonstrated in Fig. 2(a), the scaling of the pressure with respect to volume fraction in the dense regime observed using DEM is in disagreement with the GD model when Torquato's[26] g_0 expression for frictionless spheres at equilibrium is used. Moreover, substitution of the temperature given by Eq. (29) into Eq. (1) is insufficient to resolve the disparity. In fact, based on literature results[1,21] showing that $p \sim (\phi_c - \phi)^{-2}$ and our finding here that $T \sim (\phi_c - \phi)^{-1/2}$ in the dense regime, we would expect to see $g_0 \sim (\phi_c - \phi)^{-3/2}$. By plotting DEM results for $p/\rho_s \phi T$, which goes as g_0 in the dense regime, versus $\phi_c - \phi$ as in Fig. 6(a), we indeed observe this power law quite clearly. The $-3/2$ power also lies in the range of exponent values measured for the collision frequency (which is proportional to g_0) in sheared hard-sphere systems.[25] Hence, we propose to represent g_0 as

$$g_0 = g_0^{\text{CS}} + \frac{\alpha_2 \phi^2}{[\phi_c(\mu) - \phi]^{3/2}} \tag{31}$$

with $\alpha_2 = 0.58$ for all e and μ. Note that we allow ϕ_c to vary with μ as per Chialvo *et al.*[1] A comparison of this form with those of Torquato[26] and Carnahan–Starling[38] is given in Fig. 7. The larger exponent in our proposed model for sheared systems ($-3/2$) compared with that of Torquato's[26] model for equilibrium systems (-1) results in a stronger divergence at close packing. This phenomenon can be explained physically by recalling that sheared systems exhibit strong orientational anisotropy of collisions. In a sheared assembly, a reference particle will experience collisions concentrated preferentially along the compression axis of shear, while in isotropic systems these collisions are distributed uniformly in all directions. This crowding of collisions into a smaller spatial window in the sheared case results in a higher effective contact value of the radial distribution function for a given packing fraction.

Using the proposed g_0 model along with our DEM temperature in the GD pressure equation, we are able to improve the kinetic-theory predictions of the pressure for the entire range of ϕ and for all e and μ investigated (Fig. 8). As mentioned above for the temperature, there is some disagreement for $\phi \lesssim 0.2$, though the μ-independence of $p/\rho_s \phi T$ indicates that improved prediction of T in this range would mitigate or eliminate this error.

Because the collisional contribution to the pressure contains a factor of $(1 + e)$, one could ask whether the effective restitution coefficient should appear here as well. To address this question, we examine the behavior of $p/\rho_s \phi T$ from dilute-regime DEM simulations as the friction coefficient is varied. According to the GD model $p/\rho_s \phi T = 1 + 2(1 + e)\phi g_0$, so replacement of e here with e_{eff} is

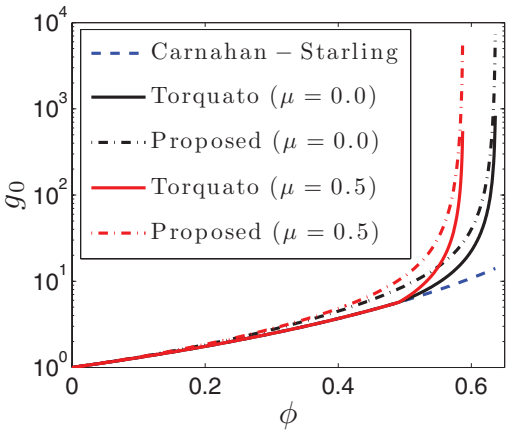

FIG. 7. Comparison of the g_0 expression proposed in Eq. (31) with those of Torquato[26] (Eq. (12)) and Carnahan–Starling[38] (Eq. (11)). The proposed and Torquato expressions are plotted for both $\mu = 0.0$ and $\mu = 0.5$, with ϕ_c depending on μ. Both of these models approach the Carnahan–Starling model in the dilute regime, while their dense-regime behaviors differ in their scaling with respect to $(\phi_c - \phi)$.

justified only if a μ-dependence is observed. As seen in Fig. 6(b), no such dependence is observed in the simulations, and hence we maintain the original form.

3. DEM shear stress ratio

Finally, we must attempt to capture the DEM shear stress, which, since we have now described the pressure, can be achieved by simply modeling the shear stress ratio η. Before investigating any further corrections, however, we first test whether the modifications done so far are sufficient to capture the DEM trends. In Fig. 9, we compare the DEM η values with the predictions of the original GD model (Eqs. (1) and (2)) augmented only with e_{eff} from Eq. (22), a chain length correction that reproduces the temperature as per Eq. (30), and the new g_0 expression from Eq. (31). This set of corrections would involve setting $\delta_\tau = 1$ and is analogous to the model of Jenkins and Berzi.[31] As seen in the figure, there is somewhat of an improvement in that this modified GD model now predicts an increase in η due to friction in the dilute regime and a decrease in η as ϕ approaches ϕ_c. However, this model continues to underpredict the effects of friction and still fails to produce a yield stress ratio at close packing. Hence, a further shear stress correction is necessary to reproduce the DEM η results quantitatively.

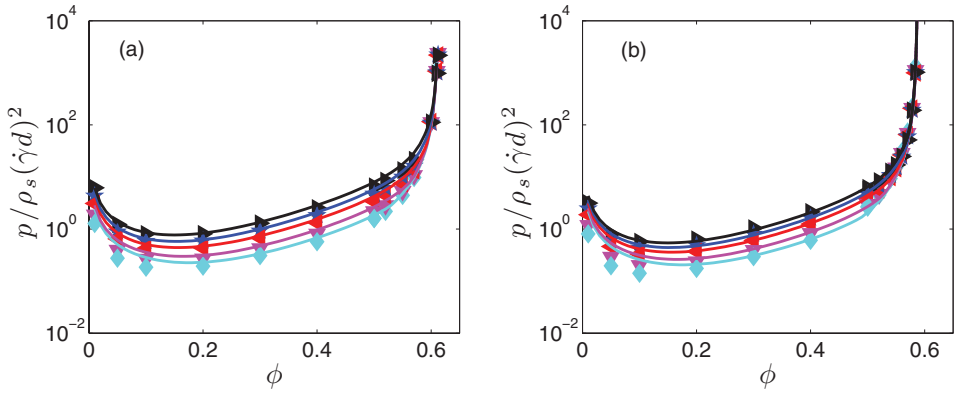

FIG. 8. Comparison of the new steady-state pressure model with DEM results. Scaled pressure versus volume fraction is shown for (a) $\mu = 0.1$ and (b) $\mu = 0.5$. The agreement observed here between the KT and DEM predictions is substantially better than in Fig. 2. Symbols are the same as in Figs. 1 and 2.

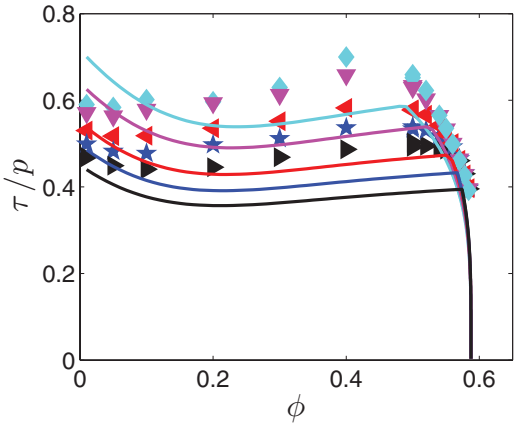

FIG. 9. Comparison of the DEM shear stress ratio values with the GD model modified to include only e_{eff} and the new g_0 expression (i.e., $\delta_\tau = 1$ as per Jenkins and Berzi[31]). The agreement observed here between the modified GD and DEM predictions is somewhat better than in Fig. 2, though the effect of friction is underestimated and a finite yield stress ratio is still not predicted. Results are shown for $\mu = 0.5$, though these trends are observed for all μ. Symbols are the same as in Figs. 1 and 2.

The proposed η model must not only predict the dilute- and dense-regime behaviors in the respective limits of $\phi \to 0$ and $\phi \to \phi_c$ but must also capture the transition between the two. In the case of pressure and temperature, the dilute-to-dense transitions involve changes of orders of magnitude, facilitating the bridging effort by allowing simple additive or switch models. However, the shear stress ratio varies over a much smaller range – always within the same order of magnitude – and the subtler transition will require a different bridging form.

In the dilute regime, we define $\psi(\mu, e, \phi) \equiv \eta(\mu, e, \phi)/\eta(\mu = 0, e, \phi)$ in order to quantify the departure of the shear stress ratio from the frictionless case. We then estimate a ϕ-averaged value of ψ for each case of μ and e, with weighting given more heavily to volume fractions between approximately between 0.2 and 0.4. The expression

$$\psi(\mu, e) = 1 + \frac{3}{10}(1 - e^2)^{-2/3}[1 - \exp(-8\mu)] \tag{32}$$

is found to provide a reasonably good fit while also satisfying some physical criteria, including the diminished influence of friction for more inelastic particles and the requirement that $\psi \to 1$ as $\mu \to 0$. The exponential μ-dependence here is similar in form to that proposed for constitutive coefficients in a recent quasi-static model;[18] it also agrees with our observations that the effect of μ on η is monotonic, unlike for T, and saturates quickly as μ exceeds about 0.3. The dilute shear stress ratio is then written as

$$\eta_{\text{DEM}}^{\text{dilute}} = \eta_{\text{SS}}^{\text{GD}}\psi. \tag{33}$$

In the dense regime, existing models for the shear stress ratio tend to take the form $\eta = \eta(I)$, where

$$I \equiv \frac{\dot{\gamma} d}{\sqrt{p/\rho_s}} \tag{34}$$

is the inertial number and can be interpreted as a ratio of the time scales of macroscopic shear deformation to microscopic particle rearrangement. Though this quantity has been shown to dictate granular rheology in the dense regime,[1,20–22] it is not particularly useful in characterizing dilute-regime behavior, in part because I is not monotonic in ϕ over the entire range of volume fractions.[45] Specifically, when evaluated using the steady-shear pressure, I approaches zero in both the dense and dilute limits, achieving a maximum around $\phi \approx 0.2$. For this reason, we modify slightly the

definition of the inertial number to

$$I' \equiv \frac{\dot{\gamma} d}{\phi \sqrt{p/\rho_s}} = I/\phi \tag{35}$$

in order to provide a monotonic $I'(\phi)$ dependence. With $I' \to 0$ representing the dense limit and $I' \to \infty$ representing the dilute limit, we now can model the transition from dense to dilute behavior using a function of I'.

Conveniently, the original GD expression for the shear stress ratio can be expressed in terms of this inertial number. By combining Eqs. (1) and (2), we obtain

$$\eta_{\mathrm{GD}} = \beta_{\mathrm{GD}}(\phi) I' \tag{36}$$

with $\beta_{\mathrm{GD}}(\phi) \equiv \phi J/\sqrt{H}$. Similarly, our DEM η from Eq. (33) along with the DEM temperature from Eq. (29) yields

$$\eta_{\mathrm{DEM}}^{\mathrm{dilute}} = \beta(\phi) I' \tag{37}$$

with

$$\beta(\phi) \equiv \phi \psi J \sqrt{\frac{K}{K' H}}. \tag{38}$$

These expressions look similar in form to the dense-regime inertial-number model proposed by da Cruz *et al.*,[21] which reads as

$$\eta_{\mathrm{da\ Cruz}} = \eta_s + \alpha I, \tag{39}$$

except that the latter contains a constant yield stress ratio η_s added to the linear term. To obtain a comprehensive expression for η, we therefore can proceed with a linear dependence on the inertial number and simply allow its prefactor to transition between dense and dilute expressions. We propose to achieve this transition using a blending function

$$B(\alpha, \beta) = \alpha + (\beta - \alpha)\chi(I') \tag{40}$$

defined in terms of a quantity $\chi(I')$ that transitions from zero to unity according to

$$\chi(I') = \frac{1}{(I_0/I')^{1.5} + 1}. \tag{41}$$

The forms of B and χ are motivated by the $\eta(I)$ models of Jop *et al.*[22] and Chialvo *et al.*,[1] though the 1.5-power from the latter is chosen because a power greater than unity is needed to achieve a complete α-to-β transition. We then propose to write the shear stress ratio as

$$\eta_{\mathrm{DEM}} = \eta_s(\mu)\chi_s + B(\alpha, \beta) I', \tag{42}$$

with

$$\chi_s = 1 - \chi \tag{43}$$

so that, as volume fraction decreases, the contributions of η_s and α disappear commensurately. A comparison between this steady-state η model and the DEM results is shown in Fig. 10. As with the temperature and pressure, the fit for η is best for $\phi \gtrsim 0.2$. Additionally, though we find a small dependence of α on μ near $\mu = 0$, α is nearly constant with respect to μ for $\mu \gtrsim 0.1$; since most practical systems feature particles with friction coefficients in this range, we hence will assume α to be constant as in Ref. 1.

D. Modified dynamic equations

Having now captured the *steady-shear* DEM results of T, p, and η, we can now use these updated expressions to define correction factors to the *dynamic* GD equations. First, the pressure equation

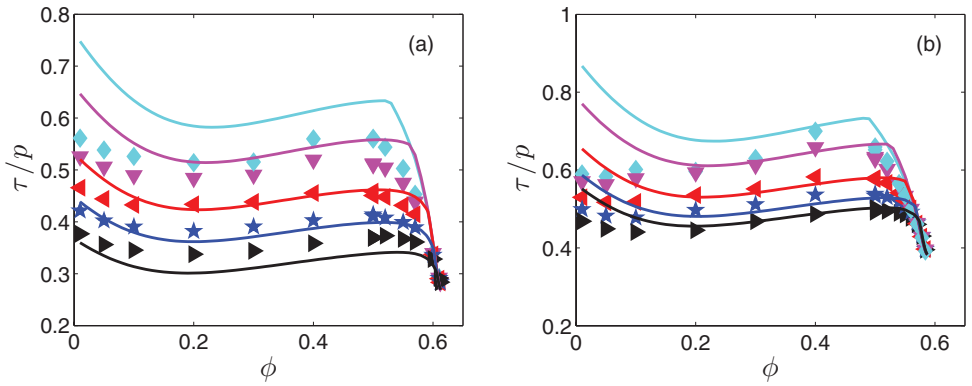

FIG. 10. Comparison of the new steady-state shear stress ratio model with DEM results. Shear stress ratio versus volume fraction is shown for (a) $\mu = 0.1$ and (b) $\mu = 0.5$. The agreement observed here between the KT and DEM predictions is substantially better than in Fig. 2. Symbols are the same as in Figs. 1 and 2.

remains unchanged from Eq. (1) except that g_0 is given by Eq. (31). Next, we write the new shear stress expression as the sum of a yield stress and an inertial stress, i.e.,

$$\tau = \tau_s + \tau_{\text{inertial}} \tag{44}$$

with

$$\tau_s = \eta_s \chi_s p \tag{45}$$

and

$$\tau_{\text{inertial}} = B(\alpha, \beta) I' p. \tag{46}$$

We also stipulate that only the inertial part τ_{inertial} will contribute to the viscous energy production rate – that is,

$$J_{\text{vis}} = \tau_{\text{inertial}} \dot{\gamma}. \tag{47}$$

This decomposition, though not necessary to predict a minimum flow angle in KT-type models,[24] is advantageous because it reproduces the observed dense-regime η behavior while also leaving open the possibility for η_s to be a function of microstructural variables (e.g., coordination number and fabric tensor[18]) that become rheologically important in close-packed systems and that could evolve independently of the KT equations; it also maintains the linear term in I' that naturally arises from the original GD model. As aforementioned, we can write τ_{inertial} alternatively as the GD expression for τ modified with a correction factor, i.e.,

$$\tau_{\text{inertial}} = \tau_{\text{GD}} \delta_\tau \tag{48}$$

with τ_{GD} given by Eq. (2) and

$$\delta_\tau = \frac{\alpha}{\beta} + \left[1 - \frac{\alpha}{\beta}\right] \chi. \tag{49}$$

Finally, the new energy dissipation rate expression is written as

$$\Gamma = \frac{\rho_s}{d} K'(\phi, e, \mu) T^{3/2} \delta_\Gamma. \tag{50}$$

By solving the steady-state condition in Eq. (13) and requiring $T = T_{\text{DEM}}$ from Eq. (29) and $\tau/p = \eta_{\text{DEM}}$ from Eq. (42), we can easily define the correction factor

$$\delta_\Gamma = \left(\frac{\beta\sqrt{H}}{K'M}\right) \delta_\tau. \tag{51}$$

TABLE I. Summary of model equations.

Primary equations	
Pressure:	$p = \rho_s HT$
Shear stress:	$\tau = \tau_s + \tau_{\text{inertial}}$
	$\tau_s = \eta_s \chi_s p$
	$\tau_{\text{inertial}} = \beta I' p\, \delta_\tau$
Energy dissipation rate:	$\Gamma = \frac{\rho_s}{d} K' T^{3/2} \delta_\Gamma$
Viscous energy production rate:	$J_{\text{vis}} = \tau_{\text{inertial}} \dot{\gamma}$
Secondary equations	
$\delta_\tau = \frac{\alpha}{\beta} + \left[1 - \frac{\alpha}{\beta}\right] \chi$	$g_0^{\text{CS}} = \frac{1-\phi/2}{(1-\phi)^3}$
$\delta_\Gamma = \left(\frac{\beta\sqrt{H}}{K'M}\right) \delta_\tau$	$g_0 = g_0^{\text{CS}} + \frac{\alpha_2 \phi^2}{[\phi_c(\mu)-\phi]^{3/2}}$
$\beta = \phi\psi J \sqrt{\frac{K}{K'H}}$	$e_{\text{eff}} = e - f(\mu)$
$H(\phi, e) = \phi[1 + 2(1+e)\phi g_0]$	$f(\mu) = \frac{3}{2}\mu \exp(-3\mu)$
$J(\phi, e) = \frac{5\sqrt{\pi}}{96}\eta^*$	$\psi = 1 + \frac{3}{10}(1-e^2)^{-2/3}[1 - \exp(-8\mu)]$
$K(\phi, e) = \frac{12}{\sqrt{\pi}}\phi^2 g_0 (1-e^2)$	$I' = \frac{\dot{\gamma} d}{\phi\sqrt{p/\rho_s}}$
$\eta^* = \eta_k^* + \eta_c^* + \eta_b^*$	$\chi = \frac{1}{(I_0/I')^{1.5}+1}$
$\eta_k^* = \frac{1-\frac{2}{5}(1+e)(1-3e)\phi g_0}{[1-\frac{1}{4}(1-e)^2-\frac{5}{24}(1-e^2)]g_0}$	$\chi_s = 1 - \chi$
$\eta_c^* = \frac{4}{5}(1+e)\phi g_0 \eta_k^*$	$K'(\phi, e, \mu) = K(\phi, e)\left(\frac{1-e_{\text{eff}}^2}{1-e^2}\right)$
$\eta_b^* = \frac{384}{25\pi}(1+e)\phi^2 g_0$	$M(\phi, e, \mu) = \max\left(\frac{J}{K'}, \frac{\alpha_1}{[\phi_c-\phi]^{1/2}}\right)$

We note that for frictionless particles in the dilute regime the original GD expressions are recovered. Additionally, the correction factor δ_Γ is related to the chain length L of Jenkins and Berzi,[31] with $L/d = \delta_\Gamma^{-1}$. This chain length is equal to the particle diameter in the dilute limit and grows rapidly as $\phi \to \phi_c$. It also produces $T \sim g_0^{1/3}$ under steady shear, a result similar to Jenkins and Berzi's[31] prediction that $T \sim g_0^{2/9}$.

It is important to mention that we have not addressed the need for corrections to the pseudothermal energy conductivity λ to account for interparticle friction and dense packing. Because our simulation approach produces homogeneous shear with no temperature gradients, it cannot be used to measure conductivity. Hence, we are unable to assess the original model or recommend any new corrections. However, we briefly mention two simple options. First, Jenkins and Berzi[31] left the original GD expression for λ unchanged, which is tantamount to setting $\lambda = \lambda_{\text{GD}}\delta_\lambda$ with $\delta_\lambda = 1$. The other option is to assume, based on the fact that the transport coefficients exhibit similar trends with respect to volume fraction, that $\delta_\lambda = \delta_\tau$. Though we cannot address this issue in the present study, we offer these two options and reserve their assessment for future work.

The complete model consists of the equations listed in Table I along with the constant parameters in Table II. As in the original GD model, all quantities are given as explicit functions of local system parameters (namely, volume fraction and shear rate) and particle-level properties (namely, material density, diameter, restitution coefficient, and friction coefficient).

TABLE II. Values of model constants. Values of the critical volume fraction ϕ_c and the yield stress ratio η_s are taken from Ref. 1.

μ-dependent parameters					
μ	0.0	0.1	0.3	0.5	1.0
ϕ_c	0.636	0.613	0.596	0.587	0.581
η_s	0.105	0.268	0.357	0.382	0.405
μ-independent parameters					
I_0		α	α_1		α_2
0.2		0.36	0.06		0.58

V. DISCUSSION

When applied to steady simple shear flows, the above dynamic model reproduces the temperature, pressure, and shear stress ratio results presented earlier in Figs. 5, 8, and 10 that the original GD theory is unable to predict. Moreover, the basic forms of the corrections used to achieve the improved performance all have precedent in the literature, as previous authors have proposed effective restitution coefficients to capture the effects of friction,[31,33] adjustable prefactors in the shear stress equation,[7,8,44] a characteristic chain length in the energy dissipation equation,[31] and expressions for the radial distribution function at contact that are based on simulation data.[26,29] Our work here builds upon these approaches and provides closures for the corrections in terms of local flow variables and particle properties.

An important finding of the present work is that corrections to the energy dissipation rate expression, such as those proposed by Jenkins and co-workers,[31,33] are *insufficient on their own* for extending traditional KT models to describe frictional and dense systems. Some aspects of the predictions are improved: the "chain length" correction reproduces an increase in temperature and a decrease in the shear stress ratio in the dense regime, and the effective restitution coefficient captures a decrease in temperature and pressure in the dilute regime as interparticle friction is increased. However, even when one constitutes these corrections based on DEM data, disparities between KT and DEM temperature and stresses remain. Hence, we choose to supplement the "chain length" and effective restitution coefficient with a modified radial distribution function at contact (to capture pressure), a correction factor to the shear stress, and decomposition of the shear stress into inertial and yield components. Though there are certainly other approaches one can take, they will necessarily involve modifications in the pressure and shear stress expressions. This point is consistent with the finding of Kumaran[14,25] that dense packing and particle roughness result in changes in the collision frequency and velocity distribution functions of a granular medium; in the full KT approach, the model expressions for energy dissipation rate, pressure, and shear stress are all derived from collision integrals involving the velocity distribution functions, so any change in the latter will necessarily produce changes in all of the former, not just the dissipation rate.

The proposed model has some key advantages over existing rheological models for granular materials. The first is its handling of the effects of friction. By acknowledging the decrease in ϕ_c upon increasing friction, the new model correctly predicts a corresponding increase in pressure in the dense regime. Previous kinetic theories accounting for friction neglect this effect and hence predict a decrease in pressure at all volume fractions resulting from increased dissipation and decreased temperature.[31,33] Second, while kinetic theory has long been used for modeling dilute flows, and while inertial-number models have proven successful for many dense flows, only very recently have the two been bridged to handle systems with wide variations in packing.[46] Although this model did not account for interparticle friction or for dense-regime e-dependence, the good agreement between its predictions and experimental results for a number of flow problems is quite promising and motivates the more general bridging performed here. Finally, the recasting of the inertial-number description into a kinetic theory framework (1) makes the model compatible with boundary conditions involving granular temperature that are more sophisticated than the simple no-slip condition and (2) enables the model to account for nonlocal effects via the conduction of pseudothermal energy. Inertial-number models are typically coupled with the no-slip wall conditions whose validity may be questionable depending on system and particle properties (an issue we aim to address in a later work), while KT models afford the option of wall slip conditions connected to fluctuating energy and the inelasticity of particle-wall collisions.[44,47] This fluctuating energy, furthermore, can vary spatially and produce nonlocal rheological effects, which recent work has shown to be of substantial importance even in the dense systems for which inertial-number models were designed.[23] While the "fluidity" approach in Ref. 23 (and also Ref. 48) is currently limited to the dense regime, the extended KT scheme presented here offers a way to account for nonlocality over the full range of volume fractions below jamming.

On the other hand, the proposed model does exhibit several weaknesses resulting in part from the approach taken in its development. Among the most salient of these is the overprediction of granular temperature in the very dilute regime ($\phi \lesssim 0.2$). Had we allowed the effective restitution

coefficient to vary with volume fraction, we would have been able to capture the temperature more closely in this region. However, because the ϕ-dependence is neither simple nor consistent across all cases of e and μ, we choose to define $e_{\text{eff}}(e, \mu)$ as a constant, with higher importance placed on capturing cases where $\phi \gtrsim 0.2$. This definition is also more satisfying since e_{eff} is conceptually a particle property rather than an ensemble one. The disparity in very dilute cases, rather than arising from a poorly constituted e_{eff}, is more likely the result of neglecting rotational degrees of freedom. The GD model is derived for smooth, frictionless particles and hence does not track rotational kinetic energy. In this context, conversion of translational energy to rotational energy is treated as an additional mode of translational energy dissipation, and so the parameter e_{eff} must encapsulate both real energy dissipation and loss to rotation. The extent of to which one mode predominates over the other may vary with volume fraction and therefore invalidate the assumption of a constant effective restitution coefficient. This problem is mitigated, though, by the fact that flow problems of practical interest manifesting such dilute regions tend to be heavily fluidized; hence, flow behavior in these regions is dictated primarily by the fluid-particle drag law, rendering any error in the solids-phase stress model rather inconsequential. Dense-phase predictions of the solids-phase stress, therefore, are most important to capture, and the corrections outlined in this work are weighted accordingly.

Another weakness of the present model is its reliance on empiricism, particularly in the corrections for the shear stress. Some of this need can likely be alleviated by considering rotational degrees of freedom, as the GD model and our modified version of it do not account for the dependence of the shear stress on the rotational temperature. It is possible, therefore, to start not with the GD model as the basis for modifications to account for friction and dense packing but rather with another existing KT model that considers particle rotation.[10,11] The effects of friction can be included in such models by defining not only an effective normal restitution coefficient as done here but also an effective tangential restitution coefficient, which has been employed previously with some success.[34] The inclusion of dense-regime effects can then be pursued as per the present work by defining a "chain length" correction and a new g_0 expression. Even these tasks are encumbered by the empirical approach, as there is little agreement in the literature in regard to the precise dense-regime scalings for the stresses and temperature with respect to $\phi_c - \phi$ [Ref. 49]. Our findings that $T \sim (\phi_c - \phi)^{-1/2}$, $g_0 \sim (\phi_c - \phi)^{-3/2}$, and $p \sim (\phi_c - \phi)^{-2}$ in the dense regime are simply our best estimates based on our DEM data, and more work needs to be done to determine the reason for the variety of exponents proposed in the literature. Finally, the determination of ϕ_c itself must be done empirically and as such has produced varying results. In particular, among recent works considering "rough"-particle shear flows, one finds that ϕ_c is independent of the normal restitution coefficient and is purely a function of μ [Ref. 1] while others show ϕ_c to vary with both normal and tangential restitution coefficients.[25,50] These works agree in their finding that roughness, whether measured by friction or tangential restitution, decrease ϕ_c from its value in the smooth, frictionless case ($\phi_c \approx 0.64$), but the contrary results regarding the influence of the normal restitution coefficient are hitherto unexplained and merit further study. The DEM data in the present work support the idea that $\phi_c(\mu)$, and since these data form the basis for our empirical modifications to the GD model we move forward with such a form.

Related to the jamming point ϕ_c is the rise of the particle stiffness k as a rheologically important parameter. The KT approach assumes that particle collisions are instantaneous and hence that particles are infinitely hard (i.e., $k \to \infty$). For this reason, in the present work we have made certain to consider only cases in which Bagnold scaling holds and hence the finite stiffness plays no role — that is, cases in the inertial regime. A truly complete rheological model, however, would be capable of describing both infinitely and finitely stiff particles and hence would span the inertial, quasistatic, and intermediate regimes. Much work has been done recently to elucidate differences between hard- and soft-particle rheology[50,51] and to quantify the rheology of soft particles in elastic and inertial regimes.[1–3,49,51–55] One recent work[1] proposes a way to bridge the rheology of the inertial regime with the two elastic regimes by smoothly incorporating stiffness dependence to an extent governed by the dimensionless parameter $\hat{\dot{\gamma}} \equiv \dot{\gamma} d / \sqrt{k/\rho_s d}$. Such an approach can be applied regardless of the choice of inertial-regime model, including the one described here, and could conceivably be coupled with more complex plasticity or hypoplasticity models for quasistatic flows.

A final drawback of the current approach is that the modifications made to the GD model, while appealing to micro- or mesoscopic concepts, are all rheological (i.e., macroscopic) in nature. In deriving KT models, one generally begins by describing the details of a single collision and the velocity distribution of a pair of particles — that is, model construction begins at the microscale and builds upwards. The approach taken here, though, makes measurements at the macroscopic level and uses them to constitute parameters that have a physical interpretation at smaller scales. The chain length correction, for example, can be interpreted as a mesoscopic length of a typical granular chain[31] or microscopically as the result of dense-regime velocity correlations.[25] The effective restitution coefficient is a microscopic metric of dissipation during the collision of two particles.[33] The radial distribution function at contact g_0 is already microscopic in nature, and our modification to it accounts in a phenomenological way for anisotropy of particle collisions (which is also a microscale effect). The correction to the shear stress, on the other hand, is mostly rheological, though the inertial number that appears therein can be interpreted as a ratio of time scales of macroscopic shear and microscopic particle rearrangement.[21] In some regard, however, the connection between our proposed values for the micro-/mesoscale quantities and their physically measurable counterparts is one of analogy more so than equality.

An alternative approach to the present one is, of course, to perform a rigorous KT derivation that includes provisions for friction and dense packing. The problem with this approach, as discussed in the Introduction, is the difficulty in obtaining a closed-form model. A collision integral involving a tangential impulse proportional to the normal one (via μ) appears to require numerical solution, as does the integral for the non-Gaussian relative velocity distribution function that arises in dense flows[14] — and even this distribution function is determined empirically. For the time being, the most promising approach toward developing a comprehensive rheological model appears to be modification of existing KT models for dilute flows of frictionless particles.

VI. SUMMARY

We investigate the influence of dense packing and interparticle friction on granular rheology in the inertial regime. From DEM simulations of homogeneous simple shear flows, we observe good agreement with the KT of GD[4] in regard to predictions of pressure, shear stress ratio, and temperature in the case of frictionless particles below $\phi_f \approx 0.49$; however, for denser systems or for frictional particles, there is a substantial discrepancy between the simulation and GD results. Based on previous strategies in the literature for modifying the kinetic theory, we propose simple corrections to the GD model to bring its predictions closer to those of our DEM simulations. These corrections include an effective restitution coefficient to capture the increased dissipation resulting from friction,[33] a chain length correction to the energy dissipation rate,[31] a new expression for the radial distribution function at contact, and a correction factor to the shear stress equation to reflect the influence of friction in the dilute regime as well as to reproduce inertial-number scalings in the dense regime.[1,20–22] These new terms are then constituted in terms of particle-level properties and system parameters from our DEM simulations to produce a more complete rheological model. This model may then be implemented in continuum-model simulations to investigate large-scale flows of frictional particles over a wide range of volume fractions such as those found in numerous important flow problems including chutes, hoppers, and fluidized beds.

ACKNOWLEDGMENTS

We gratefully acknowledge the support of (U.S.) Department of Energy (DOE)/NETL Grant No. DE-FE0006932.

[1] S. Chialvo, J. Sun, and S. Sundaresan, "Bridging the rheology of granular flows in three regimes," Phys. Rev. E **85**, 021305 (2012).
[2] G. Lois and J. M. Carlson, "Force networks and the dynamic approach to jamming in sheared granular media," Europhys. Lett. **80**, 58001 (2007).
[3] C. S. Campbell, "Granular shear flows at the elastic limit," J. Fluid Mech. **465**, 261–291 (2002).
[4] V. Garzó and J. W. Dufty, "Dense fluid transport for inelastic hard spheres," Phys. Rev. E **59**, 5895–5911 (1999).

[5] C. K. K. Lun, S. B. Savage, D. J. Jeffrey, and N. Chepurniy, "Kinetic theories for granular flow: Inelastic particles in Couette flow and slightly inelastic particles in a general flowfield," J. Fluid Mech. **140**, 223–256 (1984).
[6] J. T. Jenkins and M. W. Richman, "Kinetic theory for plane flows of a dense gas of identical, rough, inelastic, circular disks," Phys. Fluids **28**, 3485–3494 (1985).
[7] J. T. Jenkins and S. B. Savage, "A theory for the rapid flow of identical, smooth, nearly elastic, spherical particles," J. Fluid Mech. **130**, 187–202 (1983).
[8] K. Agrawal, P. N. Loezos, M. Syamlal, and S. Sundaresan, "The role of meso-scale structures in rapid gas–solid flows," J. Fluid Mech. **445**, 151–185 (2001).
[9] J. Bougie, J. Kreft, J. B. Swift, and H. L. Swinney, "Onset of patterns in an oscillated granular layer: Continuum and molecular dynamics simulations," Phys. Rev. E **71**, 021301 (2005).
[10] C. K. K. Lun, "Kinetic theory for granular flow of dense, slightly inelastic, slightly rough spheres," J. Fluid Mech. **233**, 539–559 (1991).
[11] V. Kumaran, "The constitutive relation for the granular flow of rough particles, and its application to the flow down an inclined plane," J. Fluid Mech. **561**, 1–42 (2006).
[12] A. Ferguson, B. Fisher, and B. Chakraborty, "Impulse distributions in dense granular flows: Signatures of large-scale spatial structures," Europhys. Lett. **66**, 277 (2004).
[13] A. Ferguson and B. Chakraborty, "Stress and large-scale spatial structures in dense, driven granular flows," Phys. Rev. E **73**, 011303 (2006).
[14] V. Kumaran, "Dynamics of dense sheared granular flows. Part II. The relative velocity distributions," J. Fluid Mech. **632**, 145–198 (2009).
[15] A. Drescher and G. de Josselin de Jong, "Photoelastic verification of a mechanical model for the flow of a granular material," J. Mech. Phys. Solids **20**, 337–340 (1972).
[16] S. Luding, "Micro–macro transition for anisotropic, frictional granular packings," Int. J. Solids Struct. **41**, 5821–5836 (2004).
[17] M. Alam and S. Luding, "Energy nonequipartition, rheology, and microstructure in sheared bidisperse granular mixtures," Phys. Fluids **17**, 063303 (2005).
[18] J. Sun and S. Sundaresan, "A constitutive model with microstructure evolution for flow of rate-independent granular materials," J. Fluid Mech. **682**, 590–616 (2011).
[19] N. Mitarai and H. Nakanishi, "Velocity correlations in dense granular shear flows: Effects on energy dissipation and normal stress," Phys. Rev. E **75**, 031305 (2007).
[20] GDR MiDi, "On dense granular flows," Eur. Phys. J. E **14**, 341–365 (2004).
[21] F. da Cruz, S. Emam, M. Prochnow, J.-N. Roux, and F. Chevoir, "Rheophysics of dense granular materials: Discrete simulation of plane shear flows," Phys. Rev. E **72**, 021309 (2005).
[22] P. Jop, Y. Forterre, and O. Pouliquen, "A constitutive law for dense granular flows," Nature (London) **441**, 727–730 (2006).
[23] K. Kamrin and G. Koval, "Nonlocal constitutive relation for steady granular flow," Phys. Rev. Lett. **108**, 178301 (2012).
[24] V. Kumaran, "Dense granular flow down an inclined plane: From kinetic theory to granular dynamics," J. Fluid Mech. **599**, 121–168 (2008).
[25] V. Kumaran, "Dynamics of dense sheared granular flows. Part 1. Structure and diffusion," J. Fluid Mech. **632**, 109–144 (2009).
[26] S. Torquato, "Nearest-neighbor statistics for packings of hard spheres and disks," Phys. Rev. E **51**, 3170–3182 (1995).
[27] S. Ogawa, A. Umemura, and N. Oshima, "On the equations of fully fluidized granular materials," Z. Angew. Math. Phys. **31**, 483–493 (1980).
[28] C. Lun and S. Savage, "The effects of an impact velocity dependent coefficient of restitution on stresses developed by sheared granular materials," Acta Mech. **63**, 15–44 (1986).
[29] K. A. Reddy and V. Kumaran, "Applicability of constitutive relations from kinetic theory for dense granular flows," Phys. Rev. E **76**, 061305 (2007).
[30] C. Song, P. Wang, and H. A. Makse, "A phase diagram for jammed matter," Nature (London) **453**, 629–632 (2008).
[31] J. T. Jenkins and D. Berzi, "Dense inclined flows of inelastic spheres: Tests of an extension of kinetic theory," Granular Matter **12**, 151–158 (2010).
[32] S. Luding, "Towards dense, realistic granular media in 2D," Nonlinearity **22**, R101 (2009).
[33] J. T. Jenkins and C. Zhang, "Kinetic theory for identical, frictional, nearly elastic spheres," Phys. Fluids **14**, 1228–1235 (2002).
[34] O. Herbst, R. Cafiero, A. Zippelius, H. J. Herrmann, and S. Luding, "A driven two-dimensional granular gas with Coulomb friction," Phys. Fluids **17**, 107102 (2005).
[35] D. Ertaş and T. C. Halsey, "Granular gravitational collapse and chute flow," Europhys. Lett. **60**, 931 (2002).
[36] O. Baran, D. Ertaş, T. C. Halsey, G. S. Grest, and J. B. Lechman, "Velocity correlations in dense gravity-driven granular chute flow," Phys. Rev. E **74**, 051302 (2006).
[37] P. A. Cundall and O. D. L. Strack, "A discrete numerical model for granular assemblies," Geotechnique **29**, 47–65 (1979).
[38] N. F. Carnahan and K. E. Starling, "Equation of state for nonattracting rigid spheres," J. Chem. Phys. **51**, 635–636 (1969).
[39] S. Plimpton, "Fast parallel algorithms for short-range molecular dynamics," J. Comput. Phys. **117**, 1–19 (1995).
[40] L. E. Silbert, D. Ertaş, G. S. Grest, T. C. Halsey, D. Levine, and S. J. Plimpton, "Granular flow down an inclined plane: Bagnold scaling and rheology," Phys. Rev. E **64**, 051302 (2001).
[41] H. King, R. White, I. Maxwell, and N. Menon, "Inelastic impact of a sphere on a massive plane: Nonmonotonic velocity-dependence of the restitution coefficient," Europhys. Lett. **93**, 14002 (2011).
[42] A. Stevens and C. Hrenya, "Comparison of soft-sphere models to measurements of collision properties during normal impacts," Powder Technol. **154**, 99–109 (2005).
[43] A. W. Lees and S. F. Edwards, "The computer study of transport processes under extreme conditions," J. Phys. C **5**, 1921 (1972).

[44] P. C. Johnson and R. Jackson, "Frictional-collisional constitutive relations for granular materials, with application to plane shearing," J. Fluid Mech. **176**, 67–93 (1987).
[45] Y. Forterre and O. Pouliquen, "Flows of dense granular media," Annu. Rev. Fluid Mech. **40**, 1–24 (2008).
[46] S. Schneiderbauer, A. Aigner, and S. Pirker, "A comprehensive frictional-kinetic model for gas–particle flows: Analysis of fluidized and moving bed regimes," Chem. Eng. Sci. **80**, 279–292 (2012).
[47] J. T. Jenkins, "Boundary conditions for rapid granular flow: Flat, frictional walls," J. Appl. Mech. **59**, 120–127 (1992).
[48] V. B. Nguyen, T. Darnige, A. Bruand, and E. Clement, "Creep and fluidity of a real granular packing near jamming," Phys. Rev. Lett. **107**, 138303 (2011).
[49] B. P. Tighe, E. Woldhuis, J. J. C. Remmers, W. van Saarloos, and M. van Hecke, "Model for the scaling of stresses and fluctuations in flows near jamming," Phys. Rev. Lett. **105**, 088303 (2010).
[50] K. A. Reddy and V. Kumaran, "Dense granular flow down an inclined plane: A comparison between the hard particle model and soft particle simulations," Phys. Fluids **22**, 113302 (2010).
[51] M. Otsuki, H. Hayakawa, and S. Luding, "Behavior of pressure and viscosity at high densities for two-dimensional hard and soft granular materials," Prog. Theor. Phys. Suppl. **184**, 110–133 (2010).
[52] P. Olsson and S. Teitel, "Critical scaling of shear viscosity at the jamming transition," Phys. Rev. Lett. **99**, 178001 (2007).
[53] T. Hatano, "Scaling properties of granular rheology near the jamming transition," J. Phys. Soc. Jpn. **77**, 123002 (2008).
[54] K. N. Nordstrom, E. Verneuil, P. E. Arratia, A. Basu, Z. Zhang, A. G. Yodh, J. P. Gollub, and D. J. Durian, "Microfluidic rheology of soft colloids above and below jamming," Phys. Rev. Lett. **105**, 175701 (2010).
[55] A. Latz and S. Schmidt, "Hydrodynamic modeling of dilute and dense granular flow," Granular Matter **12**, 387–397 (2010).

11 Appendix C

Please see the next page for the manuscript "Boundary conditions for dense, wall-bounded ows of granular material."

Boundary conditions for dense, wall-bounded flows of granular material

Sebastian Chialvo,[1] Ali Ozel,[1] Olivier Bonnefoy,[2] and Sankaran Sundaresan[1]

[1] *Chemical and Biological Engineering Department, Princeton University, Princeton, NJ 08540, USA*

[2] *Ecole Nationale Supérieure des Mines de Saint Etienne, Centre SPIN, LPMG FRE 3312, 158 Cours Fauriel, 42023 Saint Etienne Cedex 2, France*

(Dated: September 18, 2015)

Abstract

Continuum modeling of granular materials in most practical applications requires specification of boundary conditions at the walls of the system geometry. Unlike with molecular fluids, which under most circumstances obey no-slip behavior, granular materials exhibit complex and varied slip behavior depending on flow-field conditions and particle-particle and particle-wall interaction properties. The nature of these dependencies becomes more challenging to investigate from a theoretical perspective in dense flows, which are less amenable to the traditional kinetic-theory approach and therefore require more empirical modeling strategies. Additionally, practical continuum modeling applications tend not to consider particle rotation or resolve near-wall boundary layer formation of the particulate phase, tasks which can add undesired model complexity and computational expense to the problem. In this work, we expand upon previous simulation studies of wall-bounded granular flows by investigating slip behavior in simple-shear simulations of soft, frictional spheres over a range of volume fractions and friction coefficients. We introduce a novel scaling based on granular viscosity and use it to collapse data of the 'surface' slip velocity, which includes rotational and boundary-layer velocity contributions, and propose an empirical model for use in finely-resolved flow problems considering both translational and angular velocity fields. We then separately constitute the rotational contribution to produce a slip velocity model for use in finely-resolved, translation-only flow problems. Finally, we coarse-grain the model by subsuming the boundary-layer contribution into the boundary condition, in analogy to the wall functions used in turbulence modeling, to produce a constitutive expression for use in coarsely-resolved flows considering only translational motion — *i.e.* the vast majority of applications.

PACS numbers: 45.70.-n, 47.57.Gc, 64.60.F-, 64.70.ps, 83.10.Gr, 83.80.Fg

I. INTRODUCTION

Flows of granular material are found in many industrial and natural processes, and attempts to model these flows often rely on continuum approaches. The development of rheological models for granular materials has progressed substantially over the past three decades. For dilute flows, numerous kinetic-theory models have been developed [1–6]; for dense flows, inertial-number models have proven successful [7–9]; and recently methods to bridge dense and dilute behavior have been proposed [10, 11]. However, application of these rheological models to practical flow problems requires the specification of boundary conditions (BCs) at the system walls, and similarly advanced development of robust BC models to predict wall slip behavior remains an open challenge.

Most of the development of wall BCs for granular flows has been limited to dilute flows. Models for this regime generally track the granular fluctuation energy in addition to velocity and volume fraction and hence require two BC equations: one for the shear stress and one for the flux of fluctuation energy [12, 13]. Both equations contain explicit dependences on the slip velocity as well as particle/wall properties such as the normal [12–17] and tangential [14–17] restitution coefficients, the particle-wall friction coefficient [14–16], and the (phenomenological) specularity coefficient [12]. These BC models are coupled with kinetic-theory rheological models that relate stresses to fluctuation energy, which itself evolves dynamically according to a balance equation containing a (nonlocal) flux term. In the dense regime, however, traditional kinetic-theory rheological models are less successful because different physics predominate under dense and dilute conditions, with dilute flows characterized by uncorrelated binary collisions (often termed 'molecular chaos') while dense flows exhibit correlations in relative velocity distributions [18]. Inertial-number models [7–9], in which the stresses (and/or the shear stress ratio) are simple algebraic functions of particle concentration and shear rate, have been shown to yield reasonably good predictions of velocity profiles in dense flow systems [8, 10]. It is natural to expect, therefore, that dilute-regime BC models likewise would underperform when applied to dense flow problems and would necessitate the development of new BC formulations specifically for dense flows.

Indeed, recent work by Artoni and coworkers [19, 20] has revealed details about slip behavior in dense granular flows, on the basis of which the authors propose new BC expressions. However, their investigations were limited to two-dimensional systems of polygonal

particles with a limited range of particle concentrations, wall friction coefficients, and particle properties. Shojaaee *et al.* build upon this work by expanding the range of particle and wall friction coefficients investigated but do not provide a constitutive model for the slip velocity [21, 22]. These efforts thus motivate the first aim of this study, which is the development of a wall BC model applicable to flows with a wide array of particle/wall friction coefficients and solids concentrations within the dense regime.

Whether modeling dense or dilute flows, there remains another problem with specifying wall BCs for continuum modeling of practical flow systems: resolution of the boundary layer near the wall. Existing BC models relate the slip velocity to field variables evaluated at the wall; these field variables can vary substantially over the thickness of the boundary layer, which is generally $\sim 10d$ in thickness [23]. Hence, meaningful application of the BC requires adequately resolving the flow in the boundary layer. The computational costs of this task, though, are prohibitively high for most systems of practical interest (such as fluidized beds, risers, and hoppers), whose length scale of $\mathcal{O}(1\text{ m})$ is much larger than the particle diameter of $\mathcal{O}(100\ \mu\text{m})$. Eliminating the need to resolve the near-wall region would result in substantial savings in computational time. Additionally, in continuum simulations a boundary layer is predicted only if nonlocal conduction terms are included in the rheological model. These nonlocal terms can appear, for example, as a conduction term in the balance equation for granular energy (*e.g.* [1, 2, 12]) or in equations for other attributes such as 'fluidity' [24] or an order parameter related to the fraction of 'fluidlike' interparticle contacts [25, 26]. However, such equations, by virtue of being partial differential equations, add substantial complexity to the model that further increases computational time with respect to that required by a simple, algebraic rheological model. The reason is that numerical solution of the additional scalar field requires another iteration procedure to account for the field's spatial gradients. This burden does not exist with an algebraic formulation, a benefit that, in the case of kinetic-theory modeling of granular flows, has motivated the use of local, algebraic versions of the granular energy equation that remove gradient terms and simply equate production and dissipation terms [27, 28]. Therefore, the development of a BC model that subsumes the boundary layer and can be paired with a local rheological model is of practical interest, and such is the second aim of this study.

II. SIMULATION METHODS

We employ the spring-dashpot model [29], for which the normal and tangential forces on a spherical particle i resulting from the contact of two identical spheres i and j are

$$F_{n_{ij}} = f(\frac{\delta_{ij} d}{4})[k_n \delta_{ij} n_{ij} - \gamma_n m_{\text{eff}} v_{n_{ij}}], \tag{1}$$

$$F_{t_{ij}} = f(\frac{\delta_{ij} d}{4})[-k_t u_{t_{ij}} - \gamma_t m_{\text{eff}} v_{t_{ij}}], \tag{2}$$

where δ_{ij} is the overlap distance, k_n and k_t are spring elastic constants, γ_n and γ_t are viscous damping constants, $m_{\text{eff}} = m_i m_j/(m_i + m_j)$ is the effective mass of spheres with masses m_i and m_j, $v_{n_{ij}}$ and $v_{t_{ij}}$ are the normal and tangential components of relative particle velocity, and $u_{t_{ij}}$ is the elastic shear displacement. For Hookean contact, $f(x) = 1$, while for Hertzian contact, $f(x) = \sqrt{x}$. The magnitude of tangential force is limited by a static yield criterion, $|F_{t_{ij}}| \leq \mu |F_{n_{ij}}|$, where μ is the particle friction coefficient. We set values of $k_t/k_n = 2/7$ and $\gamma_t = 0$. For Hookean contact, γ_n is chosen such that the restitution coefficient $e = \exp\left(-\gamma_n \pi/\sqrt{4k_n/m_{\text{eff}} - \gamma_n^2}\right) = 0.7$. For Hertzian contact, we employ the same value for $\gamma_n/\sqrt{k_n/m_{\text{eff}}}$. We likewise set a wall-particle friction coefficient μ_w, wall stiffness $k_w = k$, and wall restitution coefficient $e_w = e$. We perform the discrete element method (DEM) simulations using LAMMPS [30] for the linear spring-dashpot (Hookean) model and LIGGGHTS [31] for the non-linear spring-dashpot (Hertzian) model.

$$\boldsymbol{\sigma} = \frac{1}{V} \sum_i \left[\sum_{j \neq i} \frac{1}{2} \mathbf{r}_{ij} \mathbf{F}_{ij} + m_i (\mathbf{v}_i')(\mathbf{v}_i') \right], \tag{3}$$

where V is the box volume, $\mathbf{r}_{ij}$ is the center-to-center contact vector from particle j to particle i, and $\mathbf{v}_i' \equiv \mathbf{v}_i - \langle \mathbf{v} \rangle(\mathbf{x})$ is the particle fluctuation velocity, *i.e.* the difference between its instantaneous velocity $\mathbf{v}_i$ and the time-averaged streaming velocity $\langle \mathbf{v} \rangle$ at position $\mathbf{x}$. The mean streaming velocity is zero in the y- and z-directions but is not known in the x-direction at runtime; it must be calculated in post-processing.

Two wall boundaries are placed at $y = \pm H/2$, and the gap of height H between them is filled with particles to achieve the desired ensemble-average volume fraction $\bar{\phi}$. Shear is then induced by moving the top wall at a velocity $+U_{\text{wall}}$ and the bottom wall at a velocity $-U_{\text{wall}}$ in the x-direction. Shearing proceeds for a dimensionless time of $\dot{\gamma}_{\text{wall}} t = 1000$ to ensure that steady state has been reached; here, $\dot{\gamma}_{\text{wall}} \equiv 2U_{\text{wall}}/H$ is the apparent shear rate, which will differ from the actual local shear rate $\dot{\gamma}$ because of wall slip. During the simulation,

1000 snapshots of particle position, velocity, and stress are saved for post-processing. In post-processing, we perform a volume-weighted binning to calculate the field variables; that is, a particle whose volume crosses one or more bin boundaries will have its contribution to the volume fraction, velocity, *etc.* distributed across the bins in proportion to the fraction of its volume lying in each bin. Quantities reported as boundary values and denoted as $(\cdot)_w$ are, in fact, measured at a distance of $d/2$ away from the wall, as this is the closest point to the wall that a particle center can reach; the best location for wall measurements, however, is a small but still open question [32]. After performing the binning procedure on each snapshot, the snapshots are then averaged together to yield time-averaged quantities. From the stress data, we calculate a shear stress $\tau \equiv \frac{1}{2}(\sigma_{xy} + \sigma_{yx})$ and an approximate pressure $p \equiv \frac{1}{2}(\sigma_{yy} + \sigma_{zz})$. This pressure is approximate since it excludes the normal stress in the flow direction, the data for which are unreliable because the (nonzero) true streaming velocity at a given position will deviate from the mean value calculated for the bin containing this position. However, since normal stress differences are typically of the order of 10% of the mean normal stress for shear flows [33], we consider this approximation acceptable. We can then define the shear stress ratio, also commonly called the bulk friction coefficient, as $\eta \equiv \tau/p$ and the granular viscosity as $\nu \equiv \tau/\dot{\gamma}$. All macroscopic quantities will be presented in dimensionless form, scaled by some combination of the particle diameter d, stiffness $k = k_n$, and solid material density ρ_s.

III. RESULTS

A. Core and boundary regions

As described in previous works [21, 34], wall-bounded shear flows exhibit two regions of flow: 1) a central or *core* region characterized by spatially-invariant, local rheology and 2) a boundary region within about $10d$ of each wall featuring strong gradients in shear rate $\dot{\gamma}$ and volume fraction ϕ due to non-local conduction of granular energy. Indeed we observe these regions in our simulations, as demonstrated in Figure 1, where exponential tails towards the walls are clearly visible for the shear rate, volume fraction, and granular temperature. The measured pressure p and shear stress ratio η are found to obey local, inertial-number rheological behavior [7, 9] in the core region, as shown in Figure 2. This local behavior in

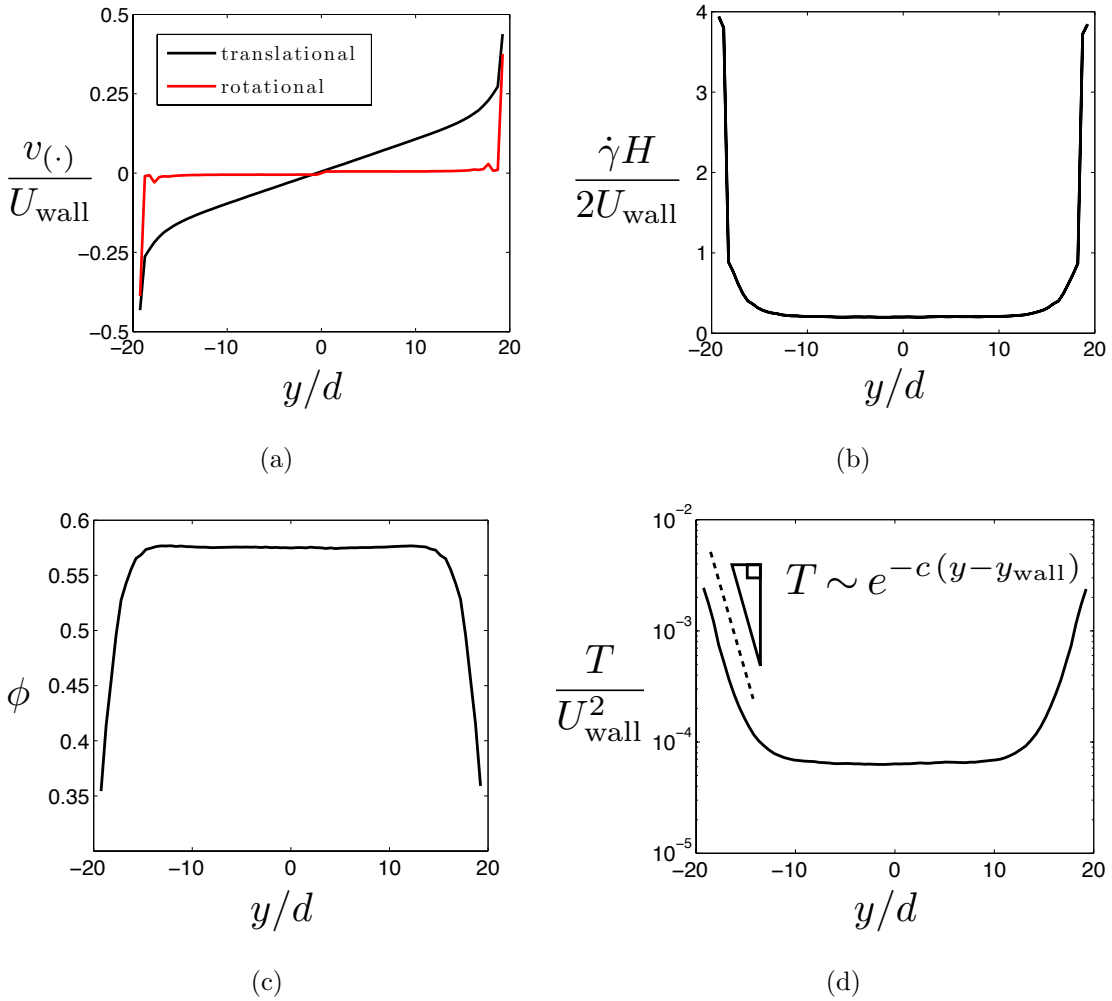

FIG. 1. Profiles of (a) velocity, (b) shear rate, (c) volume fraction, and (d) granular temperature vs. position between wall boundaries for Hookean contact. The interparticle friction coefficient and wall-particle friction $\mu = \mu_w = 0.5$ and $\bar{\phi} = 0.55$. Quantities are scaled by wall velocity U_{wall} and gap width H. A core region with spatially invariant rheological properties is observed to lie between boundary layers of thickness $\sim 10d$ at each wall. Exponential tails are observed in the boundary layers. Analogous results were obtained for Hertzian contact model as well (not shown).

the core supports the notion that a BC model that absorbs the near-wall behavior can be successfully coupled with a simple, local rheological model without the need for inclusion of further complexity to the rheology.

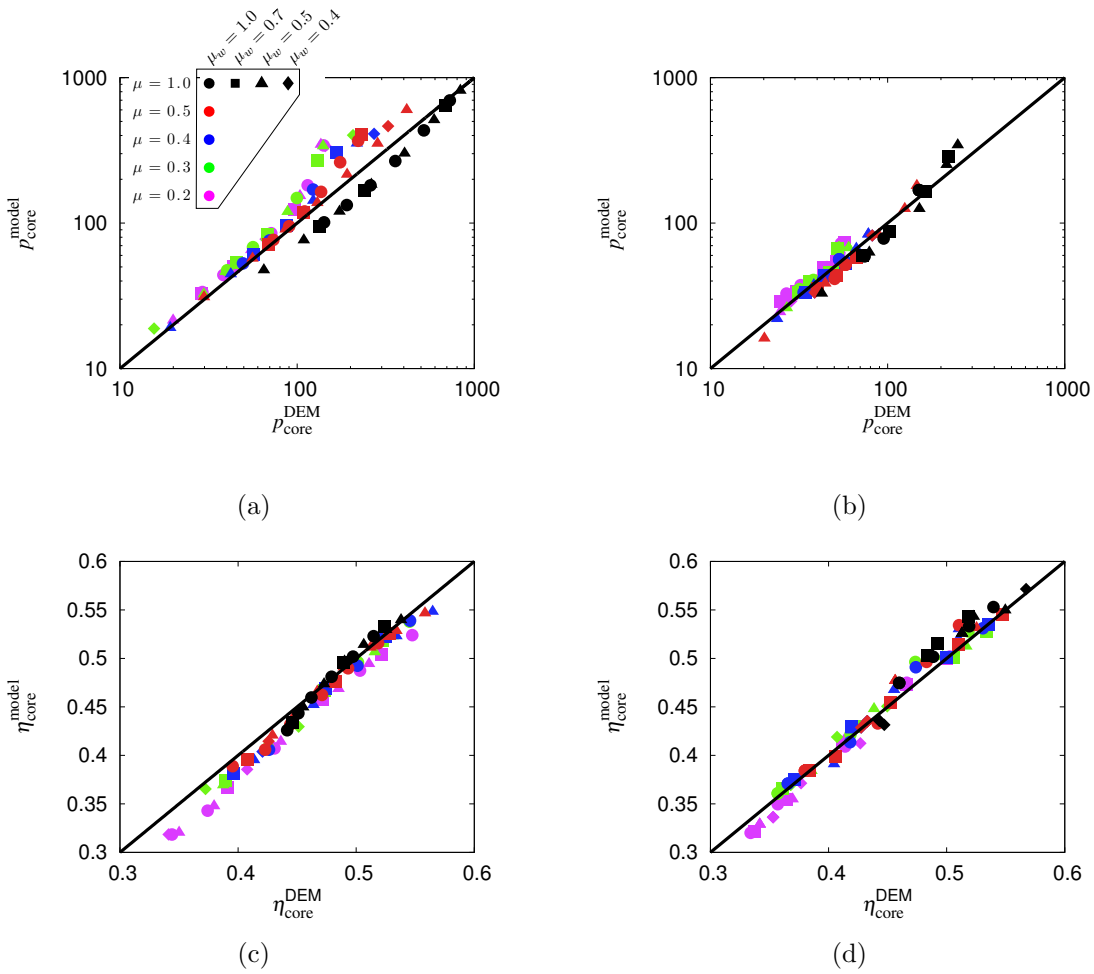

FIG. 2. Comparison of core data for scaled pressure and shear stress ratio with predictions of the local rheological model of Chialvo *et al.* [9](Eqs. (7)-(10)) and Gu *et al.* [35] (Eqs. (6),(20)-(22)). (a) scaled pressure for Hookean contact versus the rheological model of Chialvo *et al.* [9], (b) scaled pressure for Hertzian contact versus the rheological model of Gu *et al.* [35], (c) shear stress ratio for Hookean contact versus the rheological model of Chialvo *et al.* [9], (d) shear stress ratio for Hertzian contact versus the rheological model of Gu *et al.* [35]. Reasonably good agreement confirms the locality of the rheological behavior in the core.

For some combinations of parameters, we observe that the friction of the walls is insufficient to generate sustained shear in the particle assembly, a phenomenon that has also been observed in a previous work using the contact dynamics method [22]. In an effort to determine whether this non-shearing state is dependent on initial configuration, we perform low-μ_w simulations starting with a pre-sheared initial condition, *i.e.* one generated from shearing with a sufficiently frictional wall. As seen in Figure 3a, such a simulation begins with a volume fraction profile qualitatively similar to that in Figure 1c; however,

as shearing progresses under the new, low-μ_w conditions, the particle layers closest to the wall lose pseudothermal energy and begin to accumulate near the wall. This movement of particles towards the wall results in a depletion of particles in the core, producing a profile that is inverted with respect to the core-concentrated, fully sheared case. Additionally, the cooling process is accompanied by ordering of the particles near the wall (Figure 1a) and by a slow decrease in the observed shear rate over time (Figure 1b). Because our aim in this study is to develop a BC model for amorphous granular media, we deem it more valuable at present to focus our attention on the range of μ_w values that produces sustained shear. Previous two-dimensional shear simulations suggest that the lower bound for this range is $\mu_w^* \approx 0.25$ [22]; our simulations in three dimensions suggest a different value of $\mu_w^* \approx 0.33$. While it is possible that this critical value of the particle-wall friction coefficient should vary with particle and flow parameters, more cases of μ_w near μ_w^* need to be simulated in order to elucidate the dependences on these parameters. This task is outside the scope of the present work and is reserved for follow-up studies.

B. Dimensionless slip velocities and BC model

In seeking a BC model, there are several different definitions of slip velocity that one can consider. Specifically, these definitions differ in how the velocity of the granular medium is described. The options described below are summarized in Table II. We note that, for the sake of simplicity, all the velocities presented in this section are scalars and correspond to the x-component of the velocity profile, $v_x(y)$, generated by the simple-shear geometry described above; more specifically, the velocities are measured adjacent to the wall located at $y = +H/2$ and are therefore positive. A generalization of our models to arbitrary flows and geometries is provided in Subsection III D.

For a wall-shear flow the simplest definition of the slip velocity is the difference between the velocity U_{wall} of the wall itself and the translational velocity v_{w} of the particle layer immediately adjacent to the wall – that is,

$$v_{\text{slip}} \equiv U_{\text{wall}} - v_{\text{w}}, \tag{4}$$

This *translational slip velocity* has been commonly used in previous works, most notably in the model of Johnson and Jackson [12] that is frequently used in gas-solid two-fluid model

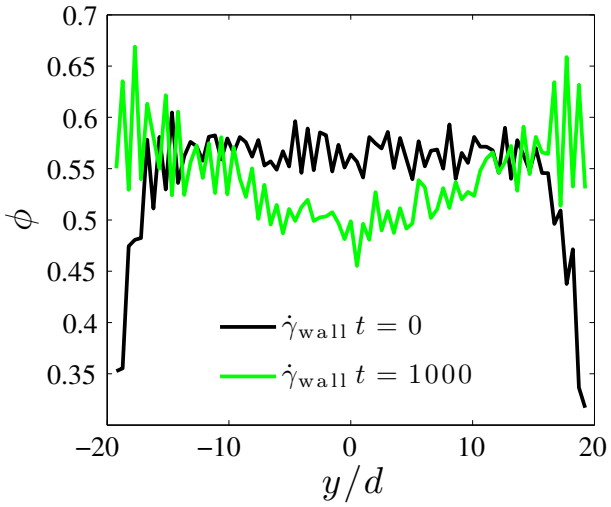

(a)

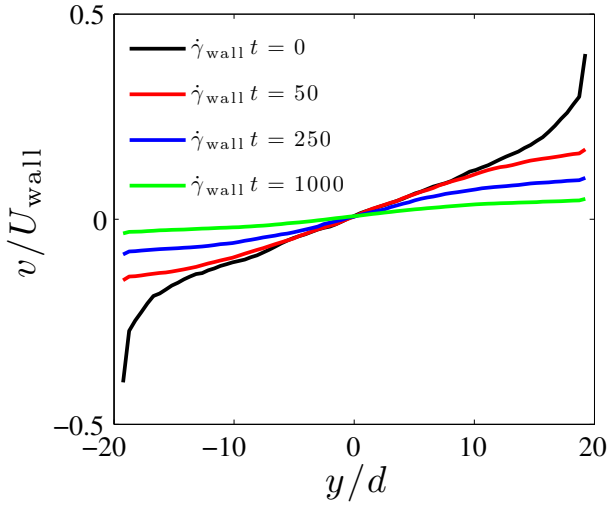

(b)

FIG. 3. Example case of shear localization when starting from a pre-sheared state for Hookean contact. The interparticle friction coefficient and wall-particle friction $\mu = \mu_w = 0.5$ and $\bar{\phi} = 0.55$. (a) A plot of volume fraction versus position reveals migration over time of particles away from the core and towards the walls, where they begin to show signs of ordering. (b) Velocity profiles at different shear times indicate progressive cooling of the assembly towards an isotropic state, with unsheared plugs growing over time at each wall.

simulations [36]. While this definition is straight-forward to use since all continuum models track the translational velocity of the solids, it does not include any rotational motion of the

particles at the wall. This exclusion is certainly significant, as a particle that rolls along a wall without slipping will nevertheless have a nonzero translational slip velocity. In fact, the best measure of true slip utilizes the velocity of the particles' surface that is in contact with the wall rather than the translational velocity of its center of mass. We define this *surface slip velocity* as

$$v_{\text{slip}}^{\text{surf}} \equiv U_{\text{wall}} - v_{\text{w}}^{\text{surf}}, \tag{5}$$

where the rotational velocity of the particles at the wall

$$v_{\text{w}}^{\text{rot}} \equiv \omega_{\text{w}} d/2 \tag{6}$$

is added to the particles' translational velocity to yield the velocity of the particles' surface

$$v_{\text{w}}^{\text{surf}} \equiv v_{\text{w}} + v_{\text{w}}^{\text{rot}}. \tag{7}$$

Here, ω_{w} is the angular velocity of the particles at the wall; for this flow geometry, only the z-component has a nonzero time-averaged value, which is positive at both walls. This surface slip velocity has been used recently in the works of Artoni *et al.* [19, 20] to describe slip behavior. While this definition is a better descriptor of slip behavior, its use in continuum modeling requires the tracking of the rotational motion of the solids phase, a level of complexity that is computationally more expensive and not commonly used. In both of the above definitions, though, the major computational cost comes from the need to resolve the boundary layer since both the translational and rotational velocities exhibit significant gradients within $\sim 10d$ of the wall – see Figure 1a. Hence, while not microscopically descriptive, it would be convenient to constitute a model for an 'effective' slip velocity based on a particle velocity extrapolated from the linear core profile to the wall. This *apparent solids velocity* v^{app} can be defined as

$$v_{\text{slip}}^{\text{app}} \equiv U_{\text{wall}} - v_{\text{w}}^{\text{app}}, \tag{8}$$

where the apparent solids velocity is

$$v_{\text{w}}^{\text{app}} \equiv \dot{\gamma}_{\text{core}} H/2, \tag{9}$$

and the difference between the apparent and translational velocities – which we term the *boundary-layer velocity contribution* – is

$$v_{\text{w}}' \equiv v_{\text{w}} - v_{\text{w}}^{\text{app}}. \tag{10}$$

TABLE I. Definitions of velocities and slip velocities, specified at the wall located at $y = H/2$.

Velocity	Definition	Meaning
U_{wall}		Velocity of the wall
v_w	$v(y = H/2)$	Translational velocity (of the solids) at the wall
v_w^{app}	$\dot{\gamma}_{\text{core}} H/2$	Translational velocity extrapolated to the wall
v_w'	$v_w - v_w^{\text{app}}$	Boundary-layer velocity contribution at the wall
v_w^{rot}	$\omega(y = H/2)d/2$	Rotational velocity at the wall (in the direction of U_{wall})
v_w^{surf}	$v_w + v_w^{\text{rot}}$	Velocity of the particle surfaces at the wall
v_{slip}	$U_{\text{wall}} - v_w$	Translational slip velocity
$v_{\text{slip}}^{\text{surf}}$	$U_{\text{wall}} - v_w^{\text{surf}}$	Surface slip velocity
$v_{\text{slip}}^{\text{app}}$	$U_{\text{wall}} - v_w^{\text{app}}$	Apparent slip velocity

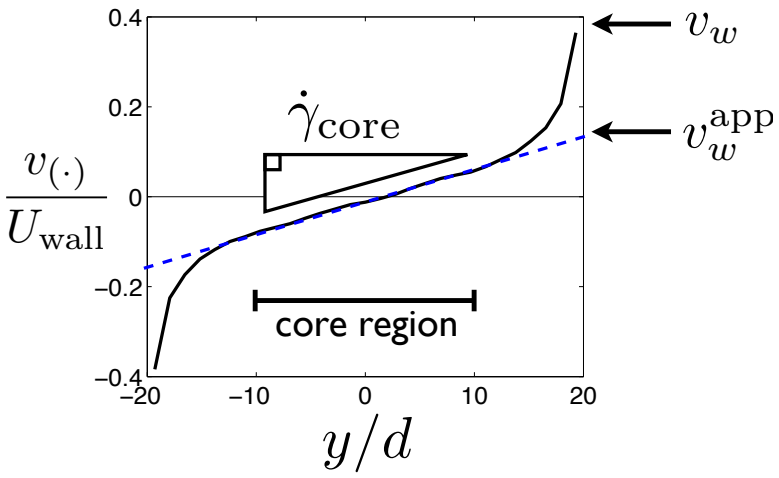

FIG. 4. Example velocity profile with the apparent wall velocity denoted.

These definitions are denoted on an example velocity profile in Figure 4. In this work, we aim to constitute models useable at all levels of resolution and complexity, and hence we investigate the amenability of all the slip velocities to scaling collapses.

Just as there are numerous slip velocities and velocity contributions, there are likewise several different options for scaling the velocities. We generally define the dimensionless slip velocity as

$$I_{\text{slip}}^{(\cdot)} = \frac{v_{\text{slip}}^{(\cdot)}}{v_{\text{char}}} \tag{11}$$

for some velocity scale v_{char}. Choices for v_{char}, which in general can be measured at the wall or in the core, include:

1. U_{wall}, simply the wall velocity;
2. $\dot{\gamma}d$, a shear-rate-based scale proposed by Artoni [20];
3. $\sqrt{p/\rho_s}$, a stress-based scale used by Artoni [19] and analogous to that in the inertial-number definition [7, 9]; and
4. $\nu/\rho_s d$ $(= \tau/\rho_s \dot{\gamma} d)$, a viscosity-based scale that seems not to have been considered in the prior literature.

The first of these options, U_{wall}, is an awkward choice for general flow problems since a BC with slip velocity scaled in this manner cannot be applied to a system with a stationary wall. Nevertheless, it is a useful reference velocity in this bounded shear flow example, in part because it is independent of particle and wall properties and the state of the particle assembly. We hence employ this scaling in Figure 5 to show the effect of μ, μ_w, and ϕ on surface slip velocity data. Here, an ordinate value of zero corresponds to a no-slip state while a value of unity corresponds to a full-slip state. Unsurprisingly, we observe that slip decreases as wall friction increases, with zero slip occurring as $\mu_w \to \infty$. There are also less straightforward dependences on μ and ϕ (or, equivalently, the distance to the jamming point $\phi_c - \phi$) that become clearer with the use of the other velocity scaling options.

Next we assess the ability of the suggested scalings of Artoni *et al.* [19, 20] to collapse the surface slip velocity data for an array of values of μ, μ_w, and ϕ. In Figure 6a, the shear-rate-based scaling is used, and the resulting dimensionless slip velocity is plotted versus η/μ_w — the quantity suggested in Refs. [19, 20] as the determinant of slip behavior. As seen in the figure, however, there is significant scatter for low values of η/μ_w, which correspond to volume fractions closest to ϕ_c. Additionally, for any given combination of friction coefficients, one can observe nonmonotonic behavior of the scaled slip velocity, which is in contrast to the behavior of the model proposed in Ref. [20]. We do note that, for the purpose of this scaling, Artoni *et al.* measure the shear rate at the wall, a task that is simple in their gravity-driven chute-flow simulations because of the rather small spatial dependence of $\dot{\gamma}$; in our shear-flow simulations, however, the shear rate varies sharply near the wall, making extrapolation of $\dot{\gamma}_{\text{w}}$ difficult. By contrast, the shear rate is constant in the core region of the shear flow and

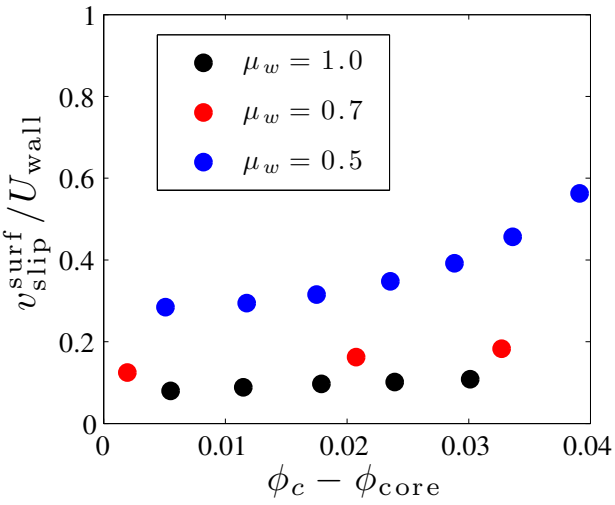

(a)

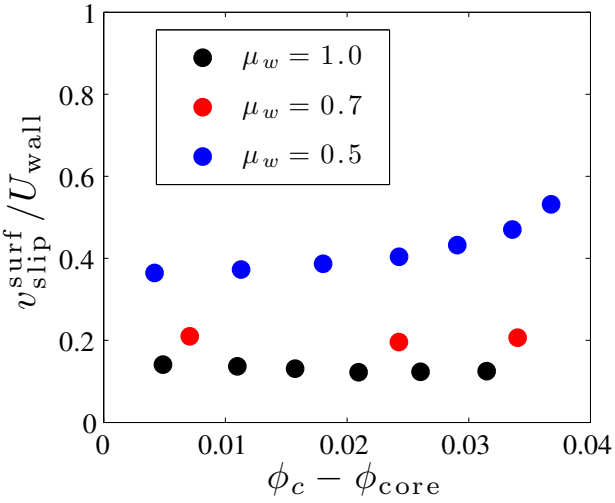

(b)

FIG. 5. Surface slip velocities, scaled by wall velocity, vs. $\phi_c - \phi$ for (a) $\mu = 0.5$ and (b) $\mu = 1.0$ for various μ_w. Slip is observed to increase with decreasing μ_w. Hookean contact is used.

thus is substantially easier to measure with confidence. We hence use $\dot{\gamma}_{\text{core}}$ as the basis for the scaling here while also noting that our use of estimated values of $\dot{\gamma}_{\text{w}}$ does not improve the ability of this scaling to collapse the data (results not shown).

With the limitations of the $\dot{\gamma}$-based scaling in mind, we then test the pressure-based scaling of Ref. [19] in Figure 6b and find that, while it resolves the issue of nonmonotonicity, it remains unable to collapse the various simulated cases in a satisfactory manner when paired with the same abscissa. If plotted against $\eta - \eta_s$ as in Figure 6c, however, the pressure

scaling somewhat collapses the data for different cases of μ and ϕ onto separate curves for each case of μ_w. There is also, though, a slight suggestion of a non-zero y-intercept in the data, which we find difficult and ultimately undesirable to constitute— no combination of η, η_s, μ_w, μ, ϕ, or ϕ_c in the ordinate or abscissa is found to remove this feature. For this reason as well as some persisting scatter, it appears that there is room for improvement, which we aim to address by changing the velocity scale.

Indeed, when the surface slip velocity is scaled using the viscosity-based scaling, *i.e.*

$$I_{\text{slip}}^{\text{surf}} \equiv \frac{v_{\text{slip}}^{\text{surf}}}{\nu_{\text{core}}/\rho_s d}, \tag{12}$$

the data similarly collapse to distinct curves for each case of μ_w, as seen in Figure 6d; the y-intercept is also pushed towards zero. The additional step of collapsing these distinct curves requires that the abscissa — chosen here as $\eta - \eta_s$ — be augmented with a dependence on the wall friction coefficient as is done in Figures 6a-b. With the abscissa written in the form $(\eta - \eta_s)/f(\mu_w)$, we find that the function

$$f(\mu_w) = \mu_w + \mu_w^* - \eta_s \tag{13}$$

produces the best collapse of the data, as demonstrated in Figure 7. The quantity $\mu_w^* = 0.33$, as aforementioned, represents the critical wall friction coefficient below which the moving walls are unable to overcome the internal friction of the granular layer and produce shear [22]. The robustness of this collapse is further tested for various cases of wall separation distance H and wall velocity U_{wall}; these data, shown in Figure 8, reveal the insensitivity of the collapse to system parameters. Finally, we generate an approximate fit to the collapsed data of

$$I_{\text{slip}}^{\text{surf}} = \frac{1.55 x^{2/3}}{(1-x)^{5.25}} \tag{14}$$

with

$$x \equiv \frac{\eta - \eta_s}{f(\mu_w)} \tag{15}$$

in order to produce a useable surface slip velocity model for finely-resolved simulations tracking rotational particle motion. Although the expressions for the Hookean and Hertzian contact models differ slightly, they both reveal that $I_{\text{slip}}^{\text{surf}}$ $I_{\text{slip}}^{\text{surf}}(x)$.

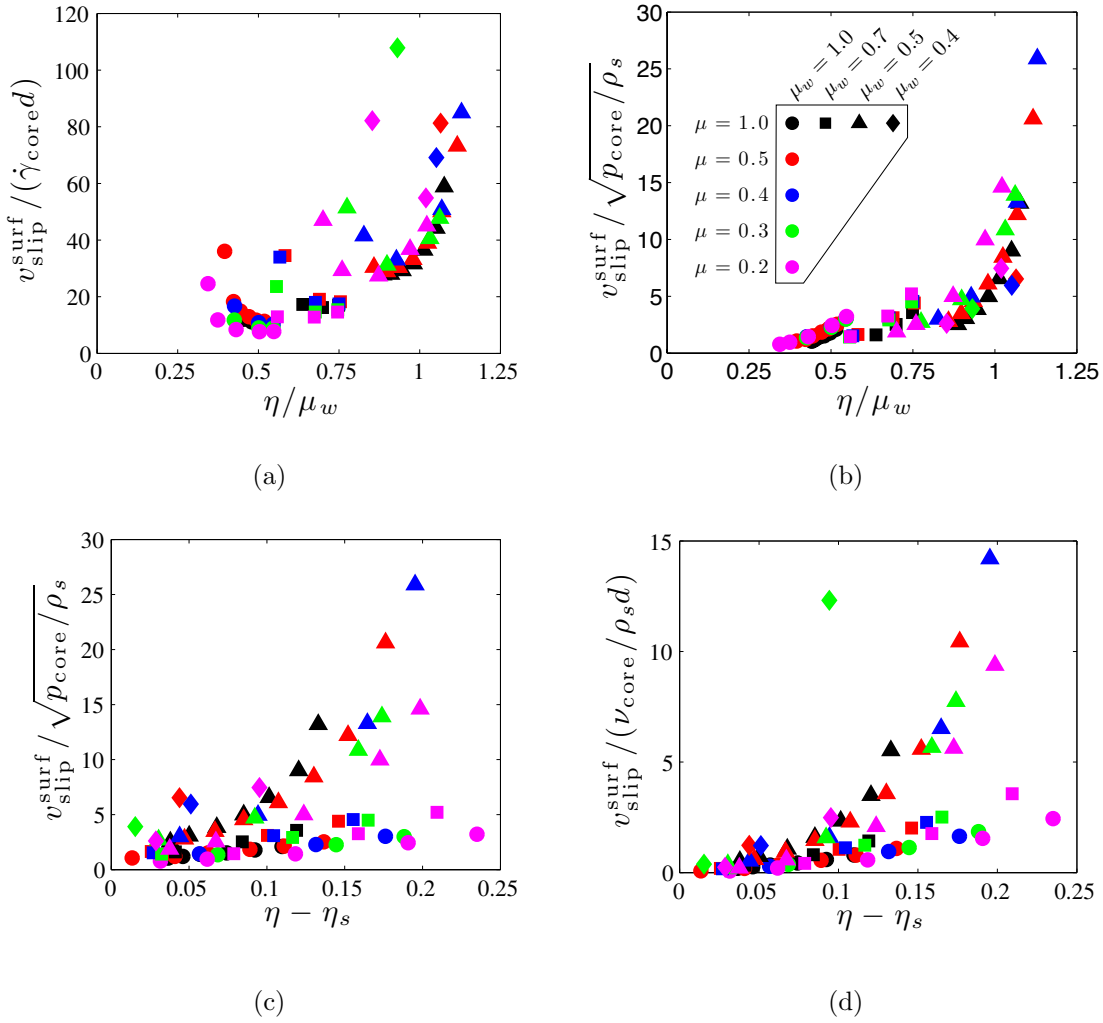

FIG. 6. Scaled surface slip velocity versus scaled shear stress ratio using velocity scales based on (a) core shear rate $\dot{\gamma}_{\text{core}}$, (b-c) pressure p, and (d) core viscosity ν_{core}. In (a) and (b), the abscissa is that used in Refs. [19, 20], and the slip data appear not to collapse as reported in those works. In (c), a new abscissa is used that somewhat collapses the data for different cases of μ and ϕ onto separate curves for each case of μ_w. However, there is a slight suggestion of a non-zero y-intercept in the data, which is undesirable to constitute. In (d), this new abscissa is paired with a new velocity scaling, which reduces the scatter of the previous scaling and pushes the y-intercept to zero. The further collapsing of μ_w cases is performed in Figure 7.

The BC model in Eq. 14 can be applied to continuum modeling of shear flow problems in which both translation and rotational velocity fields are solved with sufficient resolution to capture the boundary layer. In such an application, it is clear that the values of v_{w} and ω_{w} should be measured at the wall. The location for measurement of ν_{core}, though, is to

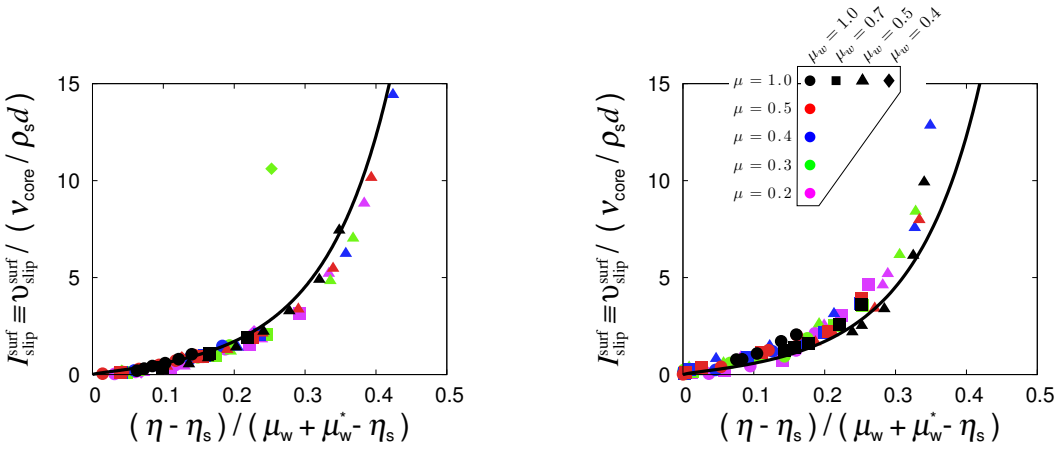

(a) (b)

FIG. 7. Viscosity-scaled surface slip velocity versus scaled shear stress ratio. Panels (a) and (b) are for Hookean and Hertzian contact models, respectively. The solid lines correspond to equation 14. The scalings produce a collapse of the data for different cases of μ_w, μ, and ϕ.

some extent a choice of the modeler; the only requirement is that it be measured outside the boundary layer, *i.e* at least $10d$ away from the wall. This question is discussed in more detail in Section III D.

C. Extension of BC model to problems with coarse resolution and/or considering only translational motion

Though Eq. 14 can predict the surface slip velocity over a wide range of dense flow scenarios, it will lose accuracy in continuum simulations that are coarsely resolved or that do not track the angular velocity of the granular material – scenarios that constitute the vast majority of practical granular and multiphase simulation efforts. Hence, we turn our attention to extending the BC model for application to these cases.

The strategy employed here for this extension is to constitute the unknown quantities representing rotational velocity and boundary-layer velocity contribution in terms of known, core quantities. We begin by applying the same viscosity-based scaling used earlier to define

$$I_{\text{rot}} \equiv \frac{v_w^{\text{rot}}}{\nu_{\text{core}}/\rho_s d} \tag{16}$$

and

$$I' \equiv \frac{v'_w}{\nu_{\text{core}}/\rho_s d}. \tag{17}$$

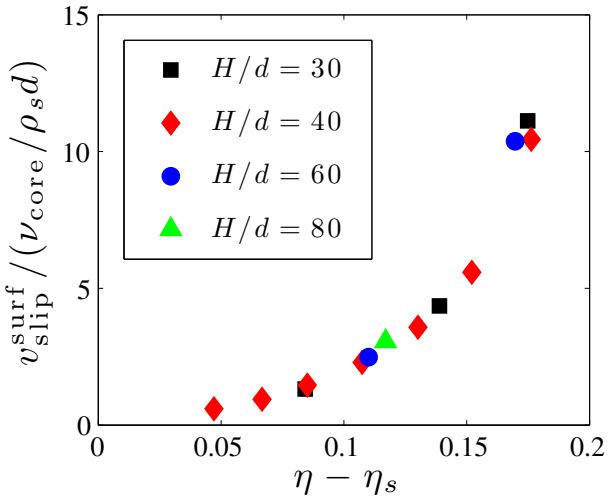

(a)

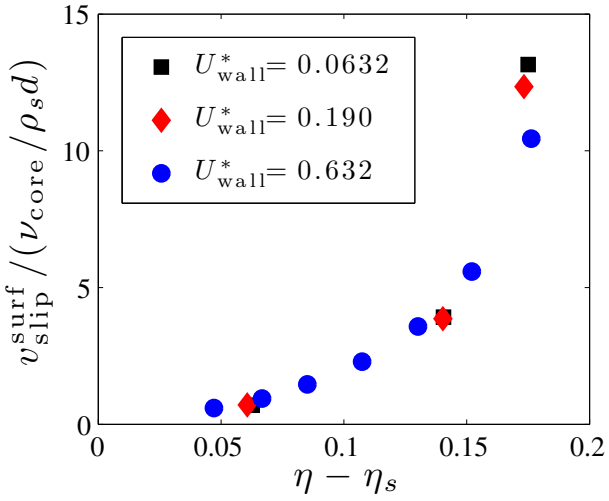

(b)

FIG. 8. Viscosity-scaled surface slip velocity versus scaled shear stress ratio for various dimensionless values of (a) wall spacing and (b) wall velocity with $\mu = \mu_w = 0.5$. The scaled wall velocity is defined here as $U^*_{\rm wall} \equiv U_{\rm wall}/\sqrt{k/\rho_s d}$. The collapse afforded by the slip velocity scaling is robust to changes in these system parameters.

Next, we note that both $v^{\rm rot}$ and v' are essentially zero in the core but become significant in the near-wall region [34], as seen in Figure 4 and Figure 1a. Indeed, their similar near-wall gradients suggest the possibility of a simple relationship between the two, which is confirmed by the plotting $I_{\rm rot}$ versus I' in Figure 9a. Results are shown for Hookean contact model.

Analogous results were obtained for Hertzian contact model as well (not shown). Here, we observe an approximately linear relationship that is independent of the chosen velocity scaling and whose slope depends primarily on μ. This μ dependence appears to be nearly exponential in a manner similar to the variation of η_s with μ. We are hence able to collapse the data from Figure 9a to a single curve, seen in Figure 9c for Hookean contact model, by scaling the abscissa by the quantity $\eta_s(\mu) - \eta_{s0}$, where $\eta_{s0} = \eta_s(\mu = 0)$; values of η_s can be obtained from simulation data [9] or calculated from the fitted function [33]

$$\eta_s = \eta_{s0} + (\eta_{s\infty} - \eta_{s0})g(\mu), \tag{18}$$

where $\eta_{s0} = 0.105$, $\eta_{s\infty} = \eta_s(\mu = \infty) = 0.405$, and $g(\mu)$ is defined as

$$g(\mu) = 1 - \exp(-6\mu). \tag{19}$$

We can then relate the scaled velocities by

$$I_{\text{rot}} = mI' \tag{20}$$

with

$$m = \frac{(\eta_{s\infty} - \eta_{s0})^2}{(\eta_s(\mu) - \eta_{s0})^2} \tag{21}$$

$$= \frac{1}{g^2(\mu)}. \tag{22}$$

Figures 9b and 9d are analogous to Figures 9a and 9c, respectively, but are for Hertzian contact model. The same expresion for $g(\mu)$ is used for both contact models. The Hertzian model shows a greater scatter. Finally, we write the translational slip velocity in dimensionless form as

$$I_{\text{slip}} = \frac{v_{\text{slip}}}{\nu_{\text{core}}/\rho_s d}, \tag{23}$$

and constitute it as

$$I_{\text{slip}} = I_{\text{slip}}^{\text{surf}} + I_{\text{rot}}, \tag{24}$$

with $I_{\text{slip}}^{\text{surf}}$ given by Eq. 14 and I_{rot} given by Eq. 20.

Functionally, Eq. 20 augments the $I_{\text{slip}}^{\text{surf}}$ model in Eq. 14 to create a BC model applicable to continuum-modeling problems without explicit solution of the angular velocity field,

provided the apparent velocity of the particles at the wall is known. In a general flow problem, the apparent velocity of the particles at the wall is not known, but in this simple test problem, it is simply equal to $\dot{\gamma}_{\text{core}}H/2$. As a result, we can write $v' = v_{\text{w}} - \dot{\gamma}_{\text{core}}H/2$. Equations 14, 20, 24 and 25 then allow estimation of v_w. For a more complex flow problem, the apparent velocity of the particles at the wall is not known and so an additional equation should be formulated. For such cases, the near-wall angular velocity is algebraically related to the near-wall boundary-layer velocity contribution v', which can be extracted from the translational velocity field provided it is solved with sufficient resolution to capture the $\sim 10d$-thick boundary layer. Specifically, we apply Eqs. 9-10 to obtain

$$v' = v_{\text{w}} - \dot{\gamma}_{\text{core}}H/2, \tag{25}$$

which is easily evaluated since the right-hand side contains known quantities. As aforementioned, for shear flows $\dot{\gamma}_{\text{core}}$ can be measured at any chosen location in the core.

In a similar fashion, we constitute I' in order to eliminate the need for boundary layer resolution. The boundary contribution to the translational velocity is again observed to depend on the distance to the jamming point as well as particle and wall friction coefficients; as with $I^{\text{surf}}_{\text{slip}}$, there is also a dependence on the restitution coefficient. These dependences are seen in Figure 10a for Hookean contact model. By approximating the relationship between I' and $\eta - \eta_s$ as linear, we calculate a slope for each case and fit the slope data to the form of

$$m' = 23.4\,(1 - e^2_{\text{eff}})\,\text{Arctan}\left[6\left(\frac{\mu_w}{\eta_s} - 1\right)\right]. \tag{26}$$

Here, e_{eff} is the effective restitution coefficient [11], which empirically describes the collisional loss of translational velocity resulting from inelasticity and friction as

$$e_{\text{eff}} = e - \frac{3}{2}\mu \exp(-3\mu). \tag{27}$$

We then obtain (see Figure 9c)

$$I' = m'(\eta - \eta_s) \tag{28}$$

Figures 9b and 9d illustrate that the same approach applies for the Hertzian contact model. Armed with these simple correlations, one can write down the boundary conditions for the simple 1-D flow problem as follows:

$$I^{\text{app}}_{\text{slip}} \equiv \frac{v^{\text{app}}_{\text{slip}}}{\nu_{\text{core}}/\rho_s d}, \tag{29}$$

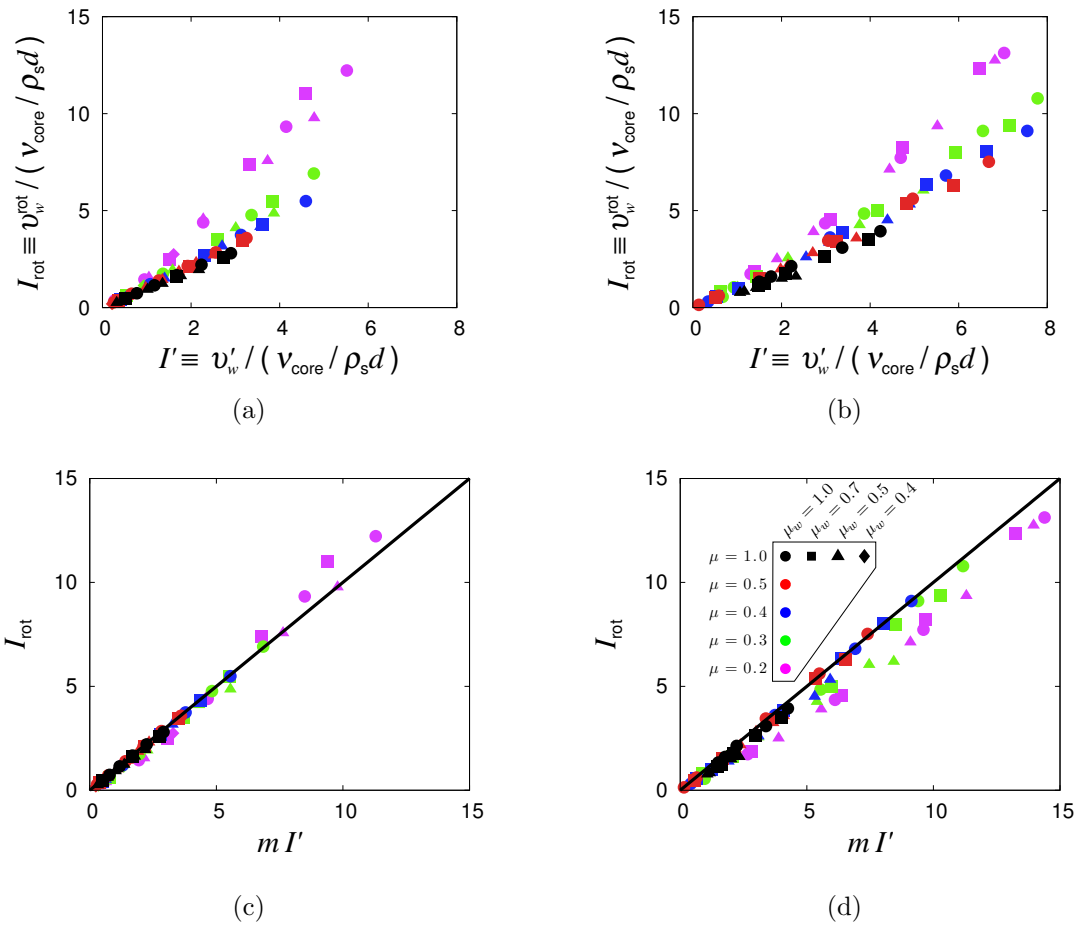

FIG. 9. Scaled rotational velocity vs. scaled boundary-layer velocity contribution (a) without and (b) with the prefactor m on the abscissa; m is defined in Eq. 22. A linear relationship between the two exists for all cases considered, regardless of how the velocities are nondimensionalized.

when one can calculate the apparent slip velocity, defined as

$$I_{\rm slip}^{\rm app} = I_{\rm slip}^{\rm surf} + I_{\rm rot} + I' \tag{30}$$

$$= I_{\rm slip} + I'. \tag{31}$$

D. Generalized BC model

Though the model expressions presented above are developed on the basis of simple-shear simulation results, they can be easily recast to handle general flow problems. To this end, we begin by rewriting all the aforementioned velocities in vectorial form. The surface slip

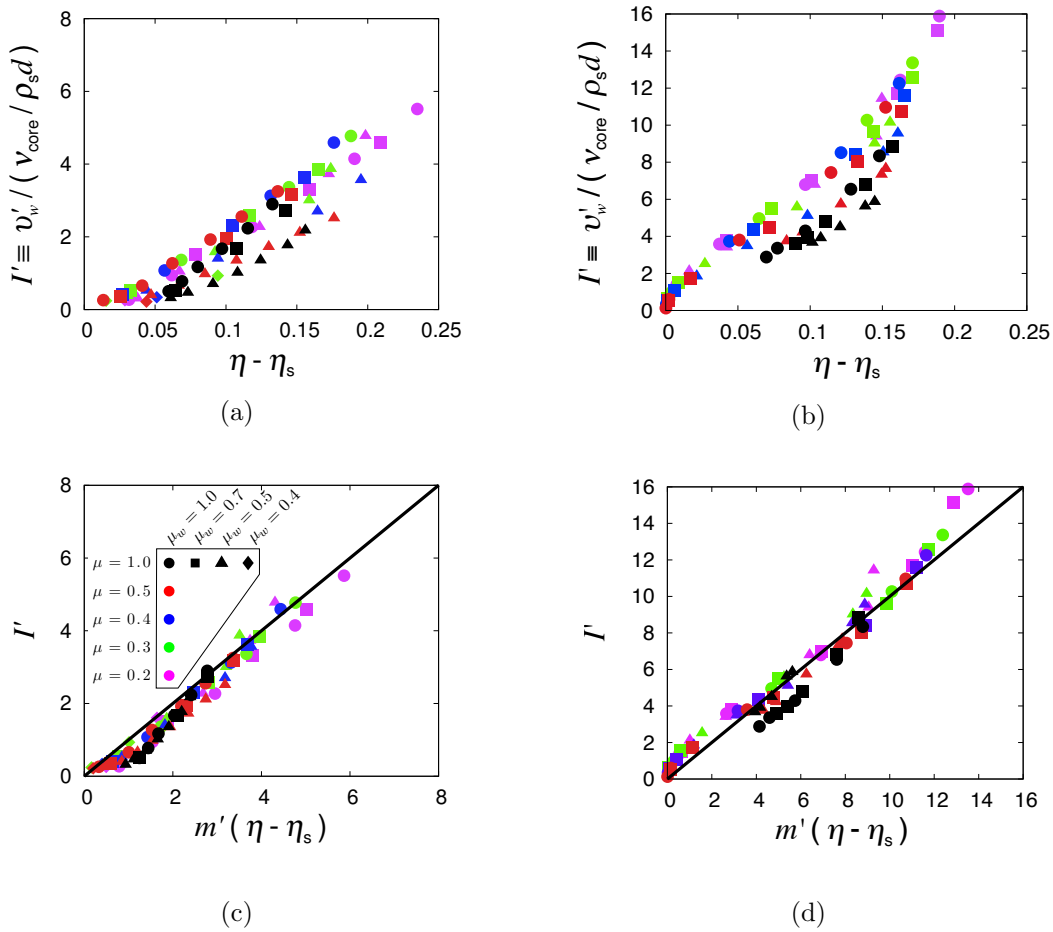

FIG. 10. Scaled boundary-layer velocity contribution vs. scaled shear stress ratio (a) without and (b) with the prefactor m' on the abscissa. The prefactor is defined in Eq. 26.

velocity can thus be written as

$$\mathbf{v}_{\text{slip}}^{\text{surf}} \equiv \mathbf{U}_{\text{wall}} - \mathbf{v}_{\text{w}}^{\text{surf}}, \tag{32}$$

with

$$\mathbf{v}_{\text{w}}^{\text{surf}} \equiv \mathbf{v}_{\text{w}} + \mathbf{v}_{\text{w}}^{\text{rot}} \tag{33}$$

and

$$\mathbf{v}_{\text{w}}^{\text{rot}} \equiv \left(\frac{d}{2}\right) \boldsymbol{\omega}_{\text{w}} \times \mathbf{n}. \tag{34}$$

Here, $\mathbf{n}$ is the unit normal vector from the particle center to the wall. We then note that, in the simple-shear example above, the scalar slip velocity is simply the magnitude of the slip velocity vector — that is,

$$v_{\text{slip}}^{\text{surf}} \equiv |\mathbf{v}_{\text{slip}}^{\text{surf}}|. \tag{35}$$

We can then continue to define $I_{\text{slip}}^{\text{surf}}$ as in Eq. 12 and constitute it as in Eq. 14. In similar fashion, we can write

$$\mathbf{v}_{\text{slip}} \equiv \mathbf{U}_{\text{wall}} - \mathbf{v}_{\text{w}}, \tag{36}$$

and

$$v_{\text{slip}} \equiv |\mathbf{v}_{\text{slip}}|, \tag{37}$$

define I_{slip} as in Eq. 25 and constitute it with Eqs. 24, 20, and 28. Finally, we write

$$\mathbf{v}_{\text{slip}}^{\text{app}} \equiv \mathbf{U}_{\text{wall}} - \mathbf{v}_{\text{w}}^{\text{app}} \tag{38}$$

and

$$v_{\text{slip}}^{\text{app}} \equiv |\mathbf{v}_{\text{slip}}^{\text{app}}|, \tag{39}$$

with $I_{\text{slip}}^{\text{app}}$ defined in Eq. 29 and constituted in Eqs. 31, 20, and 28.

In addition to the velocities, we must also generalize the definition of the viscosity in the core. This definition is trivial in the case of a shear flow since the rough location of the core is known prior to solving for the flow fields and since the core features spatially-invariant rheological properties. These features ensure that the BC model will be unaffected by the choice of ν_{core} so long as it is measured at a location that is beyond $10d$ of the walls. However, the definition of a core viscosity becomes less clear in general flow scenarios, where the viscosity (and shear rate and volume fraction) may vary with position throughout the domain. One can reason, though, that the core viscosity succeeds in collapsing slip velocity data in our shear flow simulations because of the proximity of the core to the wall; that is, the core influences the wall behavior because the two regions are separated by only $10d$. This observation motivates us to recommend measuring the core viscosity at a distance of $10d$ from the wall, *i.e.*

$$\nu_{\text{core}} \equiv \nu(\mathbf{x} = \mathbf{x}_{\text{wall}} + (10d)\mathbf{n}), \tag{40}$$

where $\mathbf{x}_{\text{wall}}$ is the local position of the wall. If the computational mesh is sufficiently coarse, though, the first grid cell may lie further than $10d$ from the wall, so viscosity information would be unavailable at the desired distance from the wall. In such a scenario, the viscosity can instead be taken at the first interior grid cell. This position ensures measurement of rheological information relevant to the slip behavior while still characterizing core (*i.e.* local) rheology.

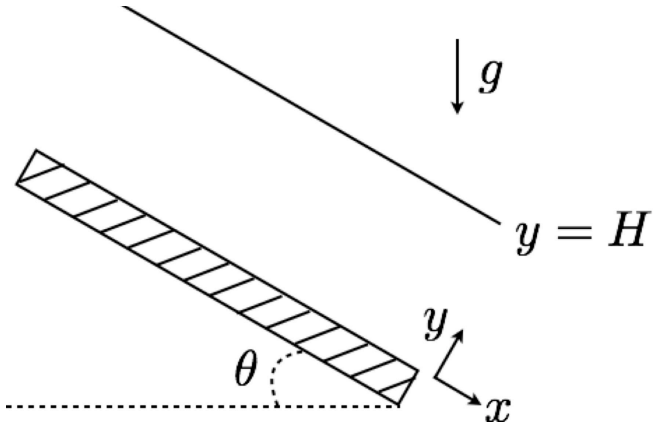

FIG. 11. Inclined-plane geometry used in the example application of the BC model.

E. Example application of BC model

To clarify how to use the BC model, we apply it to the 1-dimensional problem of dense granular flow down an inclined plane, the geometry for which is shown in Figure 11. Balance equations on momentum yield expressions for the stress gradients; specifically,

$$\frac{d\tau}{dy} = -\rho_s \phi g \sin(\theta) \tag{41}$$

and

$$\frac{dp}{dy} = -\rho_s \phi g \cos(\theta), \tag{42}$$

where y is the distance from the base, θ is the inclination angle, and g is the gravitational acceleration. If we specify a simple, algebraic rheological model, *e.g.* an inertial-number model [7, 9], p and τ become explicit functions of ϕ and $\dot{\gamma}$, thereby converting Eqs. 41-42 to a system of two ordinary differential equations for the dependent variables ϕ and $\dot{\gamma}$. The

latter of these is, of course, tied to the velocity field via

$$\frac{dv_x}{dy} = \dot{\gamma}. \tag{43}$$

If the height H of the granular layer is large, it becomes computationally quicker to model the boundary layer rather than resolve it; assuming this scenario, the velocity field near the wall is in fact the *apparent* velocity. Hence, our boundary condition at the bottom wall is, as per Eq. 31,

$$I^{\text{app}}_{\text{slip}} = I^{\text{surf}}_{\text{slip}} + I' + I^{\text{rot}} \tag{44}$$

$$= I^{\text{surf}}_{\text{slip}} + (1+m)I'. \tag{45}$$

Substituting Eqs. 14-15 and Eq. 28 into Eq. 45, we see that the right-hand side is a function of η, which we rewrite as

$$I^{\text{app}}_{\text{slip}} = F(\eta(y=0)). \tag{46}$$

Next, we substitute Eqs. 38-40 into Eq. 46 and, noting that $\mathbf{U}_{\text{wall}} = \mathbf{0}$ for this problem, we obtain

$$\frac{|\mathbf{v}^{\text{app}}_w|}{\nu_{\text{core}}/\rho_s d} = F(\eta(y=0)). \tag{47}$$

Since the boundary layer is not being resolved, $\mathbf{v}^{\text{app}}_w = \mathbf{v}_w$ as mentioned before; also, $\nu_{\text{core}} = \nu(y=0)$. Therefore, the final BC expression becomes

$$v_x(y=0) = \frac{\nu(y=0)}{\rho_s d} F(\eta(y=0)). \tag{48}$$

Expressions for η and ν in terms of ϕ and $\dot{\gamma}$ are provided by the rheological model since $\eta \equiv \tau/p$ and $\nu \equiv \tau/\dot{\gamma}$. Once a boundary condition is placed at the free surface, such as the zero-shear-stress condition

$$\tau(y=H) = 0, \tag{49}$$

the boundary value problem becomes fully specified and can be solved numerically.

IV. DISCUSSION

The constitutive equations presented in the previous section allow for the prediction of the slip velocity in finely- or coarsely-resolved solution of continuum models that either include

TABLE II. Summary of model equations.

Equation	Description
$I_{\text{slip}}^{\text{surf}} = \frac{\eta-\eta_s}{\mu_w+\mu_w^*-\eta_s}$	Surface slip velocity
$I_{\text{slip}} = I_{\text{slip}}^{\text{surf}} + I_{\text{rot}}$	Translational slip velocity
$I_{\text{slip}}^{\text{app}} = I_{\text{slip}} + I'$	Apparent translational slip velocity
$I_{\text{rot}} = mI'$	Rotational velocity at the wall
$I' = m'(\eta - \eta_s)$	Boundary-layer velocity contribution at the wall

or neglect the angular velocity field. The BC expressions contain explicit dependencies on numerous important particle and wall parameters, including (1) microscopic parameters such as the particle-particle friction coefficient μ, particle-wall friction coefficient μ_w, and the particle restitution coefficient e, as well as (2) continuum parameters that depend on the microscopic parameters such as the yield stress ratio η_s and the effective restitution coefficient e_{eff}. These aspects — flexibility and range of application — are the primary strengths of the presented model.

Another notable feature of the model is the viscosity-based characteristic velocity $v_{\text{char}} = \nu_{\text{core}}/\rho_s d$ that is used to scale the slip velocities and velocity contributions. Previous BC models have cast the slip velocity as being proportional to a characteristic shear velocity $\dot{\gamma}d$ [20], a characteristic particle rearrangement velocity $\sqrt{p/\rho_s}$ [19], or a characteristic fluctuating velocity $\sqrt{T}$ [12]. Each of these has its advantages and disadvantages. The quantity $\dot{\gamma}d$ is a valid velocity scale for all flow problems but does not contain any explicit dependences on volume fraction, which appear to be necessary to eliminate the nonmonotonicity of the scaled slip velocity observed in Figure 6a; the ϕ-dependence must therefore be constituted in the model prefactors — a task that is certainly possible but may be tedious for a large parameter space (*i.e.* ϕ, μ, e, *etc.*). The pressure-based scale introduces such a ϕ-dependence, albeit in a way that is not conducive to a general collapse (as far as we could identify); this scale is also not a useful velocity scale in quasistatic flows [20], where pressure becomes independent of shear rate [9]. Finally, the temperature-based scaling, in a continuum-modeling context, not only requires the solution of a balance equation for the fluctuation energy but moreover requires that this energy balance model be representative of the physics of dense

flows; most models for T are based on kinetic theory and have been designed for flows in which $\phi \lesssim 0.5$ (with some exceptions [11, 18, 37]). The viscosity-based scaling, therefore, combines several of the benefits of the other scales but without their drawbacks.

On the other hand, the presented model has a number of weaknesses, perhaps the largest of which is the heavy reliance on empiricism. Indeed, not only the fitting constants but even the functional forms of some of the model equations may appear difficult to justify from a purely microscopic, physical basis. To some extent, this empiricism is a product of the large parameter space considered in this work; the range of ϕ, μ, μ_w, and e studied in our simulations requires substantial effort to find common functional dependences. The kinetic-theory framework has proven useful in past investigations of rheological [5, 6] and slip behavior [14, 15] of inelastic, frictional/rough particles, producing explicit dependences on these same parameters. However, the assumptions typically made when utilizing the kinetic-theory approach can limit the range of applicability of the derived constitutive equations. Most importantly, the assumption of molecular chaos limits the model validity to volume fractions less than about 0.5, outside the dense regime of interest here. The use of kinetic theory along with velocity distribution data from dense-regime simulations, an approach taken by Kumaran [18], could reduce the need for empiricism, though it is not clear that this approach would produce closed-form expressions for the stresses as needed for practical continuum-modeling work. Hence, the approach we propose here is an interim solution until models firmly grounded on underlying physics are rigorously derived. Despite the empirical strategy, many of the model parameters, though fitted from simulation data, have direct or approximate physical meanings. For example, η_s is the yield stress ratio for the particle assembly, while $\eta - \eta_s$ is the distance to the yield stress ratio. The effective restitution coefficient e_{eff} appears in terms of $1 - e_{\text{eff}}^2$, which is an approximate measure of the collisional loss of kinetic energy due to the combined effects of inelasticity and friction [11]. The term μ_w^* represents approximately the minimum required amount of wall friction to sustain shear, and its value of 0.33 is, perhaps not by pure coincidence, also the value of μ at which e_{eff} is minimized, suggesting a possible microscopic reason for the failure to thermalize the particle assembly when $\mu_w = \mu_w^*$. While a more sound theoretical basis for the BC model is certainly desirable, the model presented here provides usable expressions for the slip velocity while also providing clues as to the possible forms and scalings that a detailed theoretical treatment might produce.

Finally, the BC model does not adequately address cases of unsteady particle cooling. As mentioned in Section III A, in some simulated cases the dissipation of granular energy is too high at the walls to allow sustained shear to occur. While we do observe an approximate regime boundary between shearing and non-shearing cases at a critical value of μ_w as did Shojaaee *et al.* [22], we do not conduct a thorough investigation of the nature of this transition. The reason for limiting our analysis to steady systems is the difficulty in obtaining meaningful measurements of continuum field variables that vary both in space and time while maintaining high spatial and temporal resolution. In the case of our steady simulations, high spatial resolution is facilitated by time-averaging over long simulation times; this approach is impeded if the dependence on time is also to be measured. Moreover, the resolution in time and space cannot be improved by increasing the system size, as the field variables of interest in the shear flow vary over distances of $\sim 10d$, a distance that is independent of the number of particles being considered. Overcoming these challenges to produce a dynamic BC model would represent a substantial, standalone effort and is therefore outside the scope of the present study.

V. SUMMARY

Solution of granular flow problems by continuum methods requires specification of wall boundary conditions, expressions for which have not been fully established for dense flow scenarios. Additionally, continuum methods are limited in the case of most practical flow problems by the need for (1) coarse resolution of the flow field and (2) simple flow models that consider only translational motion, as both of these choices reduce computational cost. On the basis of DEM simulations for a wide array of particle and wall properties, we propose a constitutive expression for the slip velocity for use in finely-resolved continuum simulations tracking particle rotation. We then constitute additional terms that, when added to this slip velocity model, extend its validity to coarsely-resolved, translation-only flow descriptions. The presented model hence offers flexibility to the modeler in regard to the level of resolved detail while reducing the loss of accuracy, thereby allowing for improved flow predictions

across a wide range of practical flow problems.

---

[1] V. Garzó and J. W. Dufty, "Dense fluid transport for inelastic hard spheres," *Phys. Rev. E*, vol. 59, pp. 5895–5911, May 1999.

[2] C. K. K. Lun, S. B. Savage, D. J. Jeffrey, and N. Chepurniy, "Kinetic theories for granular flow: inelastic particles in couette flow and slightly inelastic particles in a general flowfield," *J. Fluid Mech.*, vol. 140, pp. 223–256, 1984.

[3] J. T. Jenkins and M. W. Richman, "Kinetic theory for plane flows of a dense gas of identical, rough, inelastic, circular disks," *Phys. Fluids*, vol. 28, no. 12, pp. 3485–3494, 1985.

[4] J. T. Jenkins and S. B. Savage, "A theory for the rapid flow of identical, smooth, nearly elastic, spherical particles," *Journal of Fluid Mechanics*, vol. 130, pp. 187–202, 1983.

[5] C. K. K. Lun, "Kinetic theory for granular flow of dense, slightly inelastic, slightly rough spheres," *Journal of Fluid Mechanics*, vol. 233, pp. 539–559, 11 1991.

[6] V. Kumaran, "The constitutive relation for the granular flow of rough particles, and its application to the flow down an inclined plane," *Journal of Fluid Mechanics*, vol. 561, pp. 1–42, 7 2006.

[7] F. da Cruz, S. Emam, M. Prochnow, J.-N. Roux, and F. Chevoir, "Rheophysics of dense granular materials: Discrete simulation of plane shear flows," *Phys. Rev. E*, vol. 72, p. 021309, Aug 2005.

[8] P. Jop, Y. Forterre, and O. Pouliquen, "A constitutive law for dense granular flows," *Nature*, vol. 441, pp. 727–730, 06 2006.

[9] S. Chialvo, J. Sun, and S. Sundaresan, "Bridging the rheology of granular flows in three regimes," *Phys. Rev. E*, vol. 85, p. 021305, Feb 2012.

[10] S. Schneiderbauer, A. Aigner, and S. Pirker, "A comprehensive frictional-kinetic model for gas–particle flows: Analysis of fluidized and moving bed regimes," *Chemical Engineering Science*, vol. 80, no. 0, pp. 279 – 292, 2012.

[11] S. Chialvo and S. Sundaresan, "A modified kinetic theory for frictional granular flows in dense and dilute regimes," *Physics of Fluids*, vol. 25, no. 7, 2013.

[12] P. C. Johnson and R. Jackson, "Frictional-collisional constitutive relations for granular materials, with application to plane shearing," *J. Fluid Mech.*, vol. 176, pp. 67–93, 1987.

[13] J. T. Jenkins and M. W. Richman, "Boundary conditions for plane flows of smooth, nearly elastic, circular disks," *Journal of Fluid Mechanics*, vol. 171, pp. 53–69, 10 1986.

[14] J. T. Jenkins, "Boundary conditions for rapid granular flow: Flat, frictional walls," *J. Appl. Mech.*, vol. 59, no. 1, pp. 120–127, 1992.

[15] J. T. Jenkins and M. Y. Louge, "On the flux of fluctuation energy in a collisional grain flow at a flat, frictional wall," *Physics of Fluids*, vol. 9, no. 10, pp. 2835–2840, 1997.

[16] S. Schneiderbauer, D. Schellander, A. Löderer, and S. Pirker, "Non-steady state boundary conditions for collisional granular flows at flat frictional moving walls," *International Journal of Multiphase Flow*, vol. 43, no. 0, pp. 149 – 156, 2012.

[17] P. R. Nott, "Boundary conditions at a rigid wall for rough granular gases," *Journal of Fluid Mechanics*, vol. 678, pp. 179–202, 7 2011.

[18] V. Kumaran, "Dynamics of dense sheared granular flows. part ii. the relative velocity distributions," *Journal of Fluid Mechanics*, vol. 632, pp. 145–198, 2009.

[19] R. Artoni, A. Santomaso, and P. Canu, "Effective boundary conditions for dense granular flows," *Phys. Rev. E*, vol. 79, p. 031304, Mar 2009.

[20] R. Artoni, A. C. Santomaso, M. Go', and P. Canu, "Scaling laws for the slip velocity in dense granular flows," *Phys. Rev. Lett.*, vol. 108, p. 238002, Jun 2012.

[21] Z. Shojaaee, J.-N. Roux, F. m. c. Chevoir, and D. E. Wolf, "Shear flow of dense granular materials near smooth walls. i. shear localization and constitutive laws in the boundary region," *Physical Review E*, vol. 86, p. 011301, Jul 2012.

[22] Z. Shojaaee, L. Brendel, J. Török, and D. E. Wolf, "Shear flow of dense granular materials near smooth walls. ii. block formation and suppression of slip by rolling friction," *Physical Review E*, vol. 86, p. 011302, Jul 2012.

[23] GDR MiDi, "On dense granular flows," *Eur. Phys. J. E*, vol. 14, pp. 341–365, 2004. 10.1140/epje/i2003-10153-0.

[24] K. Kamrin and G. Koval, "Nonlocal constitutive relation for steady granular flow," *Phys. Rev. Lett.*, vol. 108, p. 178301, Apr 2012.

[25] D. Volfson, L. S. Tsimring, and I. S. Aranson, "Partially fluidized shear granular flows: Continuum theory and molecular dynamics simulations," *Phys. Rev. E*, vol. 68, p. 021301, Aug 2003.

[26] V. Vidyapati and S. Subramaniam, "Granular rheology and phase transition: Dem simulations and order-parameter based constitutive model," *Chemical Engineering Science*, vol. 72, no. 0, pp. 20 – 34, 2012.

[27] B. G. M. van Wachem, J. C. Schouten, C. M. van den Bleek, R. Krishna, and J. L. Sinclair, "Comparative analysis of cfd models of dense gas–solid systems," *AIChE Journal*, vol. 47, no. 5, pp. 1035–1051, 2001.

[28] M. Syamlal, W. Rogers, and T. J. O'Brien, "Mfix documentation: Theory guide," tech. rep., U.S. Department of Energy, 1993.

[29] P. A. Cundall and O. D. L. Strack, "A discrete numerical model for granular assemblies," *Geotechnique*, vol. 29, no. 1, pp. 47–65, 1979. ISI Document Delivery No.: GP775 Times Cited: 2094 Cited Reference Count: 14.

[30] S. Plimpton, "Fast parallel algorithms for short-range molecular dynamics," *J. Comput. Phys.*, vol. 117, no. 1, pp. 1–19, 1995. 0021-9991 doi: DOI: 10.1006/jcph.1995.1039.

[31] C. Kloss, C. Goniva, A. Hager, S. Amberger, and S. Pirker, "Models, algorithms and validation for opensource dem and cfd–dem," *Progress in Computational Fluid Dynamics, an International Journal*, vol. 12, no. 2-3, pp. 140–152, 2012.

[32] S. Savage and R. Dai, "Studies of granular shear flows wall slip velocities, 'layering' and self-diffusion," *Mechanics of Materials*, vol. 16, no. 1–2, pp. 225 – 238, 1993.

[33] J. Sun and S. Sundaresan, "A constitutive model with microstructure evolution for flow of rate-independent granular materials," *Journal of Fluid Mechanics*, vol. 682, pp. 590–616, 2011.

[34] C. S. Campbell, "Boundary interactions for two-dimensional granular flows. part 1. flat boundaries, asymmetric stresses and couple stresses," *Journal of Fluid Mechanics*, vol. 247, pp. 111–136, 2 1993.

[35] Y. Gu, S. Chialvo, and S. Sundaresan, "Rheology of cohesive granular materials across multiple dense-flow regimes," *Physical Review E*, vol. 90, no. 3, p. 032206, 2014.

[36] T. Li and S. Benyahia, "Revisiting johnson and jackson boundary conditions for granular flows," *AIChE Journal*, vol. 58, no. 7, pp. 2058–2068, 2012.

[37] J. Jenkins and D. Berzi, "Dense inclined flows of inelastic spheres: tests of an extension of kinetic theory," *Granular Matter*, vol. 12, no. 2, pp. 151–158, 2010.

12 Appendix D

Please see the next page for the manuscript "Rheology of cohesive granular materials across multiple dense-flow regimes," which was published in *Physical Review E*.

Rheology of cohesive granular materials across multiple dense-flow regimes

Yile Gu, Sebastian Chialvo, and Sankaran Sundaresan
Chemical and Biological Engineering Department, Princeton University, Princeton, New Jersey 08540, USA
(Received 26 February 2014; revised manuscript received 2 July 2014; published 12 September 2014)

We investigate the dense-flow rheology of cohesive granular materials through discrete element simulations of homogeneous, simple shear flows of frictional, cohesive, spherical particles. Dense shear flows of noncohesive granular materials exhibit three regimes: quasistatic, inertial, and intermediate, which persist for cohesive materials as well. It is found that cohesion results in bifurcation of the inertial regime into two regimes: (a) a new rate-independent regime and (b) an inertial regime. Transition from rate-independent cohesive regime to inertial regime occurs when the kinetic energy supplied by shearing is sufficient to overcome the cohesive energy. Simulations reveal that inhomogeneous shear band forms in the vicinity of this transition, which is more pronounced at lower particle volume fractions. We propose a rheological model for cohesive systems that captures the simulation results across all four regimes.

DOI: 10.1103/PhysRevE.90.032206 PACS number(s): 45.70.−n, 47.57.Gc, 64.60.F−

I. INTRODUCTION

Flows of dense granular materials occur in both natural and industrial processes and exhibit a variety of distinct rheological behaviors. For noncohesive particles, three flow regimes have been identified—namely the quasistatic, inertial, and intermediate regimes [1–4]—each of which manifests different scalings of the mean stresses with shear rate and volume fraction. Numerous constitutive stress models have been constructed with these scalings in mind [2,3,5–10]. However, many granular flows involve cohesive interparticle forces for which the above models do not account. These cohesive effects are the primary focus of the present study.

Cohesion can result from a variety of sources—including van der Waals forces [11,12], electrostatic forces [13], capillary forces [14], and solid bridges [15]—and has a strong impact on granular rheology. For example, agglomeration of particles has been observed in simulations of cohesive granular materials in various flow geometries [16–21]. Annular shear flow experiments [22] and plane shear simulations [18,20,23] have shown that cohesion increases the shear-stress ratio η, defined as the ratio of shear stress τ to pressure p. Both simulations and experiments have shown that the discharge flow rate from a hopper decreases with increasing cohesion [24]. Rotating-drum experiments reveal that cohesion increases avalanche size and leads to robust pattern formation on the surface [25–27]. Despite the number of such phenomenological studies, there is relatively little literature on constituting the rheological effects of cohesion. One notable work is that of Rognon *et al.* [20], which presents modifications to friction and dilatancy laws for noncohesive particles to account for the effects of cohesion observed in two-dimensional (2D) simulations. The present study goes beyond these earlier studies by exposing how the regime map for noncohesive materials [1–4] is altered by the introduction of cohesion and formulating explicit models for the mean stresses.

In this paper, we investigate the rheology of cohesive granular materials through discrete element method (DEM) simulations of homogeneous, simple shear flows of frictional and cohesive particles. Most of the simulations presented here are based on a linear (Hookean) spring-dashpot model [28] for particle-particle interaction and a commonly used model for van der Waals force between particles [29]. The quasistatic regime where the stress is proportional to spring stiffness (and independent of shear rate), the inertial regime where stress is proportional to square of shear rate (and independent of spring stiffness), and the intermediate regime where stress depends on both shear rate and spring stiffness—reported previously for noncohesive particles [2]—persist even when cohesion is added. The presence of cohesion is found to introduce a new rate-independent regime where the stress depends on the strength of cohesion. These regimes persist when the Hookean contact model is replaced by a Hertzian contact model as well as when the van der Waals force model is replaced with an alternate cohesion model proposed by Rognon *et al.* [20], illustrating the robustness of these regimes. Finally, we also modify the blended stress model proposed by Chialvo *et al.* [2] for dense flows of noncohesive particles to obtain an analogous model for dense flow of cohesive particles.

II. SIMULATION METHODS

The DEM simulations [28] were performed using the molecular dynamics package LAMMPS [30]. Particles interact via repulsive spring-dashpot contact forces and attractive cohesive forces. In the spring-dashpot model, the normal and tangential contact forces on a spherical particle i resulting from the contact of two spheres i and j with same diameter d are

$$\boldsymbol{F}_{n_{ij}} = f\left(\frac{\delta_{ij}d}{4}\right)\left[k_n\delta_{ij}\boldsymbol{n}_{ij} - \gamma_n m_{\text{eff}}\boldsymbol{v}_{n_{ij}}\right], \tag{1}$$

$$\boldsymbol{F}_{t_{ij}} = f\left(\frac{\delta_{ij}d}{4}\right)\left[-k_t\boldsymbol{u}_{t_{ij}} - \gamma_t m_{\text{eff}}\boldsymbol{v}_{t_{ij}}\right], \tag{2}$$

where δ_{ij} is the overlap distance, k_n and k_t are spring elastic constants, γ_n and γ_t are viscous damping constants, $m_{\text{eff}} = m_i m_j/(m_i + m_j)$ is the effective mass of spheres with masses m_i and m_j, $\boldsymbol{v}_{n_{ij}}$ and $\boldsymbol{v}_{t_{ij}}$ are the normal and tangential components of relative particle velocity, and $\boldsymbol{u}_{t_{ij}}$ is the elastic shear displacement. For Hookean contact, $f(x) = 1$, while for Hertzian contact, $f(x) = \sqrt{x}$. The magnitude of tangential force is limited by a static yield criterion, $|\boldsymbol{F}_{t_{ij}}| \leqslant \mu|\boldsymbol{F}_{n_{ij}}|$, where μ is the particle friction coefficient. We set values

of $k_t/k_n = 2/7$ [31] and $\gamma_t = 0$. For Hookean contact, for the default case, γ_n is chosen such that the restitution coefficient $e = \exp(-\gamma_n\pi/\sqrt{4k_n/m_{\text{eff}} - \gamma_n^2}) = 0.7$. For Hertzian contact, we employ the same value for $\gamma_n/\sqrt{k_n/m_{\text{eff}}}$, but now the restitution coefficient e depends on the collision velocities.

To account for cohesion, an attractive force $\boldsymbol{F}^C_{n_{ij}}$ is included so the total normal force between the particles becomes $\boldsymbol{F}^T_{n_{ij}} = \boldsymbol{F}_{n_{ij}} + \boldsymbol{F}^C_{n_{ij}}$. For the van der Waals force model, the cohesive force between a pair of particles whose surfaces separated by a distance s is written as [29]

$$\boldsymbol{F}^C_{n_{ij}} = -\frac{Ad^6}{6s^2(s+2d)^2(s+d)^3}, \tag{3}$$

where A is the Hamaker constant. It is assumed that the force saturates at a minimum cutoff distance, $s_{\min} = \theta d$ [29]. Additionally, since the magnitude of the cohesive force decreases rapidly with separation distance, a maximum cutoff distance $s_{\max} = d/4$ [18] is used to accelerate the simulation process; for $s > s_{\max}$, cohesive force is neglected.

We also investigated the alternate model of Rognon *et al.* [20],

$$\boldsymbol{F}^C_{n_{ij}} = -\sqrt{4k_nN_A\delta_{ij}}, \tag{4}$$

where N_A is specified as an input. Note that, in the static limit, where the relative particle velocity is zero, for Hookean contact, the total normal force between two particles is $k_n\delta_{ij} - \sqrt{4k_nN_A\delta_{ij}}$. Accordingly, $-N_A$ is the maximum attractive force between the two particles, experienced when $\delta_{ij} = N_A/k_n$ [20].

Differences between these two cohesion models are significant. The cohesive force in the van der Waals model [Eq. (3)] is present before the particles collide and does not increase with overlap between particles. In Eq. (4), the cohesive force is only present when particles are in contact and increases with extent of overlap. Nevertheless, it will be seen that both models lead to qualitatively similar results, differing in quantitative details only modestly.

In the DEM simulations, assemblies of about 2000 monodisperse particles of diameter d and density ρ_s are placed in a periodic box with fixed volume V. Through the Lees-Edwards boundary condition [32], particles are subjected to homogeneous steady simple shear at a shear rate $\dot\gamma$. The macroscopic stress tensor is calculated as

$$\boldsymbol{\sigma} = \frac{1}{V}\sum_i\left[\sum_{j\neq i}\frac{1}{2}\mathbf{r}_{ij}\mathbf{F}_{ij} + m_i(\mathbf{v}_i')(\mathbf{v}_i')\right], \tag{5}$$

where $\mathbf{r}_{ij}$ is the normal vector pointing from the center of particle j to that of particle i, and $\mathbf{v}_i'$ is the fluctuating velocity of particle i relative to its mean streaming velocity. This stress tensor is further ensemble-averaged over many time steps. Ensemble-averaged pressure and shear stress can thus be obtained as $p = (\sigma_{xx} + \sigma_{yy} + \sigma_{zz})/3$ and $\tau = \sigma_{xz}$. The stresses and shear rate are made dimensionless through scaling with d, ρ_s, and elasticity $k = k_n$. Note that the dimensions of the spring constants and damping coefficients differ for Hookean and Hertzian contacts. Thus, for example, stress will be scaled using k/d and k in Hookean and Hertzian contacts, respectively. As gravity is not included in the simulations, a modified Bond number Bo^* is introduced, which compares the maximum net cohesive force experienced by a particle to a characteristic contact force. For Hookean contact with the van der Waals force model, $\text{Bo}^* = F^{\max}_{\text{coh}}/(kd) \approx A/(24k\theta^2d^2)$, where $F^{\max}_{\text{coh}}$ denotes the maximum cohesive force. For Hertzian contact with the van der Waals force model, $\text{Bo}^* = F^{\max}_{\text{coh}}/(kd^2) \approx A/(24k\theta^2d^3)$. Simulation results indicate that the results are insensitive to the particular value for θ ($1.0\times10^{-5} \leqslant \theta \leqslant 4.0\times10^{-5}$) for specified value of Bo^*. For the results presented in this paper, $\theta = 4\times10^{-5}$ is chosen [18]. Finally, for Hookean contact with the alternate cohesion model, $\text{Bo}^* = N_A/(kd)$.

III. FLOW REGIMES

We first consider Hookean contact and van der Waals cohesion. Simulations are performed for various shear rates, volume fractions, friction coefficients, and modified Bond numbers. Figure 1(a) plots the scaled pressure pd/k against the scaled shear rate $\hat\gamma = \dot\gamma d/\sqrt{k/(\rho_s d)}$ for noncohesive particles with $\mu = 0.1$. Three regimes are present [1–4]: quasistatic at low shear rates and high volume fractions, inertial at low shear rates and low volume fractions, and intermediate at high shear rates and all volume fractions. The quasistatic and inertial regimes are separated by a critical volume fraction ϕ_c, which is a function of μ as summarized in Table I. When cohesive forces are included, however, it is found that this regime map is modified, as shown in Figs. 1(b) and 1(c), where Bo^* is 5×10^{-6} and 5×10^{-5}, respectively. Some aspects remain unchanged: all three noncohesive regimes persist with no change in $\phi_c(\mu)$, and the quasistatic and intermediate pressure values show no appreciable changes. However, the inertial regime is now bifurcated into two regimes occurring at different scaled shear rates: at higher $\hat\gamma$ the flow remains inertial (i.e., exhibiting Bagnold scaling), while at lower $\hat\gamma$ the flow becomes rate independent. We term this latter, new regime the *cohesive regime*. As Bo^* increases, this cohesive regime expands to encompass a larger domain of $\hat\gamma$, as illustrated in Figs. 1(b) and 1(c). Simulations were also performed for a highly inelastic system by lowering e from 0.7 (default case) to 0.02. It was found that all four regimes persist even for such a highly dissipative system, with no discernible change in the magnitude of the jamming volume fraction (see Fig. 2).

TABLE I. Values of model constants.

μ-dependent parameters			
μ	0.1	0.3	0.5
ϕ_c	0.614 ± 0.001	0.596 ± 0.001	0.587 ± 0.001
χ	2.08 ± 0.02	2.09 ± 0.02	2.14 ± 0.08
ϵ	1.00 ± 0.01	0.92 ± 0.01	0.67 ± 0.02
α_{QS}	0.36	0.36	0.20
α_{int}	0.15	0.13	0.10
$\alpha_{\text{coh,1}}$	0.15	0.32	0.26
η_s	0.268	0.357	0.382
α_3	0.23	0.23	0.15

μ-independent parameters									
ϕ_a	α_{inert}	$\alpha_{\text{coh,2}}$	I_0	α_1	β_1	$\hat\gamma_0$	α_2	β_2	α_4
0.45 ± 0.01	0.015	0.008	0.32	0.37	1.5	0.1	0.2	1.0	0.1

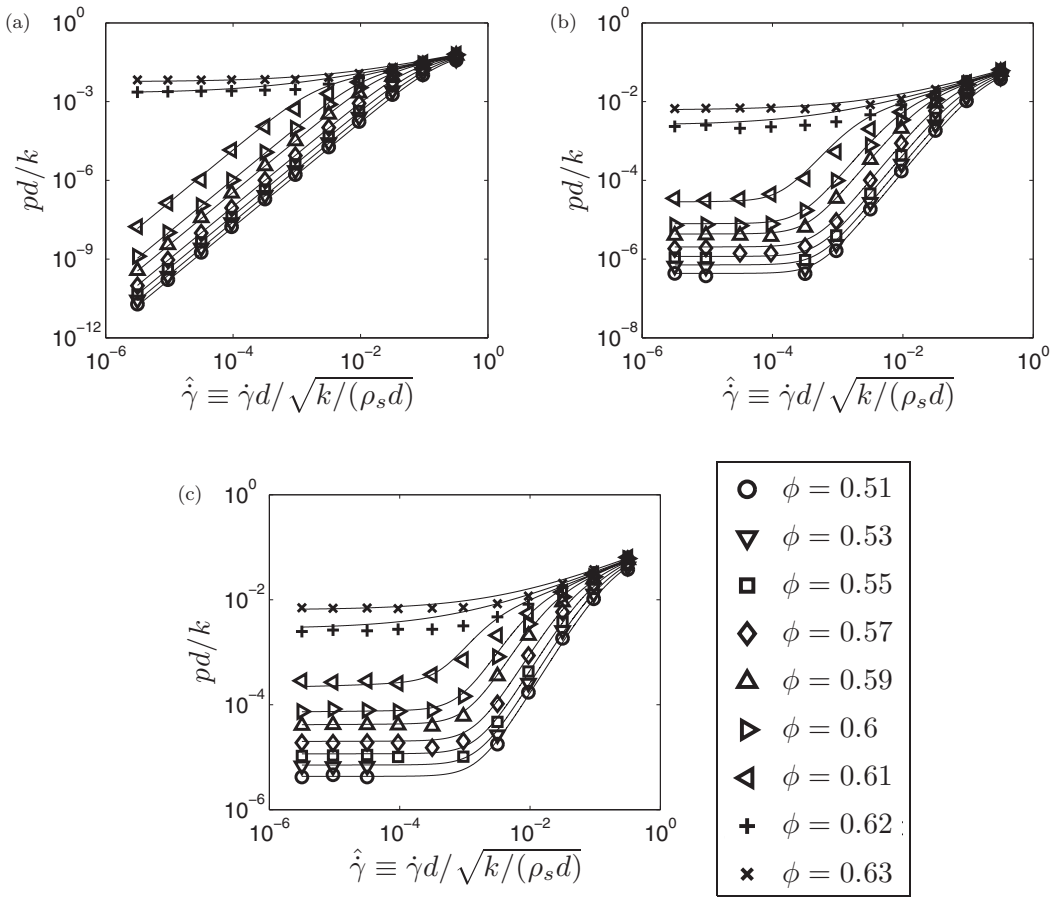

FIG. 1. Scaled pressure versus scaled shear rate for (a) noncohesive particles, (b) cohesive particles with $\mathrm{Bo}^* = 5\times10^{-6}$, and (c) cohesive particles with $\mathrm{Bo}^* = 5\times10^{-5}$. In all cases, Hookean contact and van der Waals force model are used, and the interparticle friction coefficient $\mu = 0.1$. Symbols denote simulation results, while lines denote model predictions from Eqs. (7)–(12).

In Figs. 1 and 2, we present the results only from simulations in which the velocity profile in the statistical steady state is found to be linear indicating homogeneous shear. There is a conspicuous absence of simulation results in Figs. 1(b), 1(c), and 2(b) at the lower volume fractions and shear rates in the region representing transition from cohesive regime to inertial regime. In this region, the velocity profiles are found to be inhomogeneous (see Appendix A for further details). These cases are not included in the analysis of the homogeneously sheared state presented here.

The cohesive regime corresponds well to previous results [18] which report the existence of a rate-independent regime due to cohesion. Also, the cohesive-to-inertial regime transition is in accord with results from dynamic shear cell experiments on slightly cohesive powders [22]; the pressure in these experiments is roughly rate independent at low shear rates but increases significantly at higher shear rates. Finally, the impact of cohesion on the scaling of pressure with respect to shear rate is consistent with previous 2D, constant-pressure shear simulations of Rognon *et al.* [20]. They utilize $N_A/(pd)$ to characterize cohesion and find that, when $N_A/(pd)$ is large, the solid fraction no longer varies with inertial number (defined by them as $\dot{\gamma}\sqrt{m/p}$ for particle mass m) in their dilatancy law, which corresponds to the rate-independent behavior we observe for the pressure in the cohesive regime. The present paper details where this new rate-independent cohesive regime is located in parameter space with respect to the other three regimes and provides a comprehensive regime map for dense flows of cohesive granular materials capable of explaining all of the above behaviors.

Because previous works (e.g., Refs. [20,33]) demonstrate the importance of microstructure on dense granular rheology, we aim to explain the cohesive-to-inertial regime transition in terms of changes in microstructure. To this end, we study the average coordination number Z, which is defined as the average number of contacts per particle in the system. Specifically, $Z = 2n_c/n$, where n_c is the total number of contacts (with particle overlap) and n is the total number of particles in the system. When $\phi > \phi_c$, cohesion has negligible impact on Z across all shear rates (i.e., quasistatic and intermediate regimes), as seen in Fig. 3(a). For $\phi < \phi_c$, cohesion has a weak impact on Z at high shear rates (i.e., inertial and intermediate regimes) but substantially increases the value of Z in lower-shear-rate region (i.e., the cohesive regime), as seen in Fig. 3(b). Thus, cohesion has an appreciable impact on Z only in the cohesive regime, which is consistent with the

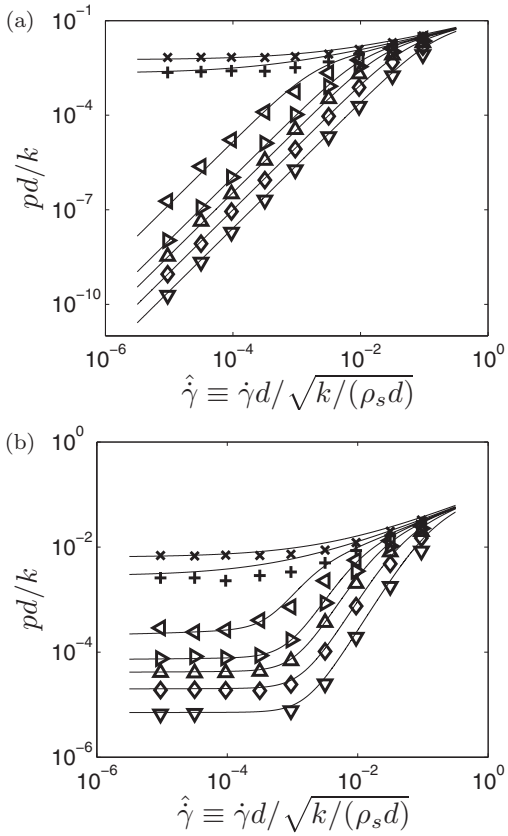

FIG. 2. Scaled pressure versus scaled shear rate for (a) noncohesive particles and (b) cohesive particles with $\mathrm{Bo}^* = 5\times10^{-5}$. Hookean contact and van der Waals force model are used, and the interparticle friction coefficient $\mu = 0.1$ and restitution coefficient $e = 0.02$. Symbols denote simulation results at various volume fractions as per the legend from Fig. 1. Lines denote model predictions from Eqs. (7)–(12). Model parameters used are the same as those in Table I.

pressure data shown in Fig. 1. To make this observation more transparent, we present in Figs. 4(a) and 4(b) the variation of pressure with shear rate corresponding to conditions in Figs. 3(a) and 3(b), respectively. It is clear that cohesion has only a weak impact (if any) on pressure (and, as presented later, shear stress) in quasistatic, inertial, and intermediate regimes. The emergence of a rate-independent regime because of the cohesive force can be reasoned through the average coordination number characterizing the microstructure. When a dense assembly of noncohesive particles is subjected to steady (and slow) shear, jamming occurs at a critical volume fraction, ϕ_c, which depends on the particle-particle coefficient of friction [33,34] and there is a corresponding average coordination number Z_c. Under dynamic conditions [33], the stress tracks Z more closely than the particle volume fraction. Hence it is more accurate to characterize the regimes in terms of Z and shear rate than in terms of volume fraction and shear rate. This distinction is more apparent when particles interact cohesively. For noncohesive assemblies in slow, steady shear, Z falls below Z_c when ϕ drops below ϕ_c. In contrast, for cohesive assemblies, Z can remain large even when ϕ is lowered below ϕ_c, and force chains persist, leading to rate-independent regime. [Compare Figs. 3(b) and 4(b).]

Another behavior connected to the coordination number is the expansion of the cohesive regime with increasing Bo^*, as illustrated in Fig. 3(b). The critical shear rate which sets the boundary between the cohesive and inertial regimes scales with $\sqrt{\mathrm{Bo}^*}$, as demonstrated in Fig. 3(c), where data are collapsed by scaling the dimensionless shear rate with $\sqrt{\mathrm{Bo}^*}$. The $\sqrt{\mathrm{Bo}^*}$ scaling can readily be rationalized: When cohesive energy ($\sim\mathrm{Bo}^*$) is overcome by the kinetic energy supplied by the shearing ($\sim\hat{\dot{\gamma}}^2$), the system transitions from a cohesive regime to an inertial regime. This transition in dependence of Z on shear rate between the cohesive regime and inertial regime is consistent with previous findings [18,19].

The variation of Z with shear rate is analyzed in more detail by decomposing the average coordination number plotted in Figs. 3(a) and 3(b) into two components: one in the extension quadrants (Z_{ext}) and one in the compression quadrants (Z_{com}), as shown in Figs. 5(a) and 5(b). As one would expect, the average coordination number in the compression quadrants is always higher than the counterpart in the extension quadrants [35]. At a packing fraction of 0.62 (which is larger than ϕ_c), Z_{com} and Z_{ext} are essentially the same for cohesive and noncohesive systems, see Fig. 5(a). Furthermore, both of them remain nearly independent of shear rate at low shear rates and decrease at higher shear rates; thus, there is no discernible difference in the behavior in the different quadrants. At

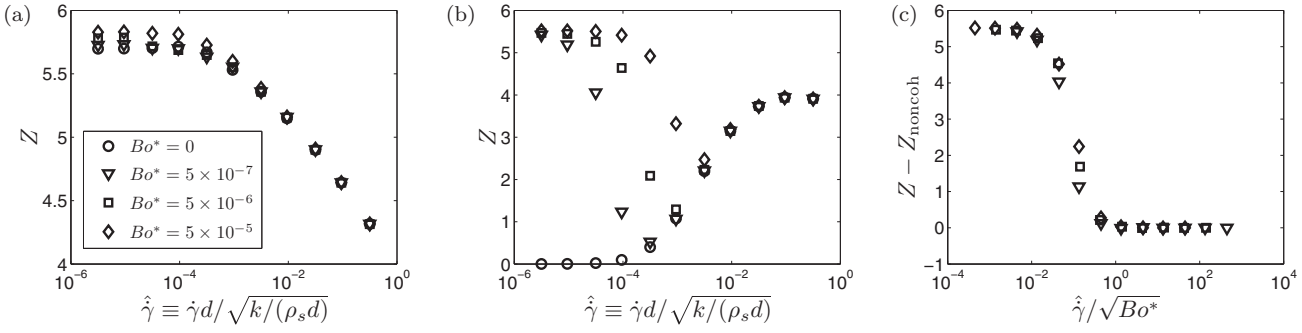

FIG. 3. The average coordination number versus scaled shear rate at $\mu = 0.1$ and various modified Bond numbers for (a) $\phi = 0.62$ and (b) $\phi = 0.59$. In (c), the data from (b) are collapsed into one curve by subtracting Z for noncohesive system from that of cohesive systems and rescaling the shear rate. Hookean contact and van der Waals force model are used here.

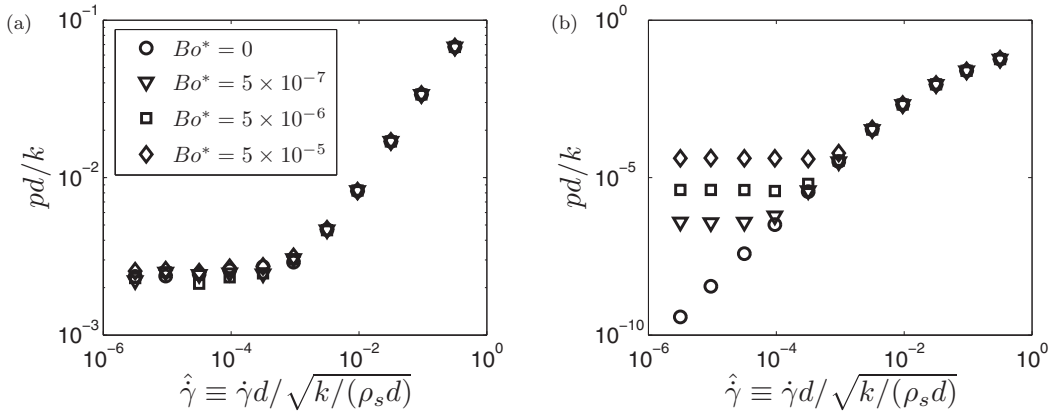

FIG. 4. Scaled pressure versus scaled shear rate at $\mu = 0.1$ and various modified Bond numbers for (a) $\phi = 0.62$ and (b) $\phi = 0.59$. Hookean contact and van der Waals force model are used here.

packing fractions lower than ϕ_c, inertial regime is obtained for noncohesive systems, where both Z_{com} and Z_{ext} increase with shear rate [see Fig. 5(b)]. When the particles interact cohesively and the shear flow is in the cohesive regime, both Z_{com} and Z_{ext} are large at low shear rates (comparable in magnitude to those in the quasistatic regime) under low-shear-rate conditions. Increasing shear rate tends to break down the force chains in all quadrants, weakly at low shear rates and rapidly in the vicinity of $\sqrt{\text{Bo}^*}$, see Fig. 5(b). Once a cohesive system enters the inertial regime, its behavior is similar to that of noncohesive systems, with new contacts forming more readily, leading to an increase in Z_{com} and Z_{ext}. It is the interplay between these two trends that give rise to a minimum in the average coordination number for cohesive systems in the vicinity of $\sqrt{\text{Bo}^*}$ [Figs. 3(b) and 5(b)], and the regime transition observed in the pressure plot [Fig. 4(b)].

IV. PRESSURE

A blended pressure model has been previously proposed for noncohesive granular materials, which can capture the pressure continuously across different dense-flow regimes for different volume fractions and shear rates [2],

$$p = \begin{cases} p_{\text{QS}} + p_{\text{int}} & \text{for} \quad \phi \geqslant \phi_c \\ \left(p_{\text{inert}}^{-1} + p_{\text{int}}^{-1}\right)^{-1} & \text{for} \quad \phi < \phi_c. \end{cases} \tag{6}$$

In this model, p_{QS}, p_{inert}, and p_{int} represent pressure in the quasistatic, inertial, and intermediate regimes. To model the transitions between them, a blending function B of the form $B(y_1, y_2) = (y_1^w + y_2^w)^{1/w}$ is used; $w = 1$ is chosen to create an additive blend for the quasistatic-to-intermediate transition and $w = -1$ is chosen to yield a harmonic blend for the inertial-to-intermedaite transition. Pressure in each individual regime is modeled based on scaling law similar to those in conventional critical phenomena [36–39]. Specifically, one seeks a power-law relationship between pressure and shear rate in each flow regime [2]: $\frac{p_j}{|\phi - \phi_c|^{\epsilon}} \sim [\frac{\dot{\gamma}}{|\phi - \phi_c|^{\omega}}]^{m_j}$, $j = \text{QS, int, inert}$. In the rate-independent quasistatic regime, $m_{\text{QS}} = 0$. In the inertial regime, where pressure varies as the square of shear rate, $m_{\text{inert}} = 2$. Thus, assuming $p_{\text{inert}} \sim |\phi - \phi_c|^{-\chi}$, we set $\omega = (\epsilon + \chi)/2$. Furthermore, as the pressure is essentially independent of $|\phi - \phi_c|$ in the vicinity of the intermediate asymptote, we deduce that $m_{\text{int}} = \epsilon/\omega = 2\epsilon/(\epsilon + \chi)$. Thus,

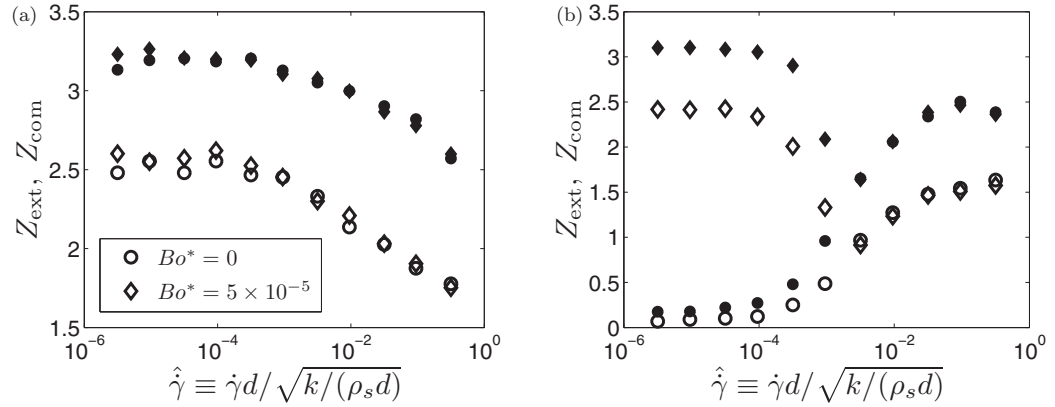

FIG. 5. The average coordination number in the extension quadrants (unfilled symbols) and compression quadrants (filled symbols) versus scaled shear rate at $\mu = 0.1$ for (a) $\phi = 0.62$ and (b) $\phi = 0.59$. Hookean contact and van der Waals force model are used here.

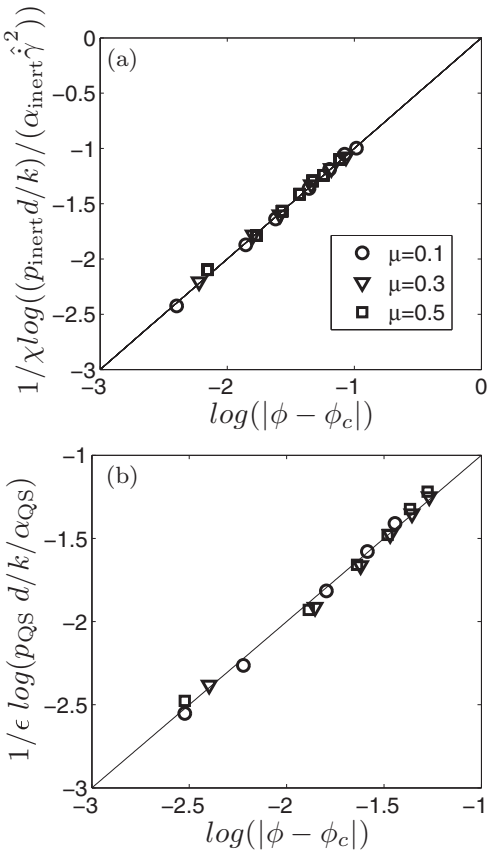

FIG. 6. Collapse of pressure for (a) inertial regime and (b) quasistatic regime. For both (a) and (b), the solid line has a slope of 1 and y intercept of 0. All points with different volume fractions and particle friction coefficients fall on the lines. Hookean contact is used.

for noncohesive particles with Hookean contact,

$$p_{QS}d/k = \alpha_{QS}|\phi-\phi_c|^{\epsilon}, \tag{7}$$

$$p_{int}d/k = \alpha_{int}\hat{\dot{\gamma}}^{2\epsilon/(\epsilon+\chi)}, \tag{8}$$

$$p_{inert}d/k = \frac{\alpha_{inert}\hat{\dot{\gamma}}^2}{|\phi_c-\phi|^{\chi}}. \tag{9}$$

The Levenberg-Marquardt method [40] is used to estimate the model constants. Details are included in Appendix B. As shown in Table I, it is found that α_{inert} is approximately independent of μ, while ϕ_c and α_{int} differ for different μ. The scaling exponent ϵ and prefactor α_{QS} in Eq. (7), as well as the scaling exponent χ in Eq. (9), manifest systematic dependence on μ, which was not reported by Chialvo *et al.* [2], who took $\chi = 2$ and $\epsilon = 2/3$ for all μ. Although it is not the principal focus of this study, we report in Table I the best-fit values of ϵ, α_{QS}, and χ for three different μ values. As demonstrated in Figs. 6(a) and 6(b), Eqs. (7) and (9), respectively, capture the pressure in the quasistatic regime and inertial regime satisfactorily.

Furthermore, the resultant value of $m_{int} = 2\epsilon/(\epsilon+\chi)$ is consistent with experimental results [41,42]. The effectiveness of the power-law relations is illustrated in Fig. 7, where the pressure versus shear rate data at several different volume fractions are collapsed onto two curves (one above ϕ_c and one below). Figures 7(a)–7(c) show results for three different values of μ.

It has been noted previously in the literature [33] that the pressure in the quasistatic regime is not set by particle volume fraction [as in Eq. (7)] and that it tracks more closely the average contact coordination number Z under both steady and dynamic flow conditions. In steady shear flows, Z is set by the particle volume fraction and so Eq. (7) can be thought of the outcome of integrating a relation that applies under steady as well as dynamic conditions and one that is restricted to steady shear flows. Since stress is principally transmitted in the quasistatic regime through force chains, researchers have focused on Z_2, where particles with 0 or 1 contact are excluded as they are not involved in the force chains (e.g., see Refs. [33,43]). We find that the pressure in the quasistatic regime can be expressed as $\alpha_Z[Z - Z_c(\mu)]^2$ or $\alpha_{Z_2}(\mu)[Z_2 - Z_{2c}(\mu)]^2$; see Figs. 8(a) and 8(b). It is interesting to note that when the pressure is expressed in terms of Z or Z_2, the exponent is independent of μ; furthermore, when it is expressed in terms of Z (instead of Z_2), the proportionality constant is also independent of μ and the role of friction is manifested only through $Z_c(\mu)$. As seen in the caption for Fig. 8(a) and 8(b), Z_c and Z_{2c} decrease as μ increases, which is consistent with previous results [33,34]. As seen in Figs. 3(a)

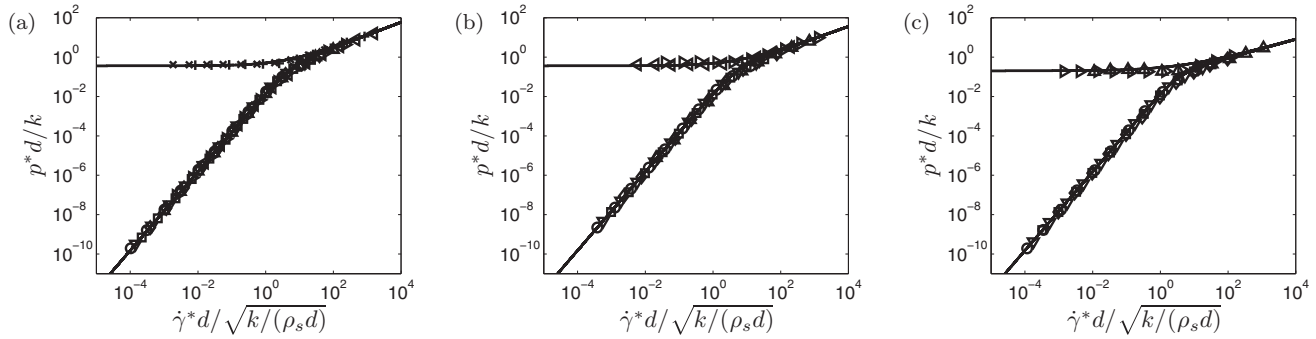

FIG. 7. Collapse of pressure versus shear rate curves for (a) $\mu = 0.1$, (b) $\mu = 0.3$, and (c) $\mu = 0.5$. In all cases, the pressure is scaled as $p^* = p/|\phi-\phi_c|^{\epsilon}$ and shear rate as $\dot{\gamma}^* = \dot{\gamma}/|\phi-\phi_c|^{(\epsilon+\chi)/2}$. (Values for ϵ and χ are included in Table I.) Symbols denote simulation results at various volume fractions as per the legend from Fig. 1. The blending function, described in Eqs. (6)–(9) and represented by solid lines, captures regime asymptotes as well as transitions. Hookean contact with no cohesion is used.

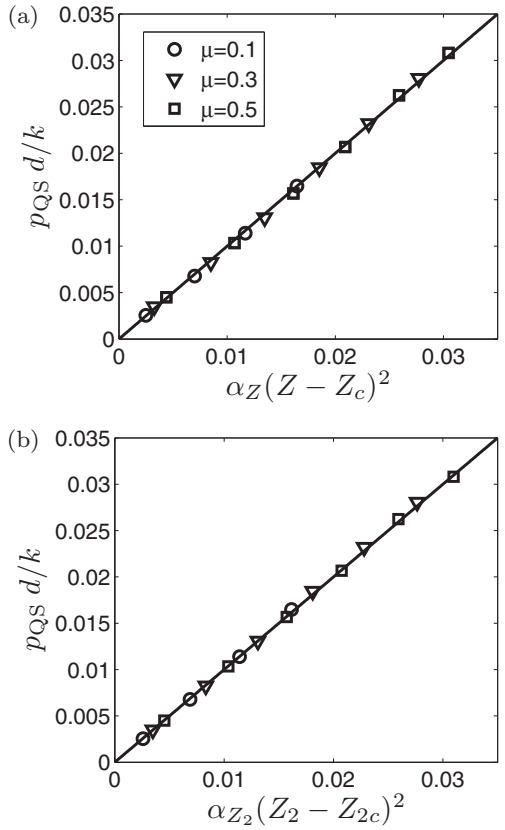

FIG. 8. Simulation data of scaled pressure in the quasistatic regime versus the predictions from the models based on (a) Z and (b) Z_2 for various volume fractions. In (a), $\alpha_Z = 0.007$ and $Z_c = 5.10$, 4.38, and 4.00 for $\mu = 0.1$, 0.3, and 0.5, respectively. In (b), $Z_{2c} = 5.20$, $\alpha_{Z_2} = 0.0077$ for $\mu = 0.1$; $Z_{2c} = 4.56$, $\alpha_{Z_2} = 0.0083$ for $\mu = 0.3$; and $Z_{2c} = 4.26$, $\alpha_{Z_2} = 0.0091$ for $\mu = 0.5$. The system is noncohesive and Hookean contact is used. The line represents $y = x$.

and 4(a), the pressure in the intermediate regime (and $\phi > \phi_c$) increases with shear rate, while Z decreases with increasing shear rate. This clearly shows that the relationship of the type shown in Figs. 8(a) and 8(b) fail in the intermediate regime, even though the stress continues to be largely transmitted through force chains.

The pressure model for noncohesive systems is readily modified to account for the effect of cohesion, as described below. The data reveal two trends which provide clues for constructing simple models. First, as illustrated in Fig. 9, $pd/k \sim \mathrm{Bo}^*$ in the cohesive regime for all volume fractions (except for those near ϕ_c). This behavior is consistent with (a) $pd/k \sim \dot{\hat{\gamma}}^2$ in the inertial regime and (b) the critical $\dot{\hat{\gamma}}$ value separating the inertial and cohesive regimes scales as $\sqrt{\mathrm{Bo}^*}$. Figure 9 shows results down only to $\phi \approx 0.50$. At lower values of ϕ, the flow transitions to shear flows of agglomerates, and the size of the simulation domain used in this study is inadequate to get meaningful results. Second, while the intermediate asymptote (at $\phi = \phi_c$) given by Eq. (8) persists for cohesive particles at high $\dot{\hat{\gamma}}$ values, it becomes rate independent when $\dot{\hat{\gamma}}$ becomes small compared to a critical shear rate. This critical shear rate scales as $\sqrt{\mathrm{Bo}^*}$, as shown

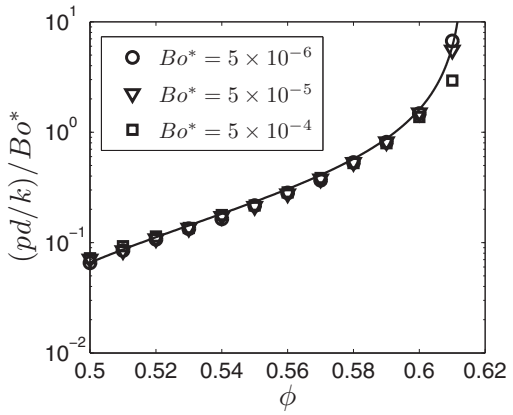

FIG. 9. Dimensionless pressure scaled by Bo^* versus volume fraction in the cohesive regime at $\dot{\hat{\gamma}} = 3.2\times10^{-6}$ for $\mu = 0.1$ and various Bo^* values. The line represents $0.15\frac{|\phi-\phi_a|}{|\phi_c-\phi|}$, where $\phi_c(\mu = 0.1) = 0.614$ and $\phi_a(\mu = 0.1) = 0.45$. Hookean contact and van der Waals force model are used here.

in Fig. 10; this is exactly the same dependence as observed earlier for the cohesive-to-inertial transition. Together these observations suggest that, in the vicinity of ϕ_c, pd/k in cohesive regime scales as $(\mathrm{Bo}^*)^{\epsilon/(\epsilon+\chi)}$.

Based on these observations, Eq. (6) is adapted using the blending function previously described with $w = 1$ to provide an additive blend that can model both the cohesive-to-inertial and cohesive-to-intermediate transitions. Thus, the model becomes

$$p = \begin{cases} p_{\mathrm{QS}} + (p_{\mathrm{int}} + p_{\mathrm{coh},2}) & \text{for } \phi \geqslant \phi_c \\ [(p_{\mathrm{inert}} + p_{\mathrm{coh},1})^{-1} + (p_{\mathrm{int}} + p_{\mathrm{coh},2})^{-1}]^{-1} & \text{for } \phi < \phi_c, \end{cases} \tag{10}$$

where p_{QS}, p_{int}, and p_{inert} are given by Eqs. (7)–(9), and

$$p_{\mathrm{coh},1} d/k = \alpha_{\mathrm{coh},1} \mathrm{Bo}^* \frac{|\phi - \phi_a|}{|\phi_c - \phi|}, \tag{11}$$

$$p_{\mathrm{coh},2} d/k = \alpha_{\mathrm{coh},2} (\mathrm{Bo}^*)^{\epsilon/(\epsilon+\chi)}. \tag{12}$$

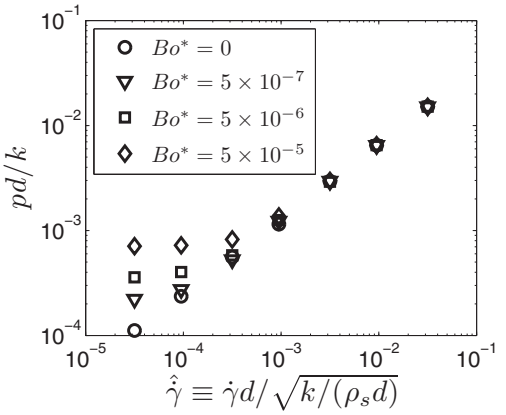

FIG. 10. Scaled pressure versus scaled shear rate at $\phi = 0.614$ for different cohesion levels (as shown in the legend). Interparticle friction coefficient $\mu = 0.1$ is used. Hookean contact and van der Waals force model are used here.

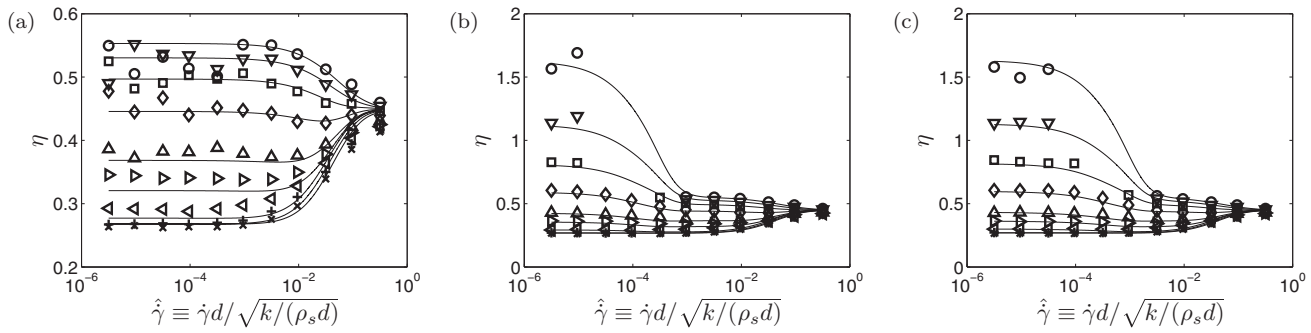

FIG. 11. Shear-stress ratio versus scaled shear rate for (a) noncohesive particles, (b) cohesive particles with $\mathrm{Bo}^* = 5\times10^{-6}$, and (c) cohesive particles with $\mathrm{Bo}^* = 5\times10^{-5}$. In all cases, Hookean contact and van der Waals force model are used, and the interparticle friction coefficient $\mu = 0.1$. Symbols denote simulation results at various volume fractions as per the legend from Fig. 1. Lines denote model predictions from Eqs. (13)–(15) and (19).

For noncohesive particles, where $\mathrm{Bo}^* = 0$, $p_{\mathrm{coh},1}$ and $p_{\mathrm{coh},2}$ vanish, and the proposed model returns to its original form written for noncohesive particles. The Levenberg-Marquardt method [40] is again used to estimate the model constants. (Details are included in Appendix B.) They are provided in Table I. Predictions based on this pressure model are compared with the simulation results in Fig. 1. The proposed model captures the data reasonably well not only in each regime but also in the transition regions.

V. SHEAR-STRESS RATIO

Figure 11 displays the variation of stress ratio $\eta(=\tau/p)$ with the scaled shear rate $\hat{\dot{\gamma}}$ for both noncohesive and cohesive particles with $\mu = 0.1$. Cohesion has a significant effect on the stress ratio only in the cohesive regime, where cohesion increases the stress ratio appreciably. This increase in stress ratio due to cohesion is in agreement with prior experiments [22] and simulations [18,20,23]. It is also consistent with increasing average coordination number with the inclusion of cohesion in the cohesive regime.

The stress-ratio model for noncohesive frictional granular materials proposed by Chialvo *et al.* [2] is composed of two contributions, η_{hard} and η_{soft}. The term η_{hard} is a function of inertial number $I \equiv \dot{\gamma} d/\sqrt{p/\rho_s}$ and describes the shear-stress ratio for infinitely hard particles [8–10], while η_{soft} is a function of $\hat{\dot{\gamma}}$ and describes the deviation from hard-particle behavior due to finite stiffness,

$$\eta^* = \eta_{\mathrm{hard}}(I) - \eta_{\mathrm{soft}}(\hat{\dot{\gamma}}), \tag{13}$$

$$\eta_{\mathrm{hard}}(I) = \eta_s(\mu) + \frac{\alpha_1}{(I_0/I)^{\beta_1}+1}, \tag{14}$$

$$\eta_{\mathrm{soft}}(\hat{\dot{\gamma}}) = \frac{\alpha_2}{(\hat{\dot{\gamma}}_0/\hat{\dot{\gamma}})^{\beta_2}+1}. \tag{15}$$

Here η^* is the stress ratio for noncohesive granular materials, and η_s is the yield stress ratio. The validity of this stress-ratio model for noncohesive granular materials is demonstrated in Fig. 12. By correcting for particle softness, the stress-ratio data from all three regimes and particle friction coefficients are collapsed onto one curve.

As shown below, the well-known Mohr-Coulomb relation $\tau = \eta^* p + C$, which can be cast as

$$\eta = \eta^* + C/p, \tag{16}$$

captures our steady, simple shear flow simulation results in the rate-independent regimes, namely quasistatic and cohesive regimes, provided C is properly modeled. Rognon *et al.* [20] found that the model proposed by Rumpf [44] for C, $C_{\mathrm{Rumpf}} = Z\eta^*\phi\mathrm{Bo}^* k/(\pi d)$, overestimates the value of C needed to match the simulation results. We found the same to be true as well. It is now known that Rumpf's formula does not account for nonaffine particle displacements [45–48], which arise due to the structural disorder in the system. The relevance of nonaffine displacement has been investigated in the context of the shear modulus of covalent amorphous solids. He and Thorpe [49] performed simulations on randomly depleted covalent lattices and found that, for the shear modulus G, $G = 0.33(Z-2.4)^{1.42}$. Recent analytical theory by Zaccone [48] was applied to the same system and led to the expression, $G = 0.36(Z-2.4)$. While this theory captured the critical coordination number well, there is a discrepancy between the theory and simulation results for the exponent and proportionality constant. In an analogous fashion, we accounted for the

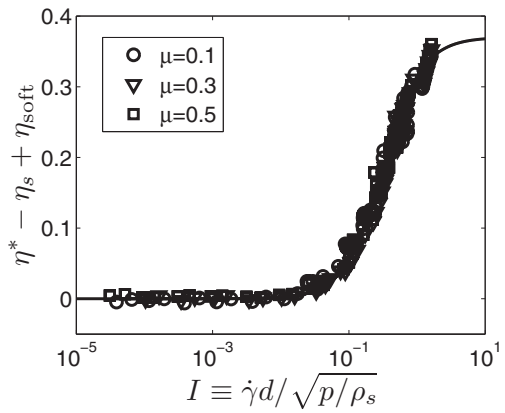

FIG. 12. The correction for particle softness yields a collapse of stress-ratio data for noncohesive particles in all three regimes for various particle friction coefficients (as shown in the legend). The line denotes the expression $\frac{\alpha_1}{(I_0/I)^{\beta_1}+1}$. Hookean contact is used.

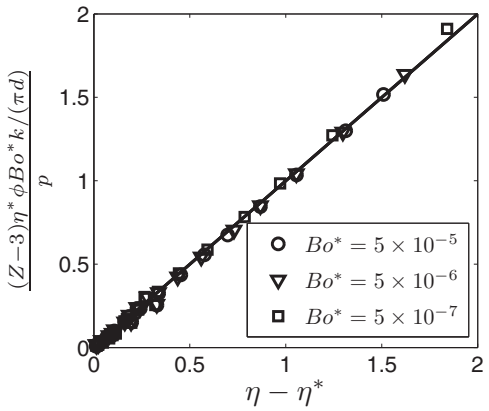

FIG. 13. Predictions of $C^{\text{corr}}_{\text{Rumpf}}/p$ taking account of nonaffine displacements versus $\eta - \eta^*$ from simulation results for different volume fractions ($0.50 \leqslant \phi \leqslant \phi_c$), cohesion levels (as shown in the legend), and friction coefficients ($\mu = 0.1$,0.3, and 0.5) in the cohesive regime. In all cases, Hookean contact and van der Waals force model are used. The line represents $y = x$.

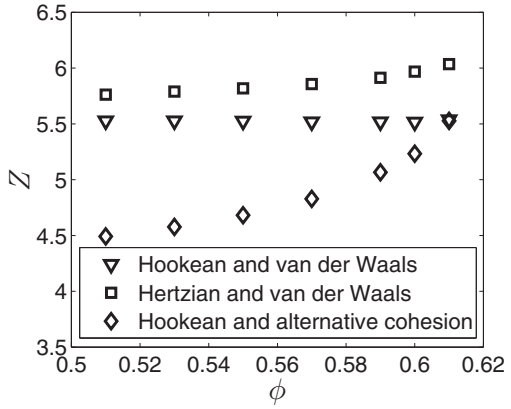

FIG. 14. The average coordination number versus volume fraction in the cohesive regime for particles with $\mu = 0.1$ and $\text{Bo}^* = 5\times10^{-5}$.

effect of nonaffine displacement in our system by replacing Z in the Rumpf model with $a(Z - Z_n)^b$ so

$$C^{\text{corr}}_{\text{Rumpf}} = a(Z - Z_n)^b \eta^* \phi \text{Bo}^* k/(\pi d), \tag{17}$$

and sought if a suitable choice of a, Z_n, and b could capture our simulation results. We found that many combinations of these values yielded equally good fits, making it difficult to discriminate among the different choices. For example, in the spirit of Zaccone [48], one could set $Z_n = 2.4$, $b = 1$ and allow a to be a function of μ and capture the data well (not shown). We found that we could get an equally good fit by setting $a = b = 1$ and $Z_n = 3$ (where now all the parameters are independent of μ); this fit is illustrated in Fig. 13. (As discussed later, $a = b = 1$ and $Z_n = 3$ captured the Hertzian contact results as well.) The simplicity of the fit with $Z_n = 3$ (as opposed to 2.4) could be due to the fact that microscopic models differ. For example, the cohesive force is active not only on the contacts that emerge due to cohesion but also on those that form even in the absence of cohesion in our system, which differs from the system studied by He and Thorpe [49] and Zaccone [48]. In any case, our data do not permit more definitive analysis.

In the quasistatic and cohesive regimes, η^* is essentially η_s, and Z does not vary significantly with the shear rate [e.g., see Figs. 3(a) and 3(b)] and volume fraction (see results for the case of Hookean contact and van der Waals force model shown in Fig. 14). In views of these, and since the coordination number is not directly accessible, a lumped model constant $\alpha_3 = (Z - Z_n)\eta_s/\pi$ is sufficient to capture our data,

$$\eta = \eta^* + \frac{\alpha_3 \phi \text{Bo}^* k/d}{p}. \tag{18}$$

To extend this model to cover rate-dependent regimes, namely inertial and intermediate, we modify the model as follows:

$$\eta = \eta^* + \frac{\alpha_3 \phi \text{Bo}^* k/d}{p} \frac{1}{\frac{\hat{\dot{\gamma}}}{\alpha_4\sqrt{\text{Bo}^*}} + 1}. \tag{19}$$

Here $\alpha_4\sqrt{\text{Bo}^*}$ approximates the critical shear rate which separates the cohesive and inertial regimes. When $\hat{\dot{\gamma}} \ll \alpha_4\sqrt{\text{Bo}^*}$, the model returns to Eq. (18). When $\hat{\dot{\gamma}} \gg \alpha_4\sqrt{\text{Bo}^*}$, the second term in the model vanishes. The model describes stress ratio reasonably well for all Bo^* values considered without any changes to constitutive parameters and for different μ values with slight adjustment of α_3. The values for α_3 and α_4 are listed in Table I.

VI. GENERALITY OF THE RESULTS

The newly identified regime map is preserved when the Hookean contact model is replaced by a Hertzian contact model as well as when the van der Waals force model is replaced with the alternate cohesion model of Rognon *et al.* [20]. The general form of the stress model is also preserved, albeit with small modifications. We illustrate these points by presenting two different particle-scale models: (a) Hertzian contact and the van der Waals force model and (b) Hookean contact and the alternative cohesion model [Eq. (4)].

A. Flow regimes

Figures 15(a) and 15(b) show the variation of scaled pressure against the scaled shear rate for cohesive particles from these two particle-scale models. The cohesive regime, characterized by rate-independent behavior below the critical volume fraction ($\phi_c = 0.614$ for $\mu = 0.1$ in the figures) and lower shear rates, is clearly present in both cases. In addition, simulation results from different Bo^* values confirm that the critical shear rate, separating the cohesive and inertial regimes, scales with $\sqrt{\text{Bo}^*}$ for both cases (not shown).

B. Pressure

The blended model for pressure, given by Eq. (10), remains unaltered, but scalings for the various contributions there change when Hookean contact is replaced with Hertzian contact.

Specifically, $p_j d/k$ is changed to p_j/k. Therefore,

$$p_{\text{QS}}/k = \alpha_{\text{QS}}|\phi - \phi_c|^\epsilon, \tag{20}$$

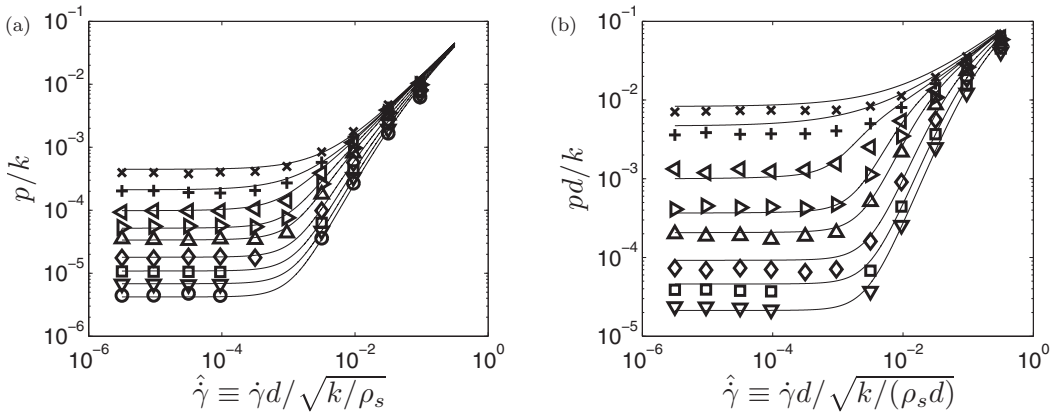

FIG. 15. Scaled pressure versus scaled shear rate for (a) Hertzian contact and the van der Waals force model and (b) Hookean contact and the alternative cohesion model [20]. Here $\mu = 0.1$ and $\mathrm{Bo}^* = 5\times10^{-5}$. Symbols denote simulation results at various volume fractions as per the legend from Fig. 1. Lines denote model predictions from Eqs. (10) and (17)–(21) in (a) and Eqs. (10)–(12) in (b).

$$p_{\mathrm{int}}/k = \alpha_{\mathrm{int}}\hat{\dot{\gamma}}^{2\epsilon/(\epsilon+\chi)}, \tag{21}$$

$$p_{\mathrm{inert}}/k = \frac{\alpha_{\mathrm{inert}}\hat{\dot{\gamma}}^2}{|\phi_c-\phi|^{\chi}}. \tag{22}$$

The Levenberg-Marquardt method [40] is performed to estimate the model constants. (Details are presented in Appendix B.) It is found that $\chi = 1.43 \pm 0.03$. It is found that $\epsilon = 1.56$, 1.21, and 1.10 with uncertainties of ±0.03 for $\mu = 0.1$, 0.3, and 0.5, respectively. The value of ϵ for Hertzian contact is approximately 3/2 times the one for Hookean contact, which is consistent with previous results [33,50]. Using the values for χ and ϵ, the pressure data can now be collapsed onto two curves for different μ, as illustrated in Fig. 16 for the case of $\mu = 0.1$. Thus, Hertzian and Hookean contacts afford similar simulation results such that pressure can be collapsed in a similar fashion.

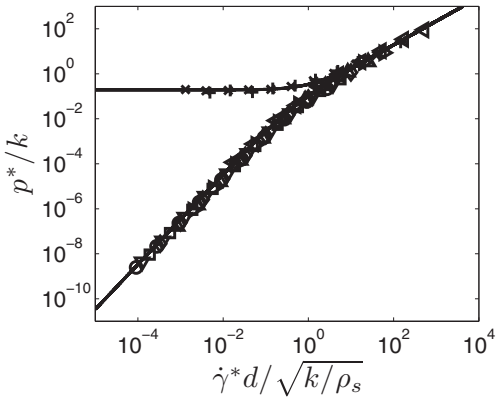

FIG. 16. Collapse of pressure versus shear rate curves for $\mu = 0.1$. The pressure is scaled as $p^* = p/|\phi-\phi_c|^{\epsilon}$, and shear rate as $\dot{\gamma}^* = \dot{\gamma}/|\phi-\phi_c|^{(\epsilon+\chi)/2}$. $\epsilon = 1.56$ and $\chi = 1.43$ is used. Symbols denote simulation results at various volume fractions as per the legend from Fig. 1. The blending function, described in Eqs. (20)–(22) and represented by solid lines, captures regime asymptotes as well as transitions. Hertzian contact with no cohesion is used.

The first cohesive contribution $p_{\mathrm{coh},1}$ remains unchanged from Eq. (11) except for scaling on the left-hand side,

$$p_{\mathrm{coh},1}/k = \alpha_{\mathrm{coh},1}\mathrm{Bo}^*\frac{|\phi-\phi_a|}{|\phi_c-\phi|}. \tag{23}$$

Finally, since $p_{\mathrm{coh},2}$ modifies the intermediate-regime contribution ($p_{\mathrm{int}}/k \sim \hat{\dot{\gamma}}^{2\epsilon/(\epsilon+\chi)}$) and their sum becomes rate independent for $\hat{\dot{\gamma}} \ll \sqrt{\mathrm{Bo}^*}$, it is modified to scale as $\mathrm{Bo}^{*\epsilon/(\epsilon+\chi)}$. This term now becomes

$$p_{\mathrm{coh},2}/k = \alpha_{\mathrm{coh},2}(\mathrm{Bo}^*)^{\epsilon/(\epsilon+\chi)}. \tag{24}$$

Model parameters used in the lines shown in Fig. 15(a) are as follows: $\chi = 1.43$, $\epsilon = 1.56$, $\alpha_{\mathrm{QS}} = 0.19$, $\alpha_{\mathrm{int}} = 0.15$, $\alpha_{\mathrm{inert}} = 0.13$, $\alpha_{\mathrm{coh},2} = 0.006$. Values for ϕ_c, ϕ_a, and $\alpha_{\mathrm{coh},1}$ are the same as those for Hookean contact with van der Waals force model (see Table I).

For case (b), the functional forms for the pressure model are unchanged, and Eqs. (7)–(12) are applied. Only values for ϕ_a, $\alpha_{\mathrm{coh},1}$, and $\alpha_{\mathrm{coh},2}$ now differ: $\phi_a = 0.50$, $\alpha_{\mathrm{coh},1} = 1.2$, $\alpha_{\mathrm{coh},2} = 0.03$.

C. Shear-stress ratio

Stress-ratio models are slightly modified for both cases and compared with the simulation data in Figs. 17(a) and 17(b). For case (a), as noted earlier, $Z_n = 3$ captures our simulation results, and since Z does not change significantly with volume fraction (see results for the case of Hertzian contact and van der Waals force model shown in Fig. 14), we can continue to lump $(Z - Z_n)\eta_s/\pi$ as α_3. As a result of change in the dimension of k for the Hertzian contact, Eq. (19) now reads as follows:

$$\eta = \eta^* + \frac{\alpha_3\phi\mathrm{Bo}^*k}{p}\frac{1}{\frac{\hat{\dot{\gamma}}}{\alpha_4\sqrt{\mathrm{Bo}^*}}+1}, \tag{25}$$

where η^* is described in Eqs. (13)–(15). Model parameters used in the lines shown in Fig. 17(a) are $\alpha_1 = 0.27, \alpha_2 = 0.23$, $\beta_1 = 1.0$, $\alpha_4 = 3$. Values for all the other parameters are the same as those for Hookean contact with the van der Waals force model.

For case (b), $Z_n = 0.5$ captures our simulation results adequately. Since Z changes significantly with volume fraction

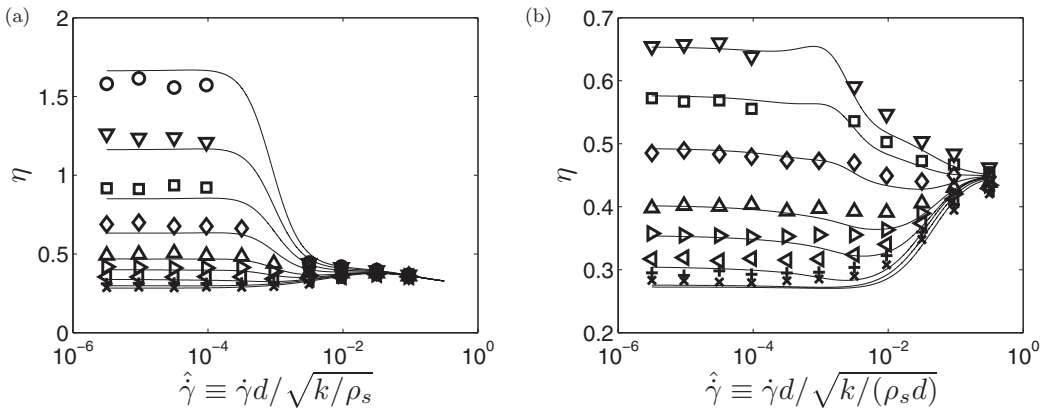

FIG. 17. Shear-stress ratio versus scaled shear rate for (a) Hertzian contact and the van der Waals force model and (b) Hookean contact and the alternative cohesion model [20]. Here $\mu = 0.1$ and $\mathrm{Bo}^* = 5\times10^{-5}$. Symbols denote simulation results at various volume fractions as per the legend from Fig. 1. Lines denote model predictions from Eqs. (13)–(15) and (25) in (a) and Eqs. (13)–(15) and (26) in (b).

(see the results for the case of Hookean contact and the alternative cohesion model shown in Fig. 14), we find that modeling $(Z - Z_n)\eta_s/\pi$ as $\alpha_5(\phi - \phi_a)$ with $\alpha_5 = 10.3$ captures the stress-ratio data well. As a result, Eq. (19) is modified to the following:

$$\eta = \eta^* + \frac{\alpha_5(\phi - \phi_a)\phi \mathrm{Bo}^* k/d}{p} \frac{1}{\frac{\hat{\dot{\gamma}}}{\alpha_4\sqrt{\mathrm{Bo}^*}} + 1}, \qquad (26)$$

where $\alpha_4 = 0.5$. The solid lines in Fig. 17(b) correspond to Eq. (26). Good agreement with simulation results is readily seen.

Note that different expressions for $(Z - Z_n)\eta_s/\pi$ are needed to capture stress-ratio results for van der Waals force model and alternative cohesion model. As noted earlier, the two cohesion models significantly differ: The van der Waals force saturates when the particles come to contact, while the cohesion is only present when the particles are in contact in the alternative cohesion model. Figure 14 illustrates the dependence of the coordination number on volume fraction for the three different cases presented in this article. For Hookean contact and the van der Waals force model, Z is roughly independent from ϕ; for Hertzian contact and the van der Waals force model, Z shows slight dependence on ϕ; and for Hookean contact and the alternative cohesion model, Z increases appreciably with ϕ. This difference in response of coordination number to volume fraction helps explain the necessity of different expressions for $(Z - Z_n)\eta_s/\pi$.

VII. SUMMARY

We have investigated shear flows of dense cohesive granular materials via DEM simulations. The quasistatic and intermediate regimes observed for noncohesive particles persist for cohesive particles, while the inertial regime of noncohesive particles bifurcates into two regimes: rate-independent cohesive regime at low shear rates and inertial regime at higher shear rates. The regime map for the rheology of dense assemblies of cohesive particles is found to be robust even when the particle-scale details of the model are altered. Furthermore, the pressure and shear-stress-ratio results obtained in our simulations can be captured via simple algebraic expressions that can be used in conjunction with continuum models for flows in practical devices.

ACKNOWLEDGMENT

We thank Professor Jin Sun (University of Edinburgh) for help with simulations. This work was supported by DOE/NETL Grant No. DE-FG26-07NT43070.

APPENDIX A: INHOMOGENEOUSLY SHEARED STATE

In all the simple shear simulation results presented in the main text, the locally averaged velocity of the particles is verified to have a very nearly linear profile, and the particle volume fraction profile is uniform. For cohesive particles, shear flow simulations yield inhomogeneous volume fraction and velocity fields at the lower volume fractions considered in this study (namely $\phi \approx 0.5$) and at shear rates in the vicinity of the transition between cohesive and inertial regimes. Figure 18 shows the scaled velocity profiles for two different scaled

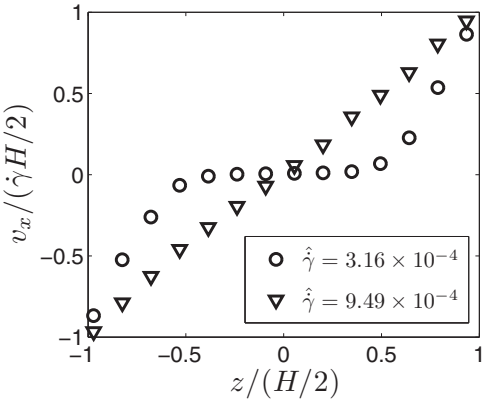

FIG. 18. Locally averaged velocity versus position in the direction of shear. Domain-averaged volume fraction of particles is 0.51. Hookean contact and van der Waals force model are used with $\mu = 0.1$ and $\mathrm{Bo}^* = 5\times10^{-6}$. H denotes the thickness of the periodic box in the shear direction.

shear rates and domain-averaged volume fraction of 0.51. All other conditions are as in Fig. 1(b). It is readily seen that a linear velocity profile was achieved for $\hat{\dot{\gamma}} = 9.49\times10^{-4}$ [results included in Fig. 1(b)] but not for $\hat{\dot{\gamma}} = 3.16\times10^{-4}$ [and hence omitted from Fig. 1(b)]. It appears reasonable to hypothesize that the occurrence of an inhomogeneous state is a manifestation of shear-banding instability [51,52], which has not been a focus of the present study but merits future investigation.

APPENDIX B: MODEL CONSTANTS DETERMINATION

The Levenberg-Marquardt method [40] is used to estimate the critical exponents as well as the values for ϕ_c and ϕ_a in the pressure models for the inertial, quasistatic, and cohesive regimes. Here, we use the case of Hookean contact and the van der Waals force model to detail the process of using this method to arrive at the values as shown in Table I.

For the pressure model in the inertial regime, the functional form $\frac{p_{\text{inert}}d/k}{\hat{\dot{\gamma}}^2} = \frac{\alpha_{\text{inert}}}{|\phi_c-\phi|^\chi}$ is assumed. The Levenberg-Marquardt method is used to estimate ϕ_c and χ from simulation results for noncohesive particles at various shear rates with ϕ as the independent variable and $\frac{p_{\text{inert}}d/k}{\hat{\dot{\gamma}}^2}$ as the dependent variable. The values of χ and ϕ_c for different particle friction coefficients are found and included in Table I.

For the pressure in the quasistatic regime, the functional form $p_{\text{QS}}d/k = \alpha_{\text{QS}}|\phi-\phi_c|^\epsilon$ is assumed. The Levenberg-Marquardt method is performed to estimate ϕ_c and ϵ from simulation results for noncohesive particles at various shear rates with ϕ as the independent variable and $p_{\text{QS}}d/k$ as the dependent variable. The values for ϕ_c are found to be close to the ones previously determined in the inertial regime. These previously determined ϕ_c values are then used to estimate ϵ, which are reported in Table I.

For the pressure in the cohesive regime, the functional form $\frac{p_{\text{coh},1}d/k}{\text{Bo}^*} = \alpha_{\text{coh},1}\frac{|\phi-\phi_a|}{|\phi_c-\phi|}$ is assumed. The Levenberg-Marquardt method is again performed to estimate ϕ_a and ϕ_c from simulation results for cohesive particles at various shear rates and modified Bond values with ϕ as the independent variable and $\frac{p_{\text{coh},1}d/k}{\text{Bo}^*}$ as the dependent variable. The values for ϕ_c are found to be close to the ones previously determined in the inertial regime. These previously determined ϕ_c values are then used to estimate ϕ_a. It is found that ϕ_a is 0.45 ± 0.01, 0.45 ± 0.01, and 0.44 ± 0.01 for $\mu = 0.1$, 0.3, and 0.5, respectively. Thus, the values for ϕ_a are the same for different particle friction coefficients within uncertainties. In Table I of the manuscript, we only report one value for ϕ_a for different particle friction coefficients.

[1] C. S. Campbell, J. Fluid Mech. **465**, 261 (2002).
[2] S. Chialvo, J. Sun, and S. Sundaresan, Phys. Rev. E **85**, 021305 (2012).
[3] M. Otsuki and H. Hayakawa, Phys. Rev. E **83**, 051301 (2011).
[4] G. Lois and J. M. Carlson, Europhys. Lett. **80**, 58001 (2007).
[5] T. Hatano, J. Phys. Soc. Jpn. **77**, 123002 (2008).
[6] M. Otsuki and H. Hayakawa, Phys. Rev. E **80**, 011308 (2009).
[7] K. N. Nordstrom, E. Verneuil, P. E. Arratia, A. Basu, Z. Zhang, A. G. Yodh, J. P. Gollub, and D. J. Durian, Phys. Rev. Lett. **105**, 175701 (2010).
[8] F. da Cruz, S. Emam, M. Prochnow, J.-N. Roux, and F. Chevoir, Phys. Rev. E **72**, 021309 (2005).
[9] G. D. R. MiDi, Eur. Phys. J. E **14**, 341 (2004).
[10] P. Jop, Y. Forterre, and O. Pouliquen, Nature **441**, 727 (2006).
[11] A. Castellanos, Adv. Phys. **54**, 263 (2005).
[12] M. A. S. Quintanilla, A. Castellanos, and J. M. Valverde, Phys. Rev. E **64**, 031301 (2001).
[13] M. F. Al-Adel, D. A. Saville, and S. Sundaresan, Ind. Eng. Chem. Res. **41**, 6224 (2002).
[14] A. Forsyth, S. Hutton, and M. Rhodes, Powder Technol. **126**, 150 (2002).
[15] K. Kuwagi, T. Mikami, and M. Horio, Powder Technol. **109**, 27 (2000).
[16] B. Ennis, Powder Technol. **65**, 257 (1991).
[17] M. Weber, D. Hoffman, and C. Hrenya, Granular Matter **6**, 239 (2004).
[18] L. Aarons and S. Sundaresan, Powder Technol. **169**, 10 (2006).
[19] R. Mei, H. Shang, O. R. Walton, and J. F. Klausner, Powder Technol. **112**, 102 (2000).
[20] P. G. Rognon, J.-N. Roux, M. Naaïm, and F. Chevoir, J. Fluid Mech. **596**, 21 (2008).
[21] R. Brewster, G. S. Grest, J. W. Landry, and A. J. Levine, Phys. Rev. E **72**, 061301 (2005).
[22] J. F. Klausner, D. Chen, and R. Mei, Powder Technol. **112**, 94 (2000).
[23] I. Iordanoff, N. Fillot, and Y. Berthier, Powder Technol. **159**, 46 (2005).
[24] S. Nase, W. Vargas, A. Abatan, and J. McCarthy, Powder Technol. **116**, 214 (2001).
[25] P. Tegzes, T. Vicsek, and P. Schiffer, Phys. Rev. Lett. **89**, 094301 (2002).
[26] P. Tegzes, T. Vicsek, and P. Schiffer, Phys. Rev. E **67**, 051303 (2003).
[27] A. W. Alexander, B. Chaudhuri, A. Faqih, F. J. Muzzio, C. Davies, and M. S. Tomassone, Powder Technol. **164**, 13 (2006).
[28] P. A. Cundall and O. D. L. Strack, Géotechnique **29**, 47 (1979).
[29] R. Y. Yang, R. P. Zou, and A. B. Yu, Phys. Rev. E **62**, 3900 (2000).
[30] S. Plimpton, J. Comput. Phys. **117**, 1 (1995).
[31] J. Shäfer, S. Dippel, and D. E. Wolf, J. Phys. I **6**, 5 (1996).
[32] A. W. Lees and S. F. Edwards, J. Phys. C **5**, 1921 (1972).
[33] J. Sun and S. Sundaresan, J. Fluid Mech. **682**, 590 (2011).
[34] C. Song, P. Wang, and H. A. Makse, Nature **453**, 629 (2008).
[35] C. S. Campbell and C. E. Brennen, J. Fluid Mech. **151**, 167 (1985).
[36] C. S. O'Hern, S. A. Langer, A. J. Liu, and S. R. Nagel, Phys. Rev. Lett. **88**, 075507 (2002).
[37] C. S. O'Hern, L. E. Silbert, A. J. Liu, and S. R. Nagel, Phys. Rev. E **68**, 011306 (2003).
[38] P. Olsson and S. Teitel, Phys. Rev. Lett. **99**, 178001 (2007).

[39] M. Otsuki and H. Hayakawa, Prog. Theor. Phys. **121**, 647 (2009).
[40] P. Olsson and S. Teitel, Phys. Rev. E **83**, 030302 (2011).
[41] J. R. Seth, M. Cloitre, and R. T. Bonnecaze, J. Rheol. **52**, 1241 (2008).
[42] J. R. Seth, L. Mohan, C. Locatelli-Champagne, M. Cloitre, and R. T. Bonnecaze, Nat. Mater. **10**, 838 (2011).
[43] K. Shundyak, M. van Hecke, and W. van Saarloos, Phys. Rev. E **75**, 010301 (2007).
[44] H. Rumpf, Chemie Ing. Tech. **30**, 144 (1958).
[45] A. Zaccone and E. Scossa-Romano, Phys. Rev. B **83**, 184205 (2011).
[46] A. Zaccone and E. M. Terentjev, Phys. Rev. Lett. **110**, 178002 (2013).
[47] A. Zaccone and E. M. Terentjev, J. Appl. Phys. **115**, 033510 (2014).
[48] A. Zaccone, Mod. Phys. Lett. B **27**, 1330002 (2013).
[49] H. He and M. F. Thorpe, Phys. Rev. Lett. **54**, 2107 (1985).
[50] H. P. Zhang and H. A. Makse, Phys. Rev. E **72**, 011301 (2005).
[51] B. Utter and R. P. Behringer, Phys. Rev. E **69**, 031308 (2004).
[52] A. Singh, V. Magnanimo, K. Saitoh, and S. Luding, Phys. Rev. E **90**, 022202 (2014).